Reduced-Order Modeling of Mistuned Bladed Disks in Contact with Dry Friction Ring Dampers

by

Weihan Tang

A dissertation submitted in partial fulfillment
of the requirements for the degree of
Doctor of Philosophy
(Mechanical Engineering)
in the University of Michigan
2017

Doctoral Committee:

Professor Bogdan I. Epureanu, Chair
Professor Noel Perkins
Professor Nickolas Vlahopoulos
Professor Kon-Well Wang

2017

To my parents, my family, and everyone who helped me during the years.

ACKNOWLEDGEMENTS

I would like to express my deepest gratitude to my advisor, Professor Bogdan I. Epureanu, for serving as my advisor and chair of my doctoral committee. Your guidance has always been invaluable to me, and eventually made this work possible. I would also like to thank the other members of my committee, Professor Noel Perkins, Professor Nickolas Vlahopoulos, and Professor Kon-Well Wang for their comments and suggestions.

I would like to thank the sponsor of this work, GE Aviation, through the University Strategic Alliance (USA) program. I would like to thank Dr. Sergio Filippi, Dr. Yoon Choi, and other members of the GE community for their suggestions and guidance during this work.

Finally, I would like to thank my parents for their continuous encouragement, love, and support over the many years.

TABLE OF CONTENTS

LIST OF FIGURES

LIST OF TABLES

ABSTRACT

Bladed disks (blisks) used in turbomachinery applications frequently operate under severe forcing conditions, which can lead to high levels of dynamics responses and pre-mature high cycle fatigue (HCF). Small blade-to-blade variations in structural properties, referred to as mistuning, result in strain energy localization, drastically amplifying blisk forced responses, and accelerate HCF. To quantitatively capture the effect of mistuning, it is necessary to develop efficient computational methods to predict the free and forced responses of blisks with various types of mistuning patterns. Due to the high geometric complexity of commercial blisks, full-order finite element (FE) blisk models contain many degrees of freedom (DOFs). Direct structural analyses with such FE models are computationally cumbersome or practically infeasible. Moreover, to prevent blisks from reaching HCF, frictional damping sources are introduced to dissipate vibrational energy and reduce the level of forced responses. Frictional damping is nonlinear in nature, and adds complexity into the blisk systems. Thus, robust and accurate reduced-order models must be developed to predict fast the dynamic responses of blisks with various mistuning and frictional damping sources.

The main objective of this study is to develop a framework that involves several novel reduced-order modeling techniques. This framework is capable of efficiently and accurately capturing linear and nonlinear dynamic responses of blisks with small blade material variations, large changes in blisk mass, stiffness, and geometry, and dry friction ring dampers. Moreover, this framework serves as a powerful tool in designing friction dampers with optimal design parameters.

CHAPTER 1

Introduction

1.1 Dissertation Objective

Ideally, an integrally bladed disk (blisk) possesses cyclic symmetry, and each of its sectors carries identical geometry and material properties. This property enables structural analyses of a full-order blisk system to be performed with the model of a single sector. However, variations in structural properties of individual sectors, referred to as mistuning, are often introduced by non-uniform material properties, manufacturing tolerances, wear, and operational damages. Mistuning can lead to localization of strain energy and drastic increases in forced responses. Thus, in the blisk design process, the effect of mistuning must be accounted for to prevent potential structural failure from premature high cycle fatigue (HCF). To prevent mechanical failures caused by HCF, and to increase the working lifetime of blisks, extensive effort has been made to reduce the amplitudes of forced vibrations by introducing various designs of frictional damping sources to blisks, such as underplatform wedge dampers, frictional shroud contacts, and ring dampers.

Unfortunately, cyclic symmetry no longer exists in the presence of mistuning. Therefore, a single sector is insufficient, and the full-order model of the entire blisk is required to capture the free and forced responses of mistuned blisks. Full-order finite element (FE) models of commercial blisks may contain many degrees of freedom (DOFs), and analyses performed on such models are computationally expensive. Moreover, mistuning patterns are random, and are best studied via statistical analyses. A Monte Carlo analysis requires sampling the blisk dynamics over a large number of mistuning patterns, and is infeasible when full-order FE models are involved. Thus, researchers have developed various reduced-order models (ROMs) to replace the full-order FE models. These ROMs accurately predict the dynamics of mistuned systems with significantly reduced computational effort. However, linear ROMs cannot be directly applied to blisks in contact with frictional dampers, as frictionally damped systems are nonlinear in natural. As a result, ROMs are

often combined with iterative solution methods to become capable of modeling nonlinear blisk-damper systems.

Motivated by these concerns, this work aims to explore ROMs to predict the structural dynamics of blisks under various conditions, including blisks with small material mistuning, large geometric mistuning, and frictional ring dampers. Specifically, this work aims to achieve the following:

- To develop ROMs that can model blisks with both small and large mistuning. The ROM construction process should not incur high computational cost, and should be efficient to be used for Monte-Carlo analyses to retrieve statistical characteristics of blisk dynamics under random mistuning.
- To develop ROMs that can accurately capture the contact dynamics between a mistuned blisk, and a dry friction ring damper. The ROM should be compact enough to be used for statistical analysis to study the correlation between small mistuning and frictional damping.
- To further enhance the capability of the developed ROMs so that they are capable of analyzing structural dynamics of blisks with both small and large mistuning, and in contact with friction dampers.
- To explore the effect of variations of damper geometry on its effectiveness in dissipating vibrational energy. A set of design guidelines should be proposed to obtain optimal damper geometries.

1.2 Dissertation Background

1.2.1 Modeling of Mistuning

Most of the existing reduced-order modeling techniques focus on small mistuning, assuming that mistuning is small enough to be modeled as deviations in natural frequencies of a nominal system. This assumption fails in the presence of significant changes of mass, stiffness and geometry, hereafter referred to as large mistuning. One of the first reduced-order modeling techniques for solving large mistuning problems was developed by Lim et al. [1,2], based on the technique of component mode synthesis (CMS), where the mistuned blisk is substructured into a tuned model and a virtual mistuning component. The tuned blisk is projected onto its normal and attachment modes, whereas the mistuning component is projected onto its normal and constraint modes. This method is general and can

be applied to model both large and small mistuning. Unfortunately, since the attachment and constraint modes are computed for each of the interface DOFs, the size of the resulting ROM is very large. Thus, Lim et al. proposed a mode-acceleration formulation to reduce the size of the ROM [3], where the projection basis is formed by tuned system modes compensated by a set of quasi-static modes. The resulting ROM is much smaller in size without significantly sacrificing its accuracy. However, this method is not effective to study random mistuning since the quasi-static modes need to be repetitively computed for each mistuning pattern. An interesting approach that targets random geometric mistuning was proposed by Sinha [4]. His method characterizes geometric variations by a few proper orthogonal decomposition (POD) features. A mode basis is formed by truncated sets of system normal modes, where each set is obtained from a blisk model carrying a distinct POD feature. This method is subsequently applied to model multistage blisks with random mistuning patterns [5]. However, the number of POD features increases as the complexity of geometric variations grows. Note that the mode bases formed by the above methods require system-level mode shapes, which are extracted from the full-order blisk models. In contrast, a method that utilizes cyclic modes was proposed by Mbaye et al. [6] to tackle geometric mistuning. Cyclic mode shapes of each mistuned sector are obtained in their method from cyclic symmetry modal analyses, which involve only sector-level computations. These sector-level mode shapes are expanded to assemble the corresponding system-level mode shapes, which are subsequently used to form a mode basis. Unfortunately, such a mode basis is very large in size, and direct projection of the full-order systems onto the mode basis results in very heavy computations. Moreover, a modal scale factor (MSF) is adopted to correct the phase shift among mode shapes of sectors with different mistuning, characterized by rotations of nodal diameters. Computing MSF requires all mistuned sectors to have the same number of DOFs. Consequently, this method is not applicable to geometric mistuning that involves large volumes of missing material. Mbaye's method also has other issues yet to be addressed, including overly constrained ROMs, and potentially ill-conditioned mode bases.

An exciting approach was proposed by Madden et al. [7] to efficiently model large mistuning. Their technique is named the pristine rogue interface modal expansion (PRIME), as it partitions a mistuned blisk into three components, including 1) a pristine component that contains all DOFs of sectors identical to a nominal sector, 2) a rogue component that contains all DOFs of sectors that have large mistuning, and 3) an interface component that connects the pristine and rogue components. Similar to the method developed by Mbaye et al., the mode basis formed by the PRIME technique makes use of cyclic modes. However, instead of projecting the blisk onto full-order mode shapes, which requires system-level

computations, PRIME projects each sector onto its own cyclic modes expanded to only the corresponding sector DOFs. Thus, the projection process is maintained on a sector level. Displacement compatibility is then enforced across the interface DOFs. Note that all computations required by the PRIME method are on a sector level. This feature makes PRIME a promising candidate for studying random mistuning due to the low computational cost involved. Compared to Mbaye's method, PRIME does not require any phase angle matching process. PRIME has a conditioning process that prevents the ROM to be overly constrained, and eliminates the ill-conditioning problem of the mode basis.

Small mistuning has been studied extensively, and many efficient approaches have been developed. Most of the techniques fall into two categories: component-mode-based and system-mode-based techniques. The first category of methods is based on the CMS technique, and involves substructuring a blisk into disk and blade components. Ottarsson et al. [8, 9] proposed a hybrid-CMS method suggesting that the blade responses can be expressed as a linear combination of system normal modes computed for a blisk model with massless blades, in addition to a set of cantilever blade modes (CB modes). This method has been adopted by Bladh et al., and extended to study the dynamics of shrouded blisks [10], and the effect of random mistuning [11]. However, Ottarsson's method suffers from inaccuracy in predicting the motion at the disk-blade interfaces. To accurately capture the interface responses, the Craig-Bampton CMS (CB-CMS) technique was adopted by Bladh et al. [12, 13], where the blade and disk components are projected on to their respective normal and constraint modes, with displacement compatibility enforced across the disk-blade interface. Since the constraint modes are computed by applying a unit displacement at every interface DOF, the resulting ROMs are very large in size. Although Bladh et al. proposed a secondary modal analysis as a subsequent approach to reduce the ROM size, this method requires re-calculating the mode basis once the mistuning pattern changes. In 2001, Yang et al. [14] proposed the first system-mode-based approach for modeling small mistuning. This method is referred to as the subset of normal modes (SNM), as it is based on the assumption that mode shapes of a mistuned blisk with closely spaced natural frequencies can be expressed as a linear combination of the normal modes of a tuned system in the same frequency range. Thus, the ROM of a mistuned blisk can be constructed with a mode basis that contains only the normal modes of a tuned system. SNM importantly indicates that small mistuning can be modeled without substructuring the blisk, as required by the component-mode-based techniques. Feiner et al. [15] subsequently developed a simplified form of SNM that requires very few input parameters, including only the natural frequencies of a tuned system and the mistuning-incurred deviation in blade-alone natural frequencies. Due to its minimal input requirement, this method is named the fundamental

mistuning model (FMM). However, the simplicity of FMM is achieved by trading off its generality, as FMM is only applicable when an isolated family of blade-dominated modes is excited. Note that SNM has a feature that is favorable in statistical analyses of random small mistuning. The basis formed by SNM contains modes of only a tuned system and does not require re-constructions when the mistuning pattern changes. However, the modes adopted by the SNM method are system-level normal modes, which are large in size for refined blisk models.

As noted above, Lim et al. proposed a CMS-based method that can solve both large and small mistuning problems. They also derived a simplified form of this approach that focuses on small mistuning [1, 2]. This formulation, named component mode mistuning (CMM), is similar to SNM in principle, which makes use of the normal modes of a tuned system. However, based on the observation that most strain energy is localized in the blades, it is assumed that the effect of mistuning on the system responses is dominated by the blade mistuning components. Thus, Lim et al. further assume that small mistuning only exists in the blades. Then, the blade mistuning components are projected onto a set of CB modes. Modal participation factors are calculated to represent the contribution of each CB mode, and to relate the blade-alone responses to the basis of system normal modes. Compared to SNM, CB modes are much smaller in size than the system normal modes. Also, the blade motion is usually dominated by only a few CB modes, and the size of the CB mode basis can be further reduced. Therefore, the computational effort required by CMM for model reduction is significantly lower than that required by SNM. However, CB modes are calculated with the disk-blade interface held fixed, which assumes no motion at the root of the blade. Thus, CMM suffers from inaccurate prediction for responses associated with high interface motions. Also, CMM restricts mistuning to exist only in the blade components, whereas in practice mistuning is random and can spread throughout the entire blisk. Moreover, to compute CB modes, it is required to have a clear root of the blade, which is not readily defined for complex structures such as dual-flow path systems. Vargiu et al. [16] proposed the approach of integral mode mistuning (IMM) as an alternative to CMM. IMM replaces the CB modes with the normal modes of a sector with free boundary conditions. Such a mode basis eliminates the need of a root of the blade, and makes IMM applicable to more realistic mistuning patterns.

Nodal energy weighted transformation, or NEWT, was recently proposed by Fitzner et al. [17] as an efficient approach for modeling small mistuning. Similar to CMM, a mistuned blisk is substructured into a tuned blisk and a virtual mistuning component. The mistuning component is first projected onto a set of projection modes, and transformed into the modal coordinates of a system tuned mode basis through participation factors. However, unlike

the CB modes used by CMM and the normal modes of a sector with free interfaces used by IMM, NEWT uses normal modes of a tuned sector with cyclic boundary conditions (cyclic modes). Similar to IMM, these sector-level normal modes eliminate the need of a root of the blade, and allow small mistuning to exist on multiple components throughout a blisk. A mode selection criterion was developed based on the fact that within a family of the cyclic modes, those associated with higher nodal diameters share similar shapes and can be mutually dependent. Through such a criterion, the basis of projection modes can be further reduced while the accuracy of the ROM is maintained.

1.2.2 Modeling of Frictionally Damped Blisks

To investigate the complex and nonlinear contact dynamics of dry friction damping, a variety of contact models have been developed and can be found in literatures. Due to its simplicity, one-dimensional (1D) marco-slip contact models have been widely used [18–20], and validated by data obtained from bench tests [21]. Arrays of 1D macro-slip models are constructed to capture the micro-slip phenomenon [22–25]. These 1D friction models are based on the assumption that the normal load acting on the contact surfaces is constant. However, in the presence of out-of-plane motions, this assumption no longer holds. Yang et al. [26] developed a 1D contact model that features normal contact stiffness to capture the variable normal loads between two contact surfaces induced by relative motions in the normal direction. Transition criteria for contact status among stick, slip, and separation conditions were also suggested. Cigeroglu et al. [27] adopted this model, and proposed a multi-mode solution method.

The contact models described above focus on 1D relative motions between two contact surfaces. Sanliturk et al. [28] extended the 1D macro-slip contact model by allowing a single-spring point contact to travel on a 2D plane. Menq et al. [29] developed a 2D contact model that contains two coupled tangential contact springs, and derived analytical transition criteria for contact status. Yang et al. [30] addressed the issue of variable normal loads for 3D relative motions between contact surfaces. Their 3D contact model was further used to predict forced responses of nonlinear structures under periodic forcing [31].

Frictional contacts are nonlinear in nature. To solve the equations of motion of blisk-damper systems that carry nonlinear contact models, a variety of solution methods have been developed. Early studies focus on analytic derivations of the contact dynamics, and heavily rely on assumptions of the damper geometry [32, 33]. Tanrikulu [34] proposed the technique of describing functions, which models the nonlinear contact forces as response-dependent equivalent damping and stiffness. Cigeroglu et al. [35] adopted this technique

to study the dynamics of a friction-damped tip-shrouded blisk. Compared to describing functions, a more well-known and widely adopted solution method is the harmonic balance method (HBM). Cardona applied HBM to predict periodic responses of a frictionally damped system, and provided an analytical Jacobian for the Newton-Raphson solver [36]. Yang et al. [37] assumed two rigid contact surfaces between a blisk and a wedge damper, where each contact surface is modeled by a 1D macro-slip contact model that accounts for normal load variations. This work includes analytical transition criteria of contact status that involve simultaneous stick-slip motions of two contact surfaces. HBM was used to solve the nonlinear equations of motion [38]. A similar method is developed by Sanliturk et al. [39], in which a two-dimensional contact model is used to account for the relative motions in the axial direction of the blisk. Csaba [22] applied HBM to study the dynamic responses of a curve-shaped underplatform damper. HBM has also been adopted to study the periodic responses of blisks with frictional shroud contacts [40–42]. Variants of HBM have also been developed to improve its efficiency [43,44]. Guillen developed a hybrid frequency/time (HFT) domain method. In the HFT method, the nonlinear friction forces are computed in the time domain, and transformed to the frequency domain, in which the equations of motion are solved by Newton-Raphson-like methods [45]. This method has been adopted by Poudou et al. [46] to analyze friction damping in turbomachinery applications.

Although HBM and its variants have proved efficiency in analyzing friction-damped systems, directly applying HBM to commercial FE models of blisk-damper systems can be computationally expensive as the nonlinear equations of motion may contain many DOFs. To address this issue, ROMs have been introduced to reduce the size of the full-order models. Exploiting cyclic symmetry, it is possible to use the model of a single sector to obtain forced responses of blisks with frictional shroud contacts [47, 48]. Classical model reduction methods, such as CB-CMS [49], are used to condense full-order models into a relatively small subset of physical DOFs, including those on the contact surfaces, and modal coordinates of the system normal modes with fixed CB-CMS interfaces [46, 50]. A modal superposition method was introduced by Cigeroglu et al. [27] to project the full-order models onto their free mode shapes. That approach adds rigid body mode shapes into the projection mode basis [51, 52]. Recently, Mitra et al. [53] proposed a method using adaptive micro-slip projection. This method is based on combining mode shapes of a set of linear systems with strategically chosen boundary conditions on the contact surfaces.

The frictional contact models, solution methods and ROMs described above have been extensively used to study underplatform wedge dampers, and frictional shroud contacts. Comprehensive reviews are also available in literature [54, 55]. In contrast, limited work has been done to study ring dampers. In the early studies, Niemotka et al. [56] analyzed the

stress-strain relationships of a split ring under static forcing. Laxalde et al. [57] constructed a lumped-parameter model of the blisk-damper system that features a 1D macro-slip contact model. The resulting nonlinear equations of motion were solved by the HFT method. The HFT method was further applied to a more realistic FE model of the blisk-ring system [58]. A dynamic Lagrangian method was used to predict the nonlinear contact forces. A nonlinear modal analysis approach was developed by Laxalde et al. [59], and applied to determine design parameters of ring dampers.

1.2.3 Optimization of Damper Effectiveness

The effectiveness of friction dampers are commonly evaluated by the reduction in forced response amplitudes at resonance. The non-linear forced responses of blisk-damper systems are usually obtained by solving the equation of motion (EOM) in the frequency domain based on HBM due to its superior computational efficiency. Although existing ROMs and solution methods are powerful, it is often demanded, from a design perspective, to identify a few sets of parameters that provide maximum energy dissipation and minimum forced responses at resonance. Thus, it is necessary to understand the sensitivity of forced responses to variations of each design parameter. Conventional approaches of investigating the effect of damper parameters on resonant responses involve performing forced response analyses with a large amount of pre-selected sets of parameters. Unfortunately, repetitive computations of nonlinear forced responses, even with the advanced ROMs and solution methods, require significant computational effort. Moreover, the pre-selected sets of parameters are often not guaranteed to provide all necessary information required to search for an optimal solution.

Sensitivity analyses have been adopted in many research areas to facilitate in tracing the optimal sets of design parameters, and reducing the amount of repetitive computations. The optimization problem can be efficiently solved when the sensitivity characteristics of forced responses are determined. Unfortunately, limited investigations on forced response sensitivity have been done in turbomachinery applications, especially for frictionally damped blisks. Based on direct parametric analyses, Petrov et al. [60, 61] proposed a method to predict nonlinear forced responses of frictionally damped blisks as a function of contact parameters. The authors also derived analytical expressions of forced response sensitivity to variations of each contact parameter. This method was further extended to directly predict the sensitivity of resonant frequencies and responses at resonance to contact parameter variations and external forcing levels [62, 63]. A similar method was developed by Krack et al. [64], with uncertainties in the design parameters and the excitation level taken into

account. Although methods based on direct parametric analyses are effective in determining an optimal set of contact parameters, unfortunately, these methods share a common limitation by assuming the geometry of a blisk-damper system remains unchanged during optimization. The effectiveness of a friction damper depends not only on the contact parameters, but also on its geometry.

1.3 Dissertation Outline

Chapter II introduces a reduced-order modeling technique that is capable of modeling blisks with simultaneous large and small mistuning. The resulting ROM is expected to be computationally efficient so that it is applicable to perform statistical analyses to study the effects of random mistuning. The PRIME method [7] is capable of solving both large and small mistuning problems. However, when sampling over a large amount of mistuning patterns, especially when statistical analyses are involved, repetitively re-constructing the ROM for each combination of large and small mistuning patterns can be a computationally formidable task. Thus, it is necessary to adopt a method that specifically handles small mistuning and is computationally less expensive than the current PRIME method. Strategically integrating a modified NEWT approach into the PRIME work frame can significantly reduce the computational effort, and extend the PRIME technique to investigate random mistuning. The NEWT projection basis is computed for a pristine sector and one of each of the rogue sectors. The small mistuning component of each sector is then projected onto its corresponding NEWT basis. Unlike the current NEWT method, the participation factors, instead of relating the contribution of the NEWT projection modes to the system-level tuned normal modes, are computed to relate the projection modes to the PRIME basis. Thus, the small mistuning component is eventually reduced and carried by the PRIME ROMs, following the same pristine, rogue, and interface partitions.

Chapter III develops a novel ROM that can predict the nonlinear steady-state forced responses of blisks with frictional ring dampers. The blisk-damper systems are projected onto a small mode basis that mimics the relative motions between the contact surfaces under stick and slip conditions, named as the basis of Coherent Ring Damper (CoRiD). The resulting ROMs are expressed in a HBM formulation. The frictional contact between the ring and the blisk contains contact node pairs that are distributed across the contact surfaces. Each node pair can be modeled by a 3D sophisticated contact model developed by Yang et al. [30]. However, to accelerate the computations, a simplified 3D contact model, consisting of two independent 1D macro-slip models and an additional spring accounting for normal load variations, is adopted in this study. The HFT method is used to solve the nonlinear

equations of motion, where in the frequency domain, the nonlinear equations of motion are expressed using only a few coordinates. Also, this work explores the effectiveness of ring dampers in dissipating vibrational energy when forced responses are amplified by the presence of mistuning. In this study, a method based on CMM is developed to construct the mistuning components of the blisk-damper systems directly in the ROM coordinates [1, 2, 7]. This method enables the developed ROMs to capture the forced responses of mistuned blisk-damper systems, and to explore the correlations between mistuning and the effectiveness of the frictional ring dampers.

Chapter IV further extends the CoRiD method by strategically Integrating it into the PRIME frame. The resulted ROM is used to study the effectiveness of frictional ring dampers when the blisk suffers from high-level forced responses due to simultaneous large and small mistuning. The PRIME method is used to compute the system normal mode shapes of a mistuned blisk-damper system with the two types of contact status, which are further used as the input to the CoRiD method to form the mode basis for system reduction.

Chapter V studies the effect of variations of damper geometry on its effectiveness in dissipating vibrational energy from the blisks. In this study, the geometry of a V-shaped damper is parametrized following a volume constraint. A parametric study is performed by varying two of the geometric parameters simultaneously at a time to explore the trade-offs among dimensions of the damper. Moreover, a series of sensitivity analyses along each of the damper dimensions are performed to reveal the optimal geometric parameters that the damper should possess to reach its maximum effectiveness. Based on the results from the sensitivity analyses, a set of damper design guidelines are also proposed.

Chapter VI offers a brief summary of contributions of the work in this dissertation, and suggests ideas for future work.

CHAPTER 2

Models for Blisks with Large Blends and Small Mistuning

2.1 Introduction

Small deviations of the structural properties of individual sectors of blisks, referred to as mistuning, can lead to localization of vibration energy and drastically increased forced responses. Similar phenomena are observed in blisks with large damages or repair blends. Such deviations are best studied statistically because they are random. In the absence of cyclic symmetry, the computational cost to predict the vibration behavior of blisks becomes prohibitively high. That has lead to the development of various ROMs. Most of the existing approaches focus heavily on modeling small mistuning [1, 2, 8–17]. Among the limited methods that are developed for modeling blisks with large mistuning, most of them [1–5] involve repetitive CB-CMS condensation of the full-order FE models. This process is computationally expensive and thus not ideal to be used for statistical analysis to study the random nature of mistuning.

This work discusses a reduced-order modeling method for blisks with both large and small mistuning, which requires low computational effort. This method utilizes the PRIME method to model large blends. PRIME uses only sector-level cyclic modes strategically combined together to create a reduction basis which yields ROMs that efficiently and accurately model large mistuning. To model small mistuning, NEWT is integrated with PRIME, resulting in N-PRIME, which requires only sector-level calculations to create a ROM which captures both small and large mistuning with minimized computational effort.

This section is organized as follows. The PRIME and NEWT methods are briefly reviewed in the next section, followed by the formulation of the new approach, called N-PRIME, as it is a hybrid of the PRIME and the NEWT methods. A stress mode technique is also proposed to recover fast the stress distributions of forced responses. The combined effects of large blends and small mistuning are studied using N-PRIME for a dual flow

path system and for a conventional blisk. A typical example of the dual-flow path system is shown in Fig. 2.1, which is also referred to as the FLADE™system. The accuracy of the N-PRIME method is validated against full-order finite element analyses for both natural and forced response computations, including displacement amplitudes and surface stresses. Results reveal that N-PRIME is capable of accurately predicting the dynamics of a blisk with severely large mistuning, along with small random mistuning throughout each sector. Also, N-PRIME can accurately capture modes with highly localized motions. A statistical analysis is performed to study the effects of random mistuning on both natural frequencies and forced responses and reveals that 1) new clusters of mistuned natural frequencies exist and cannot be treated as small deviations from nominal frequencies, and 2) unexpectedly high amplifications of forced responses exist, showing 3 to 5 times higher responses compared to the nominal system.

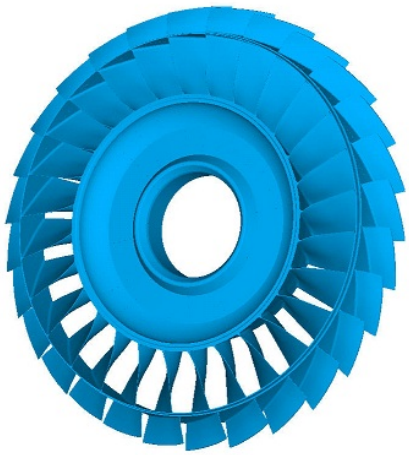

Figure 2.1: A finite element model of the FLADE™system

2.2 Methodology

In this section, two reduced-order modeling techniques which contribute to the development of the N-PRIME method are briefly reviewed. Also, the process of integrating NEWT into the PRIME work frame is discussed. Next, forced response computations are formulated based on the developed N-PRIME ROM, with the stress mode technique included to recover stress distributions fast.

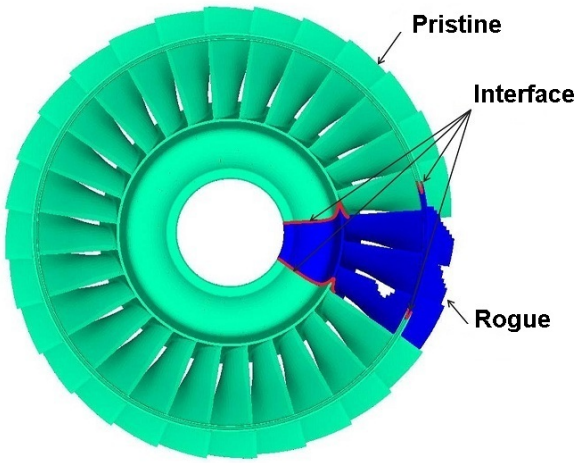

Figure 2.2: A mistuned dual-flow path system partitioned by PRIME

2.2.1 Pristine Rogue Interface Modal Expansion

N-PRIME is constructed under the frame of pristine-rogue-interface modal expansion, or PRIME, which is designed to solve large mistuning problems. Consider the equation of motion of a mistuned blisk with harmonic forcing as

$$\left[-\omega^2\mathbf{M} + (1 + j\gamma)\mathbf{K}\right]\mathbf{x} = \mathbf{f}, \tag{2.1}$$

where $\mathbf{M}$ and $\mathbf{K}$ are the system mass and stiffness matrices, γ is the structural damping ratio, and $\mathbf{f}$ is the amplitude of the harmonic forcing. This mistuned system is partitioned into three components: a pristine component which contains the DOFs of sectors that are structurally identical to a nominal sector, a rogue component which contains the DOFs of sectors that are largely mistuned, and an interface component that connects the pristine and rogue components (Fig. 2.2). The partitioned mass and stiffness matrices can be expressed as

$$\mathbf{M} = \begin{bmatrix} \mathbf{M}^{\mathrm{PP}} & \mathbf{M}^{\mathrm{PR}} & \mathbf{M}^{\mathrm{PI}} \\ \mathbf{M}^{\mathrm{RP}} & \mathbf{M}^{\mathrm{RR}} & \mathbf{M}^{\mathrm{RI}} \\ \mathbf{M}^{\mathrm{IP}} & \mathbf{M}^{\mathrm{IR}} & \mathbf{M}^{\mathrm{II}} \end{bmatrix}, \qquad \mathbf{K} = \begin{bmatrix} \mathbf{K}^{\mathrm{PP}} & \mathbf{K}^{\mathrm{PR}} & \mathbf{K}^{\mathrm{PI}} \\ \mathbf{K}^{\mathrm{RP}} & \mathbf{K}^{\mathrm{RR}} & \mathbf{K}^{\mathrm{RI}} \\ \mathbf{K}^{\mathrm{IP}} & \mathbf{K}^{\mathrm{IR}} & \mathbf{K}^{\mathrm{II}} \end{bmatrix}. \tag{2.2}$$

It has been observed in previous work [2, 3] that in the presence of large mistuning, the assumption suggested by Yang et al. [14] that the mistuned mode shapes can be expressed as a linear a combination of tuned mode shapes no longer holds. Instead, the PRIME method is based on a relaxed assumption, namely that the pristine DOFs of the mistuned mode shapes can be represented by a linear combination of the corresponding DOFs of

cyclic tuned mode shapes ($\mathbf{\Phi}^{\mathrm{P}}$). Similarly, the rogue DOFs of the mistuned mode shapes can be represented by a linear combination of the corresponding DOFs of cyclic rogue mode shapes ($\mathbf{\Phi}^{\mathrm{R}}$). With such assumption, the PRIME mode basis can be assembled as

$$\mathbf{\Phi}^{\mathrm{PRI}} = \begin{bmatrix} \mathbf{\Phi}^{\mathrm{P}} & \mathbf{0} & \mathbf{0} \\ \mathbf{0} & \mathbf{\Phi}^{\mathrm{R}} & \mathbf{0} \\ \mathbf{0} & \mathbf{0} & \mathbf{\Phi}^{\mathrm{I}} \end{bmatrix}. \tag{2.3}$$

Note that $\mathbf{\Phi}^{\mathrm{I}}$ represents interface mode shapes added to the PRIME mode basis to characterize the motion of the interface. The motion of the interface is conditioned so that we enforce displacement compatibility across the boundaries between the pristine and rogue components. This displacement compatibility is enforced by ensuring the same generalized coordinate amplitude along all independent directions in a subspace that is the intersection of two subspaces one ofr each of the two sectors at that interface. Projecting the mistuned system onto the PRIME basis yields the reduced-order mass and stiffness matrices as

$$\begin{aligned} \mathbf{M}_{\mathrm{PRI}} &= {\mathbf{\Phi}^{\mathrm{PRI}}}^{\mathrm{T}} \mathbf{M} \mathbf{\Phi}^{\mathrm{PRI}} \\ &= \begin{bmatrix} {\mathbf{\Phi}^{\mathrm{P}}}^{\mathrm{T}} \mathbf{M}^{\mathrm{PP}} \mathbf{\Phi}^{\mathrm{P}} & {\mathbf{\Phi}^{\mathrm{P}}}^{\mathrm{T}} \mathbf{M}^{\mathrm{PR}} \mathbf{\Phi}^{\mathrm{R}} & {\mathbf{\Phi}^{\mathrm{P}}}^{\mathrm{T}} \mathbf{M}^{\mathrm{PI}} \mathbf{\Phi}^{\mathrm{I}} \\ {\mathbf{\Phi}^{\mathrm{R}}}^{\mathrm{T}} \mathbf{M}^{\mathrm{RP}} \mathbf{\Phi}^{\mathrm{P}} & {\mathbf{\Phi}^{\mathrm{R}}}^{\mathrm{T}} \mathbf{M}^{\mathrm{RR}} \mathbf{\Phi}^{\mathrm{R}} & {\mathbf{\Phi}^{\mathrm{R}}}^{\mathrm{T}} \mathbf{M}^{\mathrm{RI}} \mathbf{\Phi}^{\mathrm{I}} \\ {\mathbf{\Phi}^{\mathrm{I}}}^{\mathrm{T}} \mathbf{M}^{\mathrm{IP}} \mathbf{\Phi}^{\mathrm{P}} & {\mathbf{\Phi}^{\mathrm{I}}}^{\mathrm{T}} \mathbf{M}^{\mathrm{IR}} \mathbf{\Phi}^{\mathrm{R}} & {\mathbf{\Phi}^{\mathrm{I}}}^{\mathrm{T}} \mathbf{M}^{\mathrm{II}} \mathbf{\Phi}^{\mathrm{I}} \end{bmatrix}, \\ \mathbf{K}_{\mathrm{PRI}} &= {\mathbf{\Phi}^{\mathrm{PRI}}}^{\mathrm{T}} \mathbf{K} \mathbf{\Phi}^{\mathrm{PRI}} \\ &= \begin{bmatrix} {\mathbf{\Phi}^{\mathrm{P}}}^{\mathrm{T}} \mathbf{K}^{\mathrm{PP}} \mathbf{\Phi}^{\mathrm{P}} & {\mathbf{\Phi}^{\mathrm{P}}}^{\mathrm{T}} \mathbf{K}^{\mathrm{PR}} \mathbf{\Phi}^{\mathrm{R}} & {\mathbf{\Phi}^{\mathrm{P}}}^{\mathrm{T}} \mathbf{K}^{\mathrm{PI}} \mathbf{\Phi}^{\mathrm{I}} \\ {\mathbf{\Phi}^{\mathrm{R}}}^{\mathrm{T}} \mathbf{K}^{\mathrm{RP}} \mathbf{\Phi}^{\mathrm{P}} & {\mathbf{\Phi}^{\mathrm{R}}}^{\mathrm{T}} \mathbf{K}^{\mathrm{RR}} \mathbf{\Phi}^{\mathrm{R}} & {\mathbf{\Phi}^{\mathrm{R}}}^{\mathrm{T}} \mathbf{K}^{\mathrm{RI}} \mathbf{\Phi}^{\mathrm{I}} \\ {\mathbf{\Phi}^{\mathrm{I}}}^{\mathrm{T}} \mathbf{K}^{\mathrm{IP}} \mathbf{\Phi}^{\mathrm{P}} & {\mathbf{\Phi}^{\mathrm{I}}}^{\mathrm{T}} \mathbf{K}^{\mathrm{IR}} \mathbf{\Phi}^{\mathrm{R}} & {\mathbf{\Phi}^{\mathrm{I}}}^{\mathrm{T}} \mathbf{K}^{\mathrm{II}} \mathbf{\Phi}^{\mathrm{I}} \end{bmatrix}. \end{aligned} \tag{2.4}$$

Note that $\mathbf{\Phi}^{\mathrm{P}}$ and $\mathbf{\Phi}^{\mathrm{R}}$ contain sector-level mode shapes obtained from cyclic modal analyses. Also, the mass and stiffness matrices of a cyclically symmetric blisk, $\mathbf{M}$ and $\mathbf{K}$, are block-diagonal for usual node numbering. Thus, constructing the reduced-order model involves only sector-level computations.

PRIME is also capable of constructing ROMs for systems with simultaneous large and small mistuning. Consider the equation of motion of a blisk with both large and small mistuning

$$\left[-\omega^2(\mathbf{M} + \mathbf{M}^{\delta}) + (1 + j\gamma)(\mathbf{K} + \mathbf{K}^{\delta})\right]\mathbf{x} = \mathbf{f}, \tag{2.5}$$

where $\mathbf{M}^{\delta}$ and $\mathbf{K}^{\delta}$ are the mass and stiffness matrices of small mistuning components. Projecting the mistuned system onto PRIME mode basis transforms the equation of motion

into the reduced-order domain as

$$\begin{aligned}&\Big[-\omega^2(\mathbf{M}^{\mathrm{PRI}}+\mathbf{\Phi}^{\mathrm{PRI}^{\mathrm{T}}}\mathbf{M}^{\delta}\mathbf{\Phi}^{\mathrm{PRI}})+\\&(1+j\gamma)(\mathbf{K}^{\mathrm{PRI}}+\mathbf{\Phi}^{\mathrm{PRI}^{\mathrm{T}}}\mathbf{K}^{\delta}\mathbf{\Phi}^{\mathrm{PRI}})\Big]\mathbf{p}^{\mathrm{PRI}}=\mathbf{\Phi}^{\mathrm{PRI}^{\mathrm{T}}}\mathbf{f},\end{aligned} \tag{2.6}$$

and the mass and stiffness matrices of the mistuned system are thus reduced to the following form

$$\begin{aligned}\mathbf{M}^{\mathrm{red}}&=\mathbf{M}^{\mathrm{PRI}}+\mathbf{\Phi}^{\mathrm{PRI}^{\mathrm{T}}}\mathbf{M}^{\delta}\mathbf{\Phi}^{\mathrm{PRI}},\\\mathbf{K}^{\mathrm{red}}&=\mathbf{K}^{\mathrm{PRI}}+\mathbf{\Phi}^{\mathrm{PRI}^{\mathrm{T}}}\mathbf{K}^{\delta}\mathbf{\Phi}^{\mathrm{PRI}}.\end{aligned} \tag{2.7}$$

The formulation shown by Eqns. (2.6) and (2.7) is acceptable in terms of accuracy. However, in the context of statistical analyses, the process of repetitively projecting the small mistuning component onto the PRIME basis may require a heavy computational effort. To model small mistuning more efficiently, Madden et al. [7] integrated a modified CMM [2,3] approach into PRIME (C-PRIME). The PRIME mode basis is projected onto a set of a few CB modes computed for a pristine sector and one of each of the rogue sectors. The projection is expressed as

$$\begin{aligned}\mathbf{\Phi}^{\mathrm{P}}_{j}&=\mathbf{\Phi}^{\mathrm{P}}_{cb}\mathbf{q}^{\mathrm{P}}_{cb,j},\\\mathbf{\Phi}^{\mathrm{R}}_{j}&=\mathbf{\Phi}^{\mathrm{R}}_{cb,j}\mathbf{q}^{\mathrm{R}}_{cb,j}.\end{aligned} \tag{2.8}$$

If the j^{th} sector of the blisk system is pristine, $\mathbf{\Phi}_{cb}$ contains the CB modes of a pristine sector. The participation factor $\mathbf{q}^{\mathrm{P}}_{cb,j}$ represents the contributions of the pristine CB modes to the mode shapes of the j^{th} sector in the PRIME mode basis. Similarly, if the j^{th} sector is rogue, $\mathbf{\Phi}^{\mathrm{R}}_{cb,j}$ contains the CB mode shapes of that rogue sector, and the participation factors $\mathbf{q}^{\mathrm{R}}_{cb,j}$ represents contributions of the rogue CB modes to the PRIME basis. The ROM formulated by C-PRIME is expressed as

$$\begin{aligned}\mathbf{M}^{\mathrm{red}}&=\mathbf{M}^{\mathrm{PRI}}+\sum_{j=1}^{N}\mathbf{q}^{\mathrm{T}}_{cb,j}\mathbf{\Phi}_{cb,j}{}^{\mathrm{T}}\mathbf{M}^{\delta}_{j}\mathbf{\Phi}_{cb,j}\mathbf{q}_{cb,j},\\\mathbf{K}^{\mathrm{red}}&=\mathbf{K}^{\mathrm{PRI}}+\sum_{j=1}^{N}\mathbf{q}^{\mathrm{T}}_{cb,j}\mathbf{\Phi}_{cb,j}{}^{\mathrm{T}}\mathbf{K}^{\delta}_{j}\mathbf{\Phi}_{cb,j}\mathbf{q}_{cb,j}.\end{aligned} \tag{2.9}$$

Note that in Eqn. (2.9), the projection of the mistuning components onto the CB modes, and the subsequent transformation into the PRIME modal coordinates by participation factors, are formulated as a sum of sector-level projections over the number N of sectors,

where $\mathbf{M}_j^{\delta}$ and $\mathbf{K}_j^{\delta}$ are the mistuning components of the j^{th} sector. $\mathbf{\Phi}_{cb,j}$ represents the set of CB modes of the j^{th} sector, which is selected from either $\mathbf{\Phi}_{cb}^{\text{P}}$ or $\mathbf{\Phi}_{cb,j}^{\text{R}}$, depending on whether the j^{th} sector is a pristine or one of the rogue sectors. $\mathbf{q}_{cb,j}$ contains the corresponding participation factors of the j^{th} sector. The integration of CMM into PRIME separates the construction of ROM for small mistuning from that of large mistuning. Since the blade motions are in general dominated by one or two CB modes, the computational effort required to assemble the reduced-order mistuning matrices is significantly reduced. However, by using CB modes as the mode basis for projection, CMM assumes little or no motion at the root of each blade. This assumption fails when disk-dominated modes are excited. Moreover, CB modes contain only blade DOFs, which restricts mistuning to exist only on the blade components. Also, extracting CB modes requires a clear definition of the root of a blade. These requirements render CMM inapplicable to dual-flow path systems, where one sector may contain multiple components with distinct mistuning patterns, and the root of a blade is not readily defined.

2.2.2 Nodal Energy Weighted Transformation

To explore the dynamics of dual-flow path systems, and to address the limitations of the C-PRIME method, the NEWT method is adopted in this study. Consider a system that has small mistuning only. The mistuning components $\mathbf{M}^{\delta}$ and $\mathbf{K}^{\delta}$ are projected onto the system-level tuned modes $\mathbf{\Phi}^0$ as follows

$$\begin{aligned} \mathbf{M}^{\text{red},\delta} &= {\mathbf{\Phi}^0}^{\text{T}} \mathbf{M}^{\delta} \mathbf{\Phi}^0, \\ \mathbf{K}^{\text{red},\delta} &= {\mathbf{\Phi}^0}^{\text{T}} \mathbf{K}^{\delta} \mathbf{\Phi}^0. \end{aligned} \tag{2.10}$$

Instead of CB modes used by CMM [2,3], NEWT strategically selects a subset of cyclic mode pairs $\mathbf{A}^0$ and $\mathbf{B}^0$ of a tuned sector as the projection basis. The system-level tuned mode shapes of the j^{th} sector can be expressed as a linear combination of the selected cyclic mode pairs as

$$\mathbf{\Phi}_j^0 = \mathbf{A}^0 \mathbf{q}_j + \mathbf{B}^0 \mathbf{r}_j, \tag{2.11}$$

where $\mathbf{\Phi}_j^0$ contains the system-level tuned mode shapes corresponding to the DOFs of the j^{th}sector. Modal participation factors $\mathbf{q}_j$ and $\mathbf{r}_j$ represent the contributions of the cyclic mode pairs, $\mathbf{A}^0$ and $\mathbf{B}^0$ respectively, to each mode in $\mathbf{\Phi}_j^0$. Substituting Eqn. (2.11) into

Eqn. (2.10) yields

$$\begin{aligned}\mathbf{M}^{\mathrm{red},\delta} &= \sum_{j=1}^{N} (\mathbf{A}^0\mathbf{q}_j + \mathbf{B}^0\mathbf{r}_j)^{\mathrm{T}} \mathbf{M}_j^{\delta} (\mathbf{A}^0\mathbf{q}_j + \mathbf{B}^0\mathbf{r}_j), \\ \mathbf{K}^{\mathrm{red},\delta} &= \sum_{j=1}^{N} (\mathbf{A}^0\mathbf{q}_j + \mathbf{B}^0\mathbf{r}_j)^{\mathrm{T}} \mathbf{K}_j^{\delta} (\mathbf{A}^0\mathbf{q}_j + \mathbf{B}^0\mathbf{r}_j).\end{aligned} \tag{2.12}$$

Note that a mode selection process is also proposed by Fitzner et al. [17], based on the assumption that within one mode family, cyclic modes associated with higher nodal diameters share similar shapes, and are mutually dependent on each other. Therefore, a strategically selected subset of cyclic mode shapes can span the full modal space, and the projection basis formed by NEWT can be further reduced.

2.2.3 N-PRIME: Extending PRIME with a Modified NEWT

Due to the presence of large mistuning, the original NEWT projection basis, formed by only the tuned cyclic modes, becomes insufficient. Therefore, the NEWT basis is modified to include not only the cyclic mode pairs of a pristine sector, but also the those of each rogue sector. The projection from the PRIME mode basis onto the modified NEWT basis for the j^{th} sector possesses either of the following forms

$$\begin{aligned}\mathbf{\Phi}_j^{\mathrm{P}} &= \mathbf{A}^{\mathrm{P}}\mathbf{q}_j^{\mathrm{P}} + \mathbf{B}^{\mathrm{P}}\mathbf{r}_j^{\mathrm{P}}, \\ \mathbf{\Phi}_j^{\mathrm{R}} &= \mathbf{A}_j^{\mathrm{R}}\mathbf{q}_j^{\mathrm{R}} + \mathbf{B}_j^{\mathrm{R}}\mathbf{r}_j^{\mathrm{R}}.\end{aligned} \tag{2.13}$$

Similar to the C-PRIME method, the mode shapes of the j^{th} sector in the PRIME mode basis are projected onto the cyclic mode pairs. Depending on the sector type, if the j^{th} sector is pristine, the cyclic mode pairs are selected from $\mathbf{A}^{\mathrm{P}}$ and $\mathbf{B}^{\mathrm{P}}$, and the modal participation factors $\mathbf{q}_j^{\mathrm{P}}$ and $\mathbf{r}_j^{\mathrm{P}}$ represent the contribution of the pristine cyclic mode pairs to the mode shapes of the j^{th} sector in the PRIME mode basis. Similarly, if the j^{th} sector is rogue, $\mathbf{A}_j^{\mathrm{R}}$ and $\mathbf{B}_j^{\mathrm{R}}$ contain the cyclic mode pairs of the rogue sector, and modal participation factors $\mathbf{q}_j^{\mathrm{R}}$ and $\mathbf{r}_j^{\mathrm{R}}$ represent the contribution of the rogue cyclic mode pairs to the mode shapes of the j^{th} sector in the PRIME mode basis.

Note that the above projection involves expanding cyclic mode pairs to a specific sector. This process requires adjusting the phase angle based on the sector index as well as the nodal diameter (or harmonic index). Such adjustment is implicitly carried by the participation factors, and indicated by their subscripts j = sector number. Substituting Eqn. (2.13)

into Eqn. (2.6) results in the following reduced-order matrices

$$\begin{aligned}\mathbf{M}^{\text{red}} &= \mathbf{M}^{\text{PRI}} + \sum_{j=1}^{N} (\mathbf{A}_j \mathbf{q}_j + \mathbf{B}_j \mathbf{r}_j)^{\text{T}} \mathbf{M}_j^{\delta} (\mathbf{A}_j \mathbf{q}_j + \mathbf{B}_j \mathbf{r}_j), \\ \mathbf{K}^{\text{red}} &= \mathbf{K}^{\text{PRI}} + \sum_{j=1}^{N} (\mathbf{A}_j \mathbf{q}_j + \mathbf{B}_j \mathbf{r}_j)^{\text{T}} \mathbf{K}_j^{\delta} (\mathbf{A}_j \mathbf{q}_j + \mathbf{B}_j \mathbf{r}_j).\end{aligned} \tag{2.14}$$

Equation (2.14) shows ROM matrices that are capable of efficiently modeling both large and small mistuning for complex structures such as dual-flow path systems. This novel reduced-order modeling technique is developed by integrating a modified NEWT method into the current PRIME work frame, and is thus named N-PRIME. The mistuning components of the N-PRIME ROM expressed in Eqn. (2.14) are computed as a sum of sector-level projections. Note that the NEWT basis in general contains much fewer modes than the PRIME basis. And since the modal participation factors can be pre-calculated, the computational effort required to formulate ROMs for small mistuning is minimal.

2.2.4 Forced Responses and Fast Stress Recovery

With the ROM constructed by N-PRIME, forced response computations can be formulated as

$$\left[-\omega^2 \mathbf{M}^{\text{red}} + (1 + j\gamma)\mathbf{K}^{\text{red}}\right] \mathbf{p}^{\text{PRI}} = {\mathbf{\Phi}^{\text{PRI}}}^{\text{T}} \mathbf{f}, \tag{2.15}$$

and the physical displacement responses can be extracted as

$$\mathbf{x} = \mathbf{\Phi}^{\text{PRI}} \mathbf{p}^{\text{PRI}}. \tag{2.16}$$

To explore the effects of simultaneous large and small mistuning on forced responses, a metric within which the effect of mistuning is measured must be defined. It is well known that in the presence of mistuning, strain energy localization may occur which leads to drastic increases in forced responses. Thus, it is insightful to compare the maximum magnitude of displacements throughout the mistuned system with that throughout a tuned system, under the same forcing conditions. This metric is called the amplification factor, and is defined as

$$\text{AF}_{\text{x}} = \frac{\max_{\omega}(\max_{i=1}^{\text{N}_{\text{node}}}(\|\mathbf{x}_i^{\text{m}}\|))}{\max_{\omega}(\max_{j=1}^{\text{N}_{\text{node}}}(\|\mathbf{x}_j^{0}\|))}, \tag{2.17}$$

where N_{node} is the total number of nodes in an entire blisk, and ω is the forcing frequency.

Superscript m stands for a mistuned system, whereas 0 stands for a tuned system. Note that the definition of the amplification factor proposed here does not focus on one or a few pre-select response nodes, despite the fact that the maximum responses of a tuned and a mistuned systems can occur at different locations. This is intentionally done to account for localization of strain energy and highly confined motion caused by mistuning. Such localization can occur at different locations from where the maximum response of a tuned system is. If only a single or a few response nodes are included for analyses, the amplification factor can be underestimated. For low order mode families, an amplification factor based on specified points on the blade would be very similar in the case of small mistuning. However, in the case of large mistuning, that point may not even exist on all blades, so we defined an amplification factor based on the maximum response in the entire sector.

In addition to displacements, stress distributions of mistuned systems under external forcing are investigated to further reveal the effects of mistuning. Instead of performing a full-order harmonic analysis, it is ideal to re-use the developed N-PRIME ROM to compute stress responses. This can be achieved with the following observation. Substituting Eqn. (2.16) into the definition of strain and stresses yields the following expressions

$$\begin{aligned}\epsilon_{kl} &= \frac{1}{2}(\mathbf{x}_{k,l} + \mathbf{x}_{l,k}) \\ &= \frac{1}{2}((\mathbf{\Phi}_k^{\mathrm{PRI}}\mathbf{p}^{\mathrm{PRI}})_{,l} + (\mathbf{\Phi}_l^{\mathrm{PRI}}\mathbf{p}^{\mathrm{PRI}})_{,k}) \\ &= \frac{1}{2}(\mathbf{\Phi}_{k,l}^{\mathrm{PRI}} + \mathbf{\Phi}_{l,k}^{\mathrm{PRI}})\mathbf{p}^{\mathrm{PRI}},\end{aligned} \tag{2.18}$$

$$\begin{aligned}\sigma_{kl} &= \mathbf{C}_{klmn}\epsilon_{mn} \\ &= \frac{1}{2}\mathbf{C}_{klmn}(\mathbf{\Phi}_{m,n}^{\mathrm{PRI}} + \mathbf{\Phi}_{n,m}^{\mathrm{PRI}})\mathbf{p}^{\mathrm{PRI}},\end{aligned} \tag{2.19}$$

where $\mathbf{C}$ is the elasticity tensor, and $\mathbf{x}_k$ represents the displacements in the k^{th} direction. With the above relationship among stresses, strain, and PRIME modal participation factors, it is convenient to define and pre-compute the PRIME stress modes $\mathbf{\Psi}_{kl}^{\mathrm{PRI}}$ as

$$\mathbf{\Psi}_{kl}^{\mathrm{PRI}} = \frac{1}{2}\mathbf{C}_{klmn}(\mathbf{\Phi}_{m,n}^{\mathrm{PRI}} + \mathbf{\Phi}_{n,m}^{\mathrm{PRI}}), \tag{2.20}$$

and the stress distributions of forced responses can be computed easily as a linear combination of $\mathbf{\Psi}_{kl}^{\mathrm{PRI}}$ as

$$\sigma_{kl} = \mathbf{\Psi}_{kl}^{\mathrm{PRI}}\mathbf{p}^{\mathrm{PRI}}. \tag{2.21}$$

The above formulation takes advantage of the developed N-PRIME ROM, and the modal participation factors obtained from the displacement responses. Thus, this formulation involves only sector-level computations, and requires minimal input parameters. In practice, the highest stresses are usually found on the surfaces of the blade components, where the largest strain occurs. This assumption reduces the size of each stress mode, and accelerates the stress recovery process in two ways. First, surface stresses are extracted at the center point of each surface element. The number of surface elements is much smaller than the total number of nodes. Also, compared with six stress components possessed by each node, only three in-plane stress components are extracted for each surface element. It should be noted that the stress recovery procedures demonstrated in this paper is not restricted to the N-PRIME method. For a mode shape in any reduction basis, a corresponding stress mode shape can be obtained. The stress distribution (elements of the stress tensor) resulting from forced responses can be expressed as a linear combination of the stress mode shapes.

Similar to the magnitude of displacement used in formulating the amplification factor of displacements, Von-Mises stresses are adopted in this study to develop the stress amplification factor. For a 2D planar case, Von-Mises stresses at the center point of each surface element is defined as

$$\sigma_{\mathrm{VM}}^2 = \|\sigma_k\|^2 + \|\sigma_l\|^2 + 3\|\sigma_{kl}\|^2 - \frac{\bar{\sigma}_k\sigma_l + \sigma_k\bar{\sigma}_l}{2}, \tag{2.22}$$

where σ_{VM} represents the Von-Mises stresses, and $\bar{\sigma}_i$ and $\bar{\sigma}_j$ are the complex conjugates of corresponding in-plane stress components. Comparing the maximum Von-Mises stresses over all blade surface elements of a mistuned system with that of a tuned system. The stress amplification factor can be defined as

$$\mathrm{AF}_\sigma = \frac{\max_\omega(\max_{i=1}^{\mathrm{N_{node}}}(\sigma_{\mathrm{VM},i}^{\mathrm{m}}))}{\max_\omega(\max_{i=1}^{\mathrm{N_{node}}}(\sigma_{\mathrm{VM},i}^{0}))}. \tag{2.23}$$

The stress amplification factor is defined in the same way as for the displacement amplification factor. The same arguments apply here for stresses as those for displacements. In fact, for stresses, this is an even more important issue because the location of the maximum stress can significantly change due to the large blends.

2.3 Results and Discussion

In this section, the N-PRIME approach is applied to two distinct models, including a simplified academic model of a conventional blisk and a more complex model of a dual-flow path system. Mistuned natural frequencies are computed for both models, and compared with the results generated by the C-PRIME method, where applicable. Forced responses are computed for both systems to extract the displacements and stresses under traveling wave excitations. For both analyses, the results are validated against the full-order finite element analysis performed in ANSYS. A statistical analysis is performed on the dual-flow path system to compute the probability distributions of 1) mistuned natural frequencies, and 2) displacement and stress amplification factors by sampling the dual-flow path system over a large number of simultaneous large and small mistuning patterns.

2.3.1 Conventional Blisks

Figure 2.3 shows a simplified academic model of a conventional blisk, referred to as the UM Validation Blisk. Small material mistuning is applied to each blade by varying its Young's modulus by a small percentage from the nominal value. Such variations are determined randomly following a normal distribution with a 0 mean and a 2% standard deviation. Large mistuning is created by removing a significant volume of material from one of the blades. In this study, three cases of large mistuning are considered, each of which involves a different volume of material removed from a blade tip, as shown in Fig. 2.4.

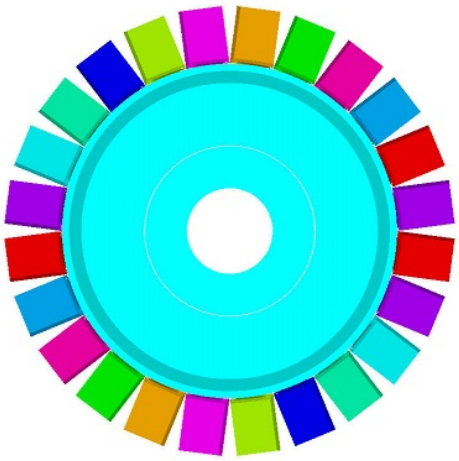

Figure 2.3: A finite element model of the UM Validation Blisk

(a) 10% Material (b) 20% Material (c) 30% Material

Figure 2.4: Large mistuning: 10%, 20% and 30% material removed from a blade component

2.3.1.1 Free Responses

Consider a case with 10% material removed from one of the blades. 186 PRIME modes for the pristine and each of the rogue sectors are included to compute the first 102 natural frequencies of the mistuned blisk. Figure 2.5a shows the error in natural frequencies computed by the C-PRIME method. 5 CB modes are used to form the CMM mode basis for the pristine sector and each one of the rogue sectors (up to 20 kHz). These results are compared with the errors in the natural frequencies provided by the N-PRIME method, with 5 cyclic modes (selected within the frequency range, up to 20 kHz) used to form the NEWT projection basis. These cyclic modes are associated with the highest nodal diameter, and are hereafter referred to as the N/2 modes. At the first glance, results generated by N-PRIME are not superior to those computed by C-PRIME. However, with more CB modes adopted by C-PRIME (37 modes for each sector, up to 120 kHz), its accuracy is not significantly improved (Fig. 2.5b). In contrast, with 37 cyclic modes adopted for each sector, N-PRIME provides a much better accuracy. With all 186 cyclic modes included in the NEWT projection basis, hereafter referred to as the exhaustive projection, the maximum error of natural frequencies is reduced to a value less than 0.011% (Fig. 2.5c), which is approximately three times lower than the maximum error in the results computed by C-PRIME with either of the two sets of CB modes.

Figure 2.6 shows the relative error in the maximum displacement of each mode shape computed by the ROMs. A similar trend is observed in the case of mode shapes, where the N/2 mode basis generates the highest error of approximately 3.5%. The bases formed by 5 and 37 CB modes result in same level of accuracy, with a maximum error of approximately 1.3%. N-PRIME with exhaustive projection results in a lowest error of 0.5%, which indicates a good accuracy of this basis in predicting mistuned mode shapes.

As mentioned previously, mistuning can lead to strain energy localization, which typi-

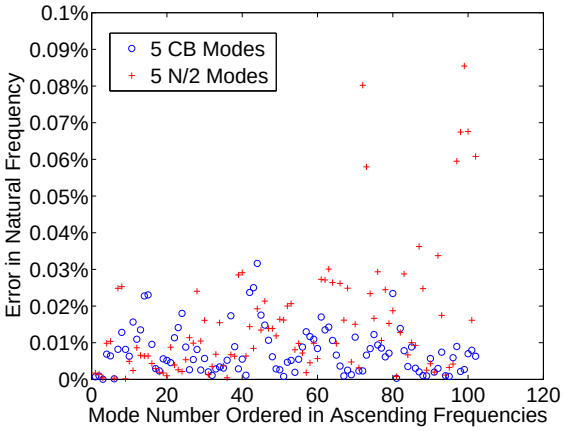

(a) 5 Projection Modes

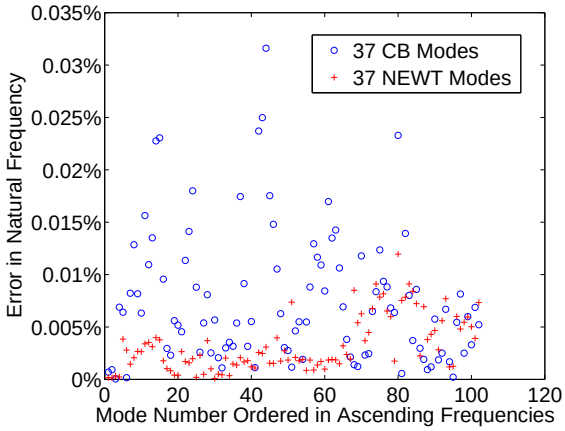

(b) 37 Projection Modes

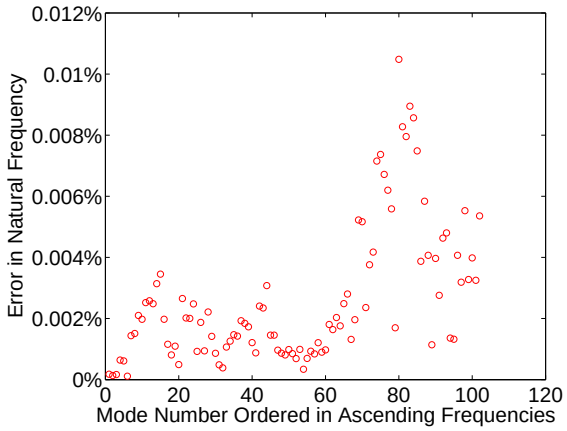

(c) N-PRIME Exhaustive Projection

Figure 2.5: Relative errors in frequencies for the UM Validation Blisk: C-PRIME and N-PRIME with different small mistuning projection bases

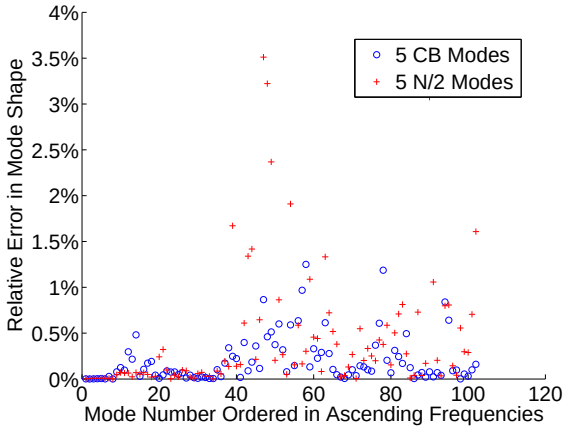

(a) 5 Projection Modes

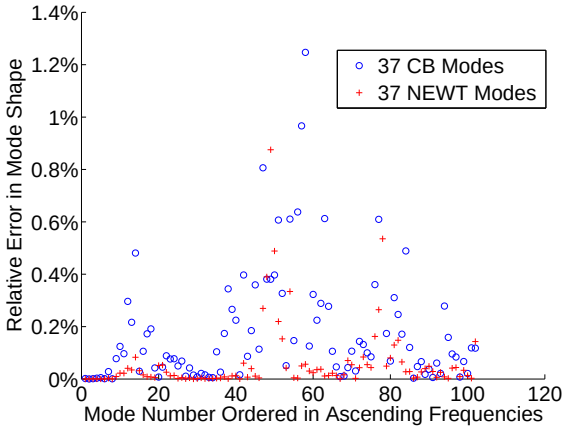

(b) 37 Projection Modes

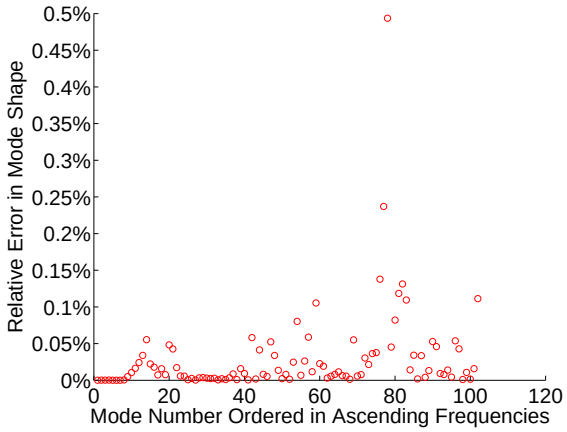

(c) N-PRIME Exhaustive Projection

Figure 2.6: Relative errors in mode shapes for the UM Validation Blisk: C-PRIME and N-PRIME with different small mistuning projection bases

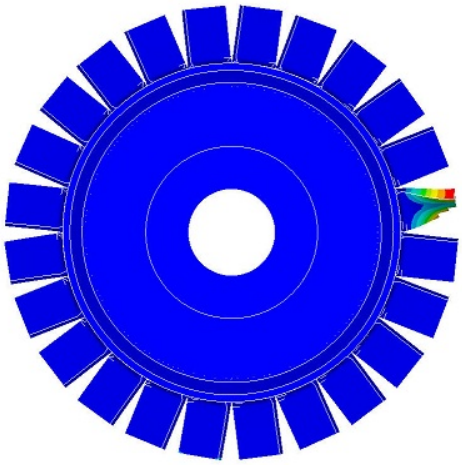

Figure 2.7: A mode shape with highly localized blade motion (mode index 71)

cally results in mode shapes with localized and significantly amplified motions. Figure 2.7 shows the mode shape of index 71. Note that the error carried by the ROM-predicted frequency for this localized mode remains small, which is less than 0.001%, and demonstrates that N-PRIME is capable of capturing such extreme cases.

Due to its better accuracy, N-PRIME with exhaustive mode basis is used to compute the natural frequencies for the UM Validation Blisk with 20% and 30% material removed from one blade. Figure 2.8 shows the error in natural frequencies of the ROM-predicted results. Note that in an extreme case of large mistuning, where 30% blade material is removed from the blade, N-PRIME remains capable of accurately capturing the natural frequencies, with a maximum error that is less than 0.013%.

Figure 2.9 shows the shift of natural frequencies induced by mistuning, from the frequencies of a pristine blisk. Compared to the maximum shift of 15%, and an average shift of 1.14%, the relative error in natural frequencies, provided by both C-PRIME and N-PRIME, is significantly smaller than the level of shift due to mistuning. Under this circumstance, both methods are acceptable in predicting natural frequencies, with the exhaustive projection basis providing a better accuracy.

2.3.1.2 Forced Responses

A traveling wave excitation is adopted in this study as the forcing function. It is the most common type of forcing used in analyzing blisk dynamics. A traveling wave excitation is

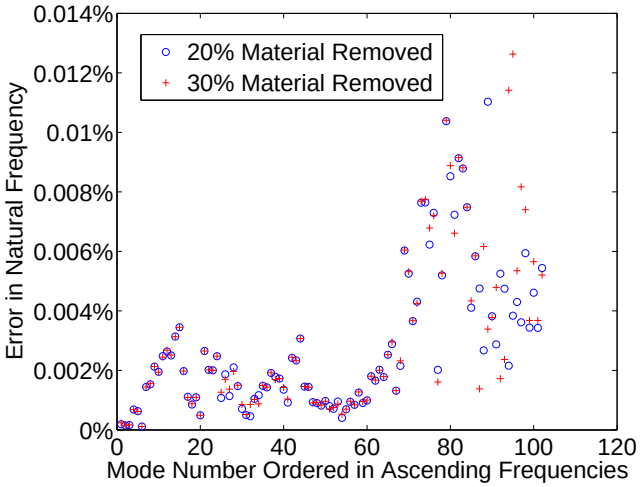

Figure 2.8: Relative errors in frequencies computed by N-PRIME with the exhaustive projection for the UM Validation Blisk with 20% and 30% material removed from a single sector

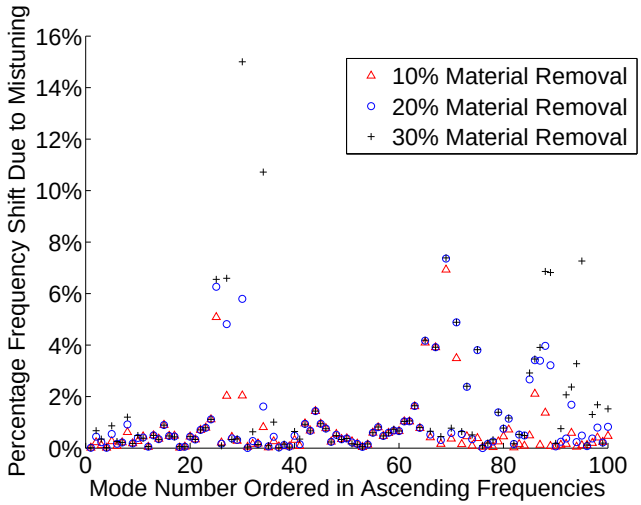

Figure 2.9: Natural frequency shift induced by mistuning for the UM Validation Blisk with 10%, 20% and 30% material removed from a single sector

a function of engine order EO, and can be expressed as

$$\mathbf{f} = \sum_{j=1}^{N} \mathbf{F}_j e^{-i(j-1)\mathrm{EO}\frac{2\pi}{N}}, \tag{2.24}$$

where $\mathbf{F}_j$ is the amplitude vector of the excitation on the j^{th} sector. Responses under excitations of lower engine orders are expected to exhibit disk-dominated motions. In contrast, excitations of higher engine orders often result in blade-dominated responses. For the completeness of this analysis, excitations of both engine order 1 and 12 are included. The traveling wave excitation is applied at the tip of each blade to generate adequately large deformation. Mistuned natural frequencies are chosen as the forcing frequencies. A structural damping ratio of 0.03 is selected.

Consider a blisk that has 30% material removed from one blade, along with small variations in Young's modulus of each blade. This mistuning pattern resembles an extreme case of simultaneous large and small mistuning. Maximum displacements throughout the blisk at each forcing frequency are extracted for validation. Figure 2.10a shows the deviations in ROM-predicted displacements, under a traveling wave excitation of engine order 1, from the responses computed by the full-order FEA. With 5 N/2 modes and 5 CB modes adopted, respectively, N-PRIME provides a comparable accuracy with that provided by C-PRIME, throughout the range of forcing frequencies (0 - 4 kHz). N-PRIME with exhaustive projection provides the best accuracy among all presented projection bases, with a maximum error in displacements that is less than 0.18%. Figure 2.10b shows another case where the same mistuned blisk is forced under a traveling wave excitation of engine order 12. With the 5 N/2 and CB modes employed, respectively, N-PRIME provides a better accuracy than C-PRIME does. Again, N-PRIME with exhaustive projection achieves the best accuracy.

Surface stress distributions are computed for above cases based on the technique of stress modes. Similar to the validation process for displacement responses, the maximum Von-Mises stresses are extracted throughout the surface of all blades at each forcing frequency. Figure 2.11a shows the error in surface stresses for the mistuned blisk under an excitation of engine order 1. In this case, C-PRIME provides a better accuracy than N-PRIME. With exhaustive projection, N-PRIME provides a better accuracy, comparable to that of C-PRIME, with an error in surface stresses of approximately 0.3%. However, under an excitation of engine order 12, with the same number of N/2 and CB modes involved, N-PRIME shows a better accuracy, with a maximum error of 0.5% compared to 0.66% provided by C-PRIME. This error is further reduced to 0.35% when the exhaustive projection is used. Note that the accuracy in predicting surface stresses is limited by the fact that

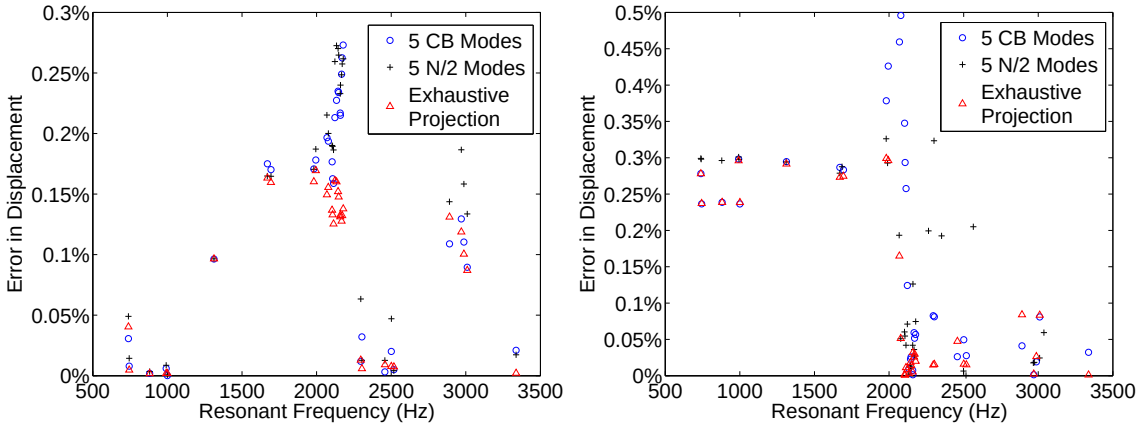

(a) Engine order 1

(b) Engine order 12

Figure 2.10: Error in displacements under traveling wave excitations of engine order 1 and 12, computed by C-PRIME and N-PRIME with different projection bases for the UM Validation Blisk with 30% material removed from a single sector

strain is a spatial derivative of displacements, and the process of numerical differentiation introduces an additional error source in predicting strains and stresses. Thus, the error in predicting surface stresses can only be considered an upper bound error carried by the N-PRIME method. This upper bound does not indicate N-PRIME has a worse accuracy than C-PRIME in computing surface stresses, and vice versa.

2.3.2 Dual-Flow Path Systems

2.3.2.1 Free and Forced Responses

The N-PRIME method is applied in this section to a model of a dual-flow path system that contains 28 sectors. Compared to a conventional bladed disk, the tips of the inner blades are connected to an additional shroud. A second set of blades are attached to the opposite side of the shroud. A sector model of the dual-flow path system is shown in Fig. 2.12. The design of the dual-flow path system adds complexity to its geometry, and a lack of a clear definition of the root of a blade. Consequently, C-PRIME method cannot be applied easily to the dual-flow path system. In contrast, the N-PRIME with exhaustive projection can easily be adopted to analyze the dynamics of the dual-flow path system.

Each sector of the dual-flow path system contains four components that can have distinct small material mistuning. Also, large geometric mistuning may occur at both the inner and outer blade components. In this study, the source of large mistuning includes material being removed from inner blades, outer blades, and simultaneously both these components

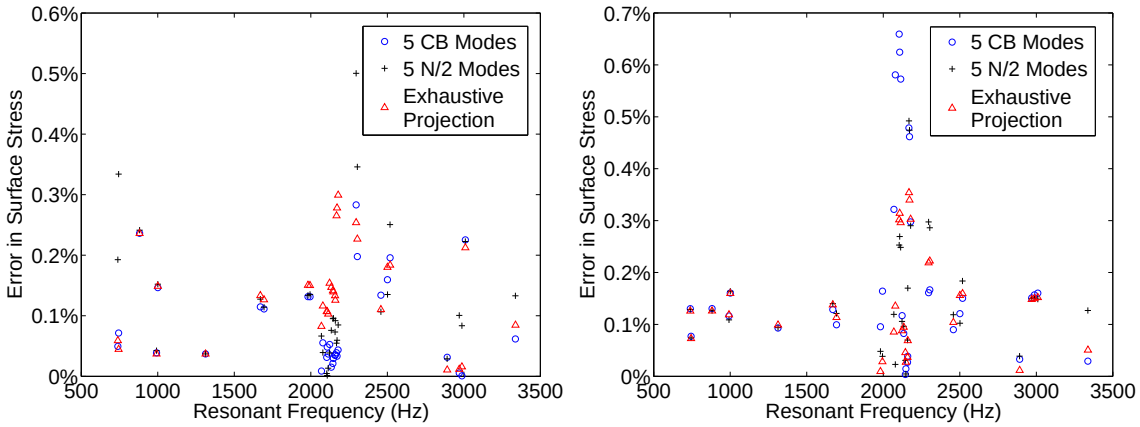

(a) Engine order 1

(b) Engine order 12

Figure 2.11: Error in surface stresses under traveling wave excitations of engine order 1 and 12, computed by C-PRIME and N-PRIME with different projection bases for the UM Validation Blisk with 30% material removed from a single sector

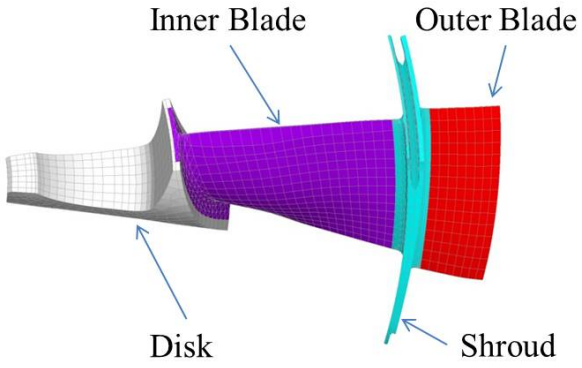

Figure 2.12: A finite element model of a sector of the dual-flow path system

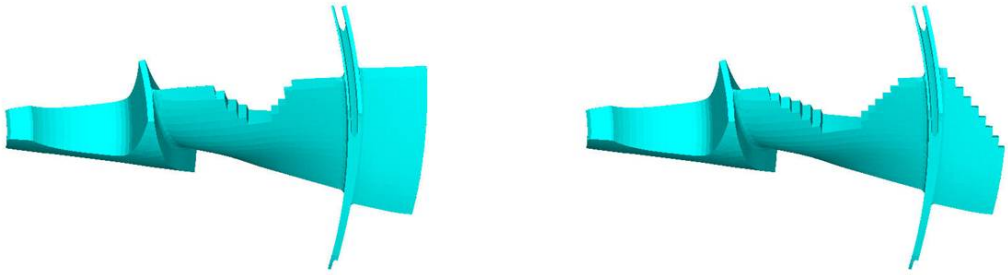

(a) 10% of the inner blade (b) 30% and 20% of outer and inner blades

Figure 2.13: Large mistuning of the dual-flow path system created by removing different amounts of material from different components

of a single sector. Similar to the UM Validation Blisk, small mistuning is applied to the dual-flow path system by varying the Young's modulus of each component. Three distinct sets of small mistuning patterns are applied to all 28 inner blade, 28 outer blade, and 28 shroud components, respectively. Each of the mistuning patterns is chosen randomly and follows a normal distribution with a 0 mean and a 2% standard deviation.

Consider the case where 10% material is removed from the inner blade of one sector, shown in Fig. 2.13a. Figure 2.14 shows the error in displacements and stresses under a traveling wave excitation of engine order 14 applied at the tip of each outer blade. The system is forced at the mistuned natural frequencies. Note that the error carried by most ROM-predicted responses is less 1.5%. However, some responses are associated with a large error ranging from 2% to 4.5%. These responses occur when modes with highly localized motions are excited (Fig. 2.15).

Note that for a conventional blisk, all cyclic modes that are associated with high nodal diameters have mode shapes with blade-dominated motion. In the previous section, 7 mode families for each pristine and rogue sector ranging from 0 to 20 kHz are added to the PRIME basis and are sufficient to capture the localized modes from 0 to 12 kHz. Unlike conventional blisks, cyclic modes of the dual-flow path system that are associated with high nodal diameters can have either inner-blade-dominated or outer-blade-dominated motion (Fig. 2.16). Thus, the PRIME basis for the dual-flow path system must include enough mode families, compared with 7 families used for UM Validation Blisk, in order to adequately contain both types of modes. The current PRIME basis, formed by 232 sector-level cyclic mode shapes, consists of 5 families of outer-blade-dominated modes, and only 2 families of inner-blade-dominated modes for the pristine and each of the rogue sectors.

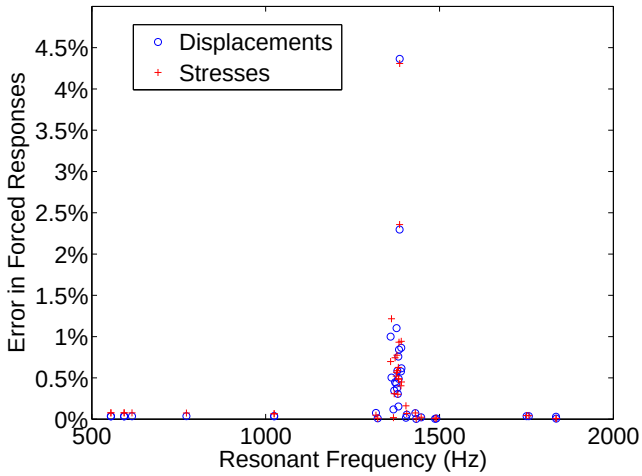

Figure 2.14: Error in forced responses of the dual-flow path system under a traveling wave excitation of engine order 14, in the case where 10% material is removed from the blade component of a sector

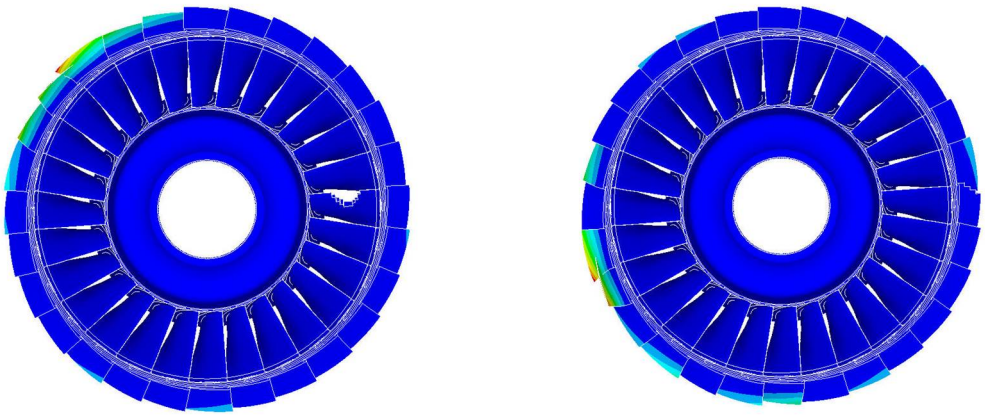

(a) Mode caused by inner blade mistuning

(b) Mode caused by outer blade mistuning

Figure 2.15: Modes with highly localized motion under different types of large mistuning

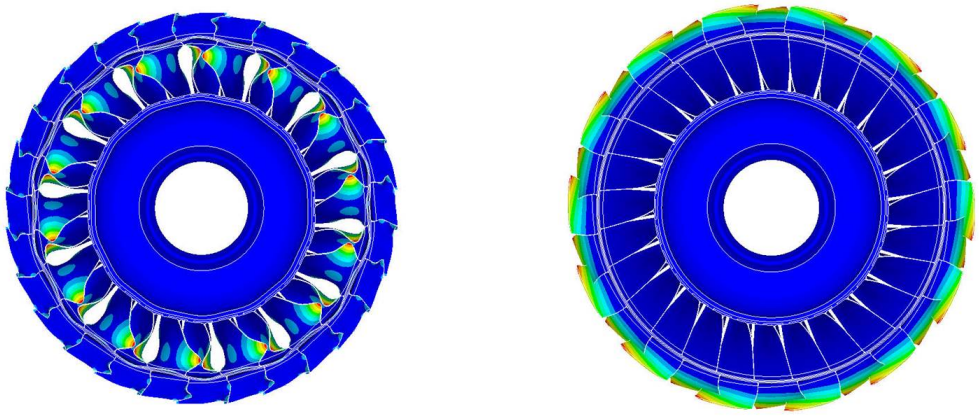

(a) Inner-blade-dominated mode (b) Outer-blade-dominated mode

Figure 2.16: Modes associated with high nodal diameters

Such a basis is insufficient to capture the localized modes. To improve the accuracy of the N-PRIME method, all cyclic modes ranging from 0 to 20 kHz are added to the PRIME basis. Figure 2.17 shows the deviation in ROM-predicted free and forced responses when the larger PRIME basis is used. The error is reduced to a significantly lower level, with a maximum error of 0.53% in displacements and 0.8% in stresses under an excitation of engine order 14 (Fig. 2.17b). Note that such a small error is also observed when an excitation of engine order 1 is applied to the mistuned blisk, where the disk-dominated modes are excited (0.38% in displacements, and 0.9% in stresses), as shown in Fig. 2.17a. Moreover, the maximum error in ROM-predicted mistuned frequencies is 0.0049%, which is negligibly small (Fig. 2.18). Due to the improved accuracy, this larger PRIME basis is used for the rest of the analysis.

Consider an extreme case that involves large mistuning on both the inner and outer blade components. Figure 2.13b shows a damaged sector of a dual-flow path system with 20% and 30% material removed from the inner and outer blade components. Figure 2.20 shows that even in this extreme case, the error carried by the ROM-predicted natural frequencies remains below 0.008%. And the error in forced responses, including both displacements and stresses, has an upper bound of 0.7% (Figs. 2.19a and 2.19b). These results demonstrate that the N-PRIME method is accurate and stable even for severe scenarios of large mistuning.

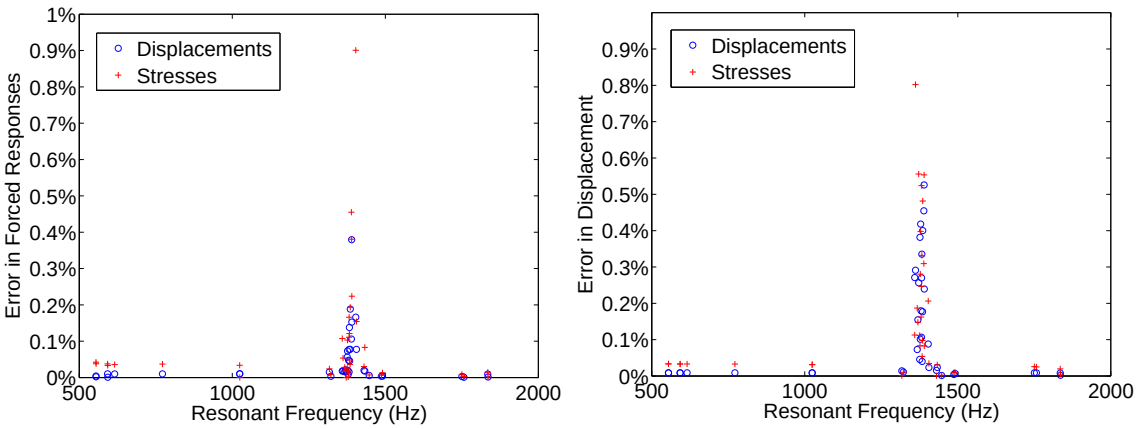

(a) Engine order 1 excitation

(b) Engine order 14 excitation

Figure 2.17: Forced response errors computed with a larger N-PRIME basis, for the dual-flow path system with 10% material removed from the inner blade component of a single sector

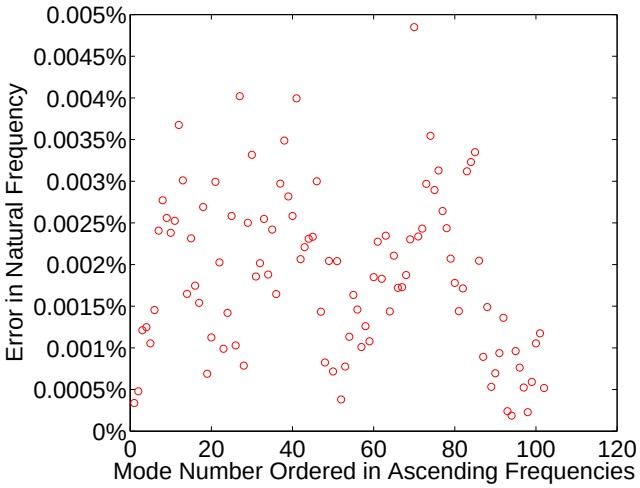

Figure 2.18: Frequency errors computed with a larger N-PRIME basis, for the dual-flow path system with 10% material removed from the inner blade component of a single sector

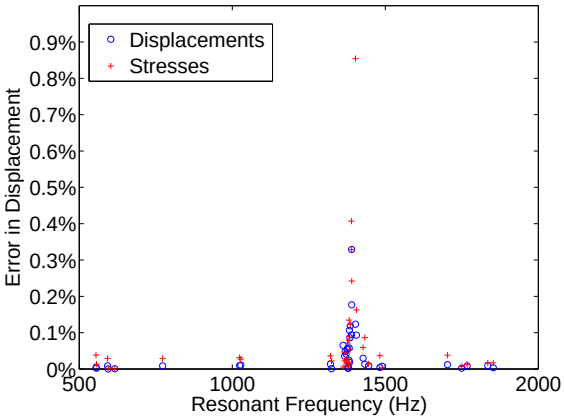

(a) Engine order 1 excitation

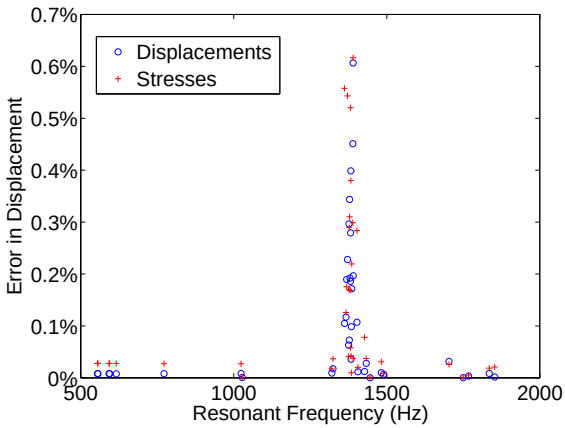

(b) Engine order 14 excitation

Figure 2.19: Forced response errors computed with a larger N-PRIME basis, for the dual-flow path system with 30% material removed from the outer blade and 20% removed from the inner blade of a single sector

Figure 2.20: Frequency errors computed with a larger N-PRIME basis, for the dual-flow path system with 30% material removed from the outer blade and 20% removed from the inner blade of a single sector

2.3.2.2 Statistical Analysis

The previous free and forced response analyses reveal that certain mistuning patterns result in modes with highly localized motions. These modes are often associated with isolated natural frequencies that do not belong to any mode family. However, the correlation between mistuning patterns and occurrences of the isolated modes are uncertain. With fast computations and accuracy provided by the N-PRIME method, it is possible to sample a dual-flow path system over a large amount of mistuning patterns to extract its statistical characteristics, and to reveal the effect of random mistuning on blisk dynamics. In this study, a Monte-Carlo analysis is applied to the dual-flow path system, with 1,000 samples of mistuning patterns included. The mistuning patterns are created as the following:

1. Large mistuning patterns are created by randomly selecting 1 or 2 of the 28 sectors as rogue sectors. Each of the rogue sectors has different volume of material removed from either its inner or outer blade component. In this study, 10 large mistuning patterns are created.

2. Each large mistuning pattern is associated with 100 different small mistuning patterns. Small mistuning patterns are randomly created by varying the Young's modulus of all inner blade, shroud, and outer blade components. These variations follow a normal distribution with a 0 mean and a 2% standard deviation.

Figure 2.21 shows the probability distribution of the ROM-predicted natural frequencies for the 1,000 mistuning patterns. Note that most natural frequencies can be treated as deviations from the natural frequencies of a nominal system (shown by x symbols below the zero probability line). However, there exist groups of mistuned natural frequencies that are not close to any nominal frequencies, including the groups formed near 1,640 Hz and 3,340 Hz. These mistuned natural frequencies correspond to isolated modes that contain highly localized motion, as shown in Fig. 2.22. Since all mistuned natural frequencies up to 5 kHz are included in the Monte Carlo analysis, the occurrence of these isolated modes is relatively low. The probability of the natural frequencies near 3,340 Hz is approximately 0.0048%. However, 99 of the 1,000 mistuning patterns result in such an isolated mode, and therefore such occurrence of isolated modes cannot be ignored in the design process.

An interesting phenomenon is discovered that the motion contained by the isolated mode shapes demonstrated in Fig. 2.22 are localized on the rogue sectors. This phenomenon indicates that the cyclic modes of the rogue sectors have a dominating participation in forming such isolated mode shapes. Thus, in this case, one possible source of the emerging groups of mistuned natural frequencies near 1,640 Hz and 3,340 Hz are the

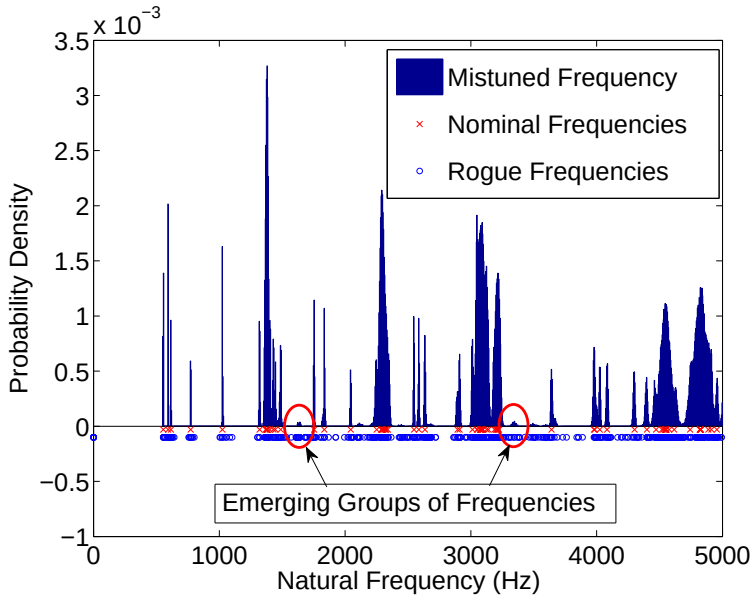

Figure 2.21: Probability distribution of mistuned natural frequencies of the dual-flow path system with random mistuning

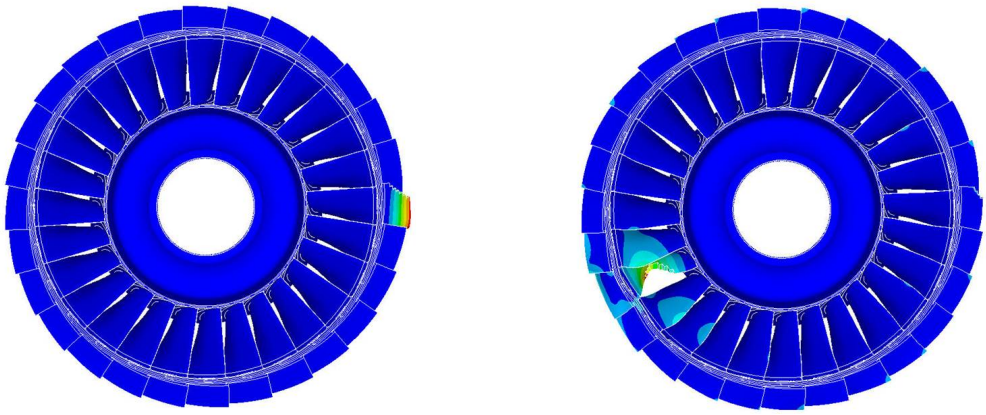

(a) Isolated mode shape around 1,640 Hz

(b) Isolated mode shape around 3,340 Hz

Figure 2.22: Typical mode shapes for the two clusters of isolated modes around 1,640 and 3,340 Hz

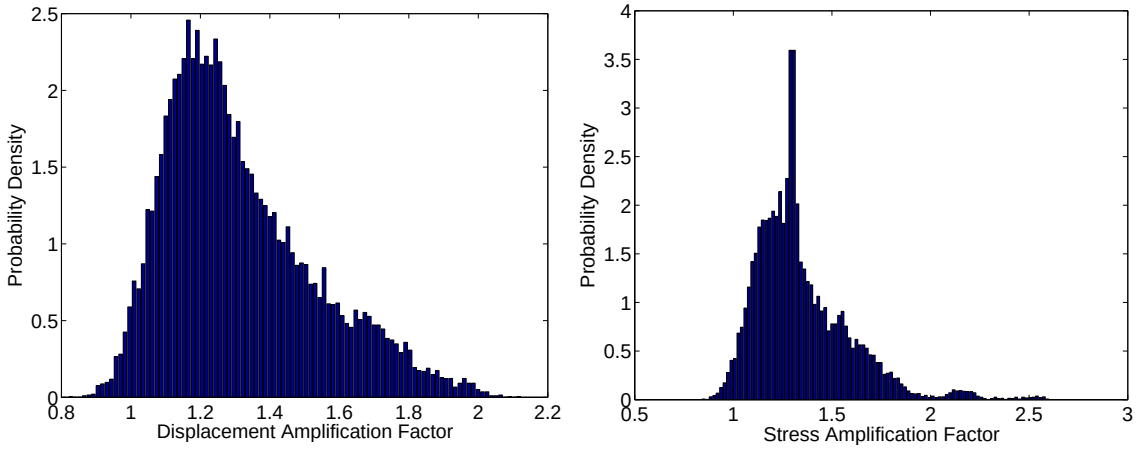

(a) Amplification factors of displacements

(b) Amplification factors of stresses

Figure 2.23: Probability distributions of amplification factors of forced responses for the dual-flow path system with random mistuning

frequencies associated with cyclic rogue modes within the same frequency range (shown by circles below the zero probability line in Fig. 2.21). However, this is an incomplete observation since within the frequency range between 3,840 Hz and 3,890 Hz, there exist frequencies of cyclic rogue modes. However, no mistuned natural frequencies are found in this frequency range.

Figure 2.23 shows the probability distributions of displacement and stress amplification factors under traveling wave excitations. The forced response computations are performed for a) each of the 1,000 mistuning patterns at the resulting mistuned natural frequencies up to 4 kHz, and b) for all engine orders from 0 to 14. In Fig. 2.23a, the mean value of the displacement amplification factors is 1.3131, and the 95 percentile amplification factors is 1.7413, which corresponds to an increase in displacement amplitudes of 74.13%. Also, the mean stress amplification factor is 1.3436, and the 95 percentile stress amplification factors is 1.7800, which corresponds to an increase in Von-Mises stresses of 78.00% (Fig. 2.23b). Note that both the mean and 95 percentile amplification factors of stresses are slightly higher than that of displacements.

Conventionally, the amplification factors extracted from displacement responses are used to estimate the maximum stress as

$$\max_{\omega}(\sigma^{\mathrm{m}}) = \max_{\omega}(\sigma^{0})\mathrm{AF}_{\mathrm{x}}. \tag{2.25}$$

The results provided by the statistical analysis suggests that Eqn. (2.25) is valid in estimating the mean value of stress amplification, and the 95 percentile of the maximum

stress amplification. However, Fig. 2.23b reveals that the stress amplification factors are more concentrated in a certain range, such as the peak located at 1.30, and the group of amplification factors near 2.20. Thus, Eqn. (2.25) cannot be applied to generate an accurate full profile of stress amplifications.

Previous work by Bladh et al. [11] suggests that the probability density functions (pdf) of the amplification factors follow a modified Weibull pdf, which is expressed as

$$P(AF) = \frac{a}{b}\left(\frac{-AF+c}{b}\right)^{a-1} e^{-\left(\frac{-AF+c}{b}\right)^{a}}, \tag{2.26}$$

where P is the probability density, a function of the amplification factor AF. a, b, and c are the parameters of the modified Weibull distribution, which differs slightly from the conventional 3-parameter Weibull distribution by a negative sign before the variable. Bladh's analysis involves cases with only small mistuning. In order to verify whether such a pdf is applicable to simultaneous large and small mistuning, a statistical analysis is performed with a single known large mistuning pattern, associated with 1,000 small random mistuning patterns. These mistuning patterns are created in the same way as the previous analysis. The resulted probability distributions of amplification factors are shown in Fig. 2.24, along with the Weibull pdf with proper fitting parameters.

As shown by Fig. 2.24a, although most displacement amplification factors follow the pdf, outliers form a second peak located around 1.90. Similarly, Fig. 2.24b shows that 3 groups of amplification factors, located around 1.51, 1.64 and 2.55, do not follow the Weibull pdf. These outliers correspond to the forced responses where the isolated modes are excited. These modes can be excited under traveling wave excitations of multiple engine orders, and thus increase the occurrence of amplification factors within certain ranges. Also, from a mathematical perspective, the Weibull distribution should not be expected to capture the amplification factors when large mistuning is involved, as the assumption of independently and identically distributed (IID) random variables is violated. Since the results that Bladh et al. presents only involves cases with small mistuning, the occurrence of the isolated modes is very low, and the assumption of IID variables can still hold. However, in the presence of large mistuning, the Weibull pdf may fail to estimate the amplification of forced responses, due to the higher occurrence of the isolated modes.

2.4 Conclusions

A new reduced-order modeling technique, capable of capturing the dynamics of bladed disks with simultaneous large and small mistuning, was presented in this paper. This tech-

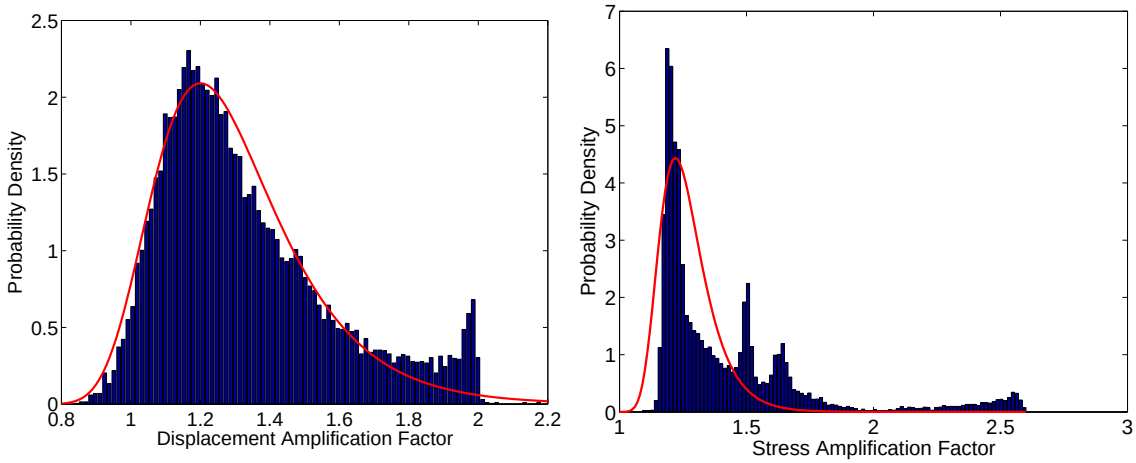

(a) Amplification factors of displacements

(b) Amplification factors of stresses

Figure 2.24: Weibull-fitted probability density distributions of amplification factors

nique, referred to as N-PRIME, utilizes the concepts of pristine, rogue, and interface modal expansion, and nodal energy weighted transformation. The N-PRIME method has the following attractive features.

1. Compared to the CMM method adopted by Madden et al. [7], N-PRIME does not require a clear definition of the root of a blade because N-PRIME uses cyclic modes rather than CB modes as the projection basis to model small mistuning. Therefore, N-PRIME is applicable to complex structures such as dual-flow path systems.

2. Unlike CMM, which restricts small mistuning to exist only on the blade components, N-PRIME allows all components of a sector to have distinct levels of small mistuning. Thus, it is possible for users to flexibly define regions or components to be mistuned.

3. Mistuning often introduces isolated modes that have highly localized motions. N-PRIME is capable of capturing these modes with very good accuracy.

4. N-PRIME has NEWT strategically integrated under the frame of the PRIME method. A PRIME basis is formed for a large mistuning pattern and is re-constructed only when the large mistuning changes. The small mistuning component is projected on to a small subset of cyclic modes, and modeled with low computational cost. This integration allows a largely mistuned blisk to be fast sampled over multiple small mistuning patterns.

5. N-PRIME requires only sector-level mode shapes to form the PRIME basis. Also, a subset of the cyclic modes is used for small mistuning projection. Thus, all computations performed by N-PRIME are on a sector level, and require low computational effort.

The results presented demonstrate that N-PRIME has very good accuracy in predicting free and forced responses of mistuned blisks, including conventional blisks, and more complex structures such as dual-flow path systems. Moreover, the efficiency of N-PRIME enables it to be one of the first available methods that can perform statistical analyses to study the effects of random large and small mistuning on blisk dynamics.

CHAPTER 3

Nonlinear Dynamics of Mistuned Bladed Disks with Ring Dampers

3.1 Introduction

To reduce forced response amplitudes when subject to high level of dynamic loadings, various dry friction dampers are designed for blisk systems, including the underplatform wedge damper [22, 32, 33, 37–39, 51, 52], frictional shroud contact [35, 40, 41, 47, 48], and ring dampers [56–59]. Ring dampers have gained increasing popularity and are the focus of this study. These ring-shaped damping sources are located in the disk, underneath the blades, and are held in contact with the blisk by centrifugal loading. Energy is dissipated by nonlinear friction forces when relative motions between the ring damper and the blisk take place.

To investigate the dynamic responses of blisk-damper systems in the presence of the nonlinear frictional contacts, conventional methods based on numerical time integration are not suitable since they are computationally expensive. Limited amount of effort has been done to develop efficient ROMs for blisks in contact with ring dampers. This paper presents a reduced-order modeling technique to efficiently capture the nonlinear dynamic responses of the blisk-damper systems. CB-CMS serves as the first model reduction step. A novel mode basis that mimics the contact behavior under sliding and sticking conditions is developed to further reduce the CB-CMS model while maintaining its accuracy. The resulting reduced nonlinear equations of motion are solved by a HFT method. In the HFT method, the contact status and friction forces are determined in the time domain by a three-dimensional contact model at each contact point, whereas the reduced equations of motion are solved in the frequency domain according to a harmonic balance formulation. Moreover, to investigate the effects of blade mistuning, which can lead to drastic increase of forced responses, an extension of the ROMs is developed based on component mode mistuning.

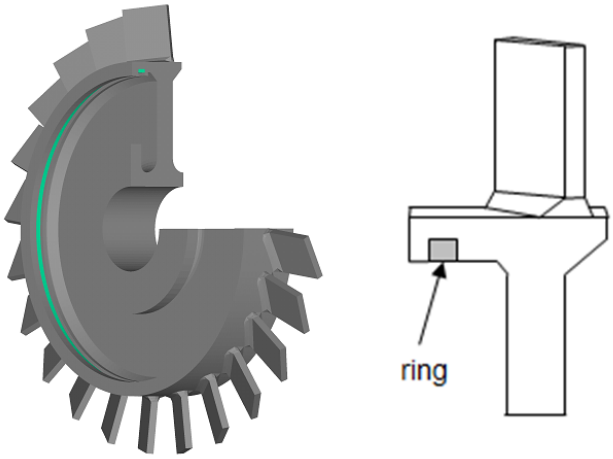

Figure 3.1: A typical blisk-damper system (UM Validation Blisk with a ring damper)

The reduced-order modeling technique developed in this study is applied to the UM Validation Blisk model, in contact with a frictional ring damper, as shown in Fig. 3.1. ROM-predicted forced responses are retrieved and validated for both tuned and mistuned models. The computational effort required by the developed ROM is minimal, and that enables statistical analyses, which reveal the influence of random mistuning on the effectiveness of energy dissipation by frictional ring dampers. A statistical analysis is presented in this paper.

3.2 Methodology

3.2.1 Frequency-Domain Formulation of the Equations of Motion

Consider the following equations of motion of a general blisk-damper system

$$\mathbf{M}\ddot{\mathbf{x}}(t) + \beta\mathbf{K}\dot{\mathbf{x}}(t) + \mathbf{K}\mathbf{x}(t) = \mathbf{F}_e(t) + \mathbf{F}_{nl}(t), \tag{3.1}$$

where $\mathbf{M}$ and $\mathbf{K}$ are the mass and stiffness matrices of the full-order blisk-damper system, β is the stiffness-proportional damping coefficient, $\mathbf{x}(t)$ is the displacement vector, $\mathbf{F}_e(t)$ is the vector of external periodic forcing, and $\mathbf{F}_{nl}(t)$ is the vector of nonlinear contact forces that are functions of displacements and velocities at the contact DOFs.

It is assumed that under periodic excitations, the steady-state responses of the nonlinear blisk-damper system remain periodic. Thus, each of the variables in Eqn. (3.1), including the displacement $\mathbf{x}(t)$, the external forcing $\mathbf{F}_e(t)$, and the nonlinear force $\mathbf{F}_{nl}(t)$, can be

approximated by a truncated sum of harmonic terms, written as

$$\begin{aligned}
\mathbf{x}(t) &= \mathbf{x}^{(0)} + \mathrm{Re}\left(\sum_{n=1}^{N_H} \mathbf{x}^{(n)} e^{in\omega t}\right), \\
\mathbf{F}_e(t) &= \mathbf{F}_e^{(0)} + \mathrm{Re}\left(\sum_{n=1}^{N_H} \mathbf{F}_e^{(n)} e^{in\omega t}\right), \\
\mathbf{F}_{nl}(t) &= \mathbf{F}_{nl}^{(0)} + \mathrm{Re}\left(\sum_{n=1}^{N_H} \mathbf{F}_{nl}^{(n)} e^{in\omega t}\right),
\end{aligned} \tag{3.2}$$

where N_H is the number of harmonics used in the approximation, and ω is the frequency of the external excitation $\mathbf{F}_e(t)$. By substituting Eqn. (3.2) into Eqn. (3.1), a set of N_H nonlinear complex algebraic equations are obtained as

$$\mathbf{D}^{(n)}\mathbf{x}^{(n)} = \mathbf{F}_e^{(n)} + \mathbf{F}_{nl}^{(n)}, \tag{3.3}$$

where $\mathbf{x}^{(n)}$ is a vector containing the amplitudes of motion of the n^{th} harmonic at all DOFs, and $\mathbf{D}^{(n)}$ is the n^{th} order dynamic stiffness matrix of the blisk-damper system ($n = 1, 2, \cdots, N_H$), and is expressed as

$$\mathbf{D}^{(n)} = -(n\omega)^2\mathbf{M} + (1 + i\beta n\omega)\mathbf{K}. \tag{3.4}$$

3.2.2 Contact Model

The frictional contact between the blisk and the ring damper is modeled by contact node pairs that are evenly distributed across two mating contact surfaces. The 3D relative displacements between each contact node pair are expressed in the contact local coordinates, and decomposed into an out-of-plane normal and two perpendicular in-plane tangential components. A fully coupled 3D contact model is available in Ref. [30]. However, the focus of this study is to develop reduced-order modeling techniques for blisk-damper systems. Thus, a simplified model is adopted to accelerate the computations. This simplified model is based on the assumption that the two tangential components of relative motions, as well as the resulted tangential contact forces, are independent of each other. Thus, contact dynamics along each contact tangential direction can be modeled by a 1D macro-slip contact model with normal load variations [26]. This assumption has been extensively adopted and validated in many studies of frictional contacts [51, 52, 65]; it is particularly adequate for ring dampers because there is a strongly dominant direction of relative motion at the contact, namely, the tangential direction along the ring.

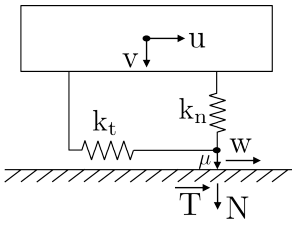

Figure 3.2: Macro-slip model showing tangential and normal coordinates and stiffness

The 1D macro-slip contact model with normal load variations is shown in Fig. 3.2. The parameters of the contact model include the tangential contact stiffness k_t, the normal contact stiffness k_n, and the friction coefficient μ. Relative displacements in the tangential and normal directions are denoted by $u(t)$ and $v(t)$, respectively. The amount of slip motion is expressed as $w(t)$. The normal force between the contact surfaces is expressed as

$$N(t) = \max(N_0 + k_n v(t), 0), \tag{3.5}$$

where N_0 is the initial normal force due to static pre-stress. Along the tangential direction, the friction force is computed according to the Coulomb's law of friction as follows

$$T(t) = \begin{cases} k_t(u(t) - w(t)) & \text{sticking} \\ sign(\dot{w}(t))\mu N(t) & \text{sliding} \\ 0 & \text{separation} \end{cases} \tag{3.6}$$

Detailed transition criteria for the contact status (sticking, sliding, or separation) can be found in Ref. [30]. Note that the friction forces applied on each contact node are computed in the contact local coordinates. Due to the circular geometry of the ring damper, it is convenient to align one of the local in-plane directions with the tangential direction of the global cylindrical coordinate system.

3.2.3 Reduced-Order Modeling

Full-order finite element models of industrial blisk-damper systems in general contain many DOFs. Thus, solving Eqn. (3.3) in the frequency domain remains a formidable task. To reduce the computational effort required to solve the nonlinear algebraic equations, successive model reduction techniques are developed and applied in this study.

3.2.3.1 Craig-Bampton Component Mode Synthesis

The nonlinearity possessed by a general blisk-damper system is localized at contact DOFs. Thus, it is possible to categorize the DOFs of the system into nonlinear DOFs, where nonlinear friction forces are applied upon, and all other linear DOFs. Since the set of nonlinear DOFs is small in size, applying a classical CB-CMS method to the system can result in significant model reduction because most linear DOFs can be reduced to much fewer modal coordinates of the normal modes of a blisk-damper system with fixed CB-CMS interfaces, while leaving the nonlinear DOFs intact.

Note that not all linear DOFs are substituted by modal coordinates. Some linear DOFs of particular importance to the forced response analysis can be retained. Thus, the DOFs of the blisk-damper system can be re-arranged as

$$\mathbf{x}^{(n)} = [\mathbf{x}_{nl}^{(n)}, \mathbf{x}_{l,r}^{(n)}, \mathbf{x}_{u}^{(n)}]^T = [\mathbf{x}_{a}^{(n)}, \mathbf{x}_{u}^{(n)}]^T, \tag{3.7}$$

where $\mathbf{x}_{nl}^{(n)}$ represents the n^{th} harmonic of the amplitudes of motion of the nonlinear DOFs, $\mathbf{x}_{l,r}^{(n)}$ contains the n^{th} harmonic of the amplitudes of motion of the linear retained DOFs, and $\mathbf{x}_{u}^{(n)}$ contains the n^{th} harmonic of the amplitudes of motion of the slave/unretained linear DOFs. Both $\mathbf{x}_{nl}^{(n)}$ and $\mathbf{x}_{l,r}^{(n)}$ are retained after the CB-CMS reduction process, and thus they are grouped into a vector $\mathbf{x}_{a}^{(n)}$ (active DOFs). Eqn. (3.3) is subsequently partitioned as

$$\begin{bmatrix} \mathbf{D}_{aa}^{(n)} & \mathbf{D}_{au}^{(n)} \\ \mathbf{D}_{ua}^{(n)} & \mathbf{D}_{uu}^{(n)} \end{bmatrix} \begin{bmatrix} \mathbf{x}_{a}^{(n)} \\ \mathbf{x}_{u}^{(n)} \end{bmatrix} = \begin{bmatrix} \mathbf{F}_{e,a}^{(n)} \\ \mathbf{F}_{e,u}^{(n)} \end{bmatrix} + \begin{bmatrix} \mathbf{F}_{nl,a}^{(n)} \\ \mathbf{F}_{nl,u}^{(n)} \end{bmatrix}. \tag{3.8}$$

CB-CMS is a well-established reduced-order modeling technique, and its detailed formulation can be found in Ref. [49]. Using CB-CMS, Eqn. (3.3) is transformed into CB-CMS coordinates for each harmonic n based on the following transformation

$$\mathbf{x}_{CMS}^{(n)} = \begin{bmatrix} \mathbf{x}_{a}^{(n)} \\ \mathbf{q}_{CMS}^{(n)} \end{bmatrix} = \mathbf{T}_{CMS} \begin{bmatrix} \mathbf{x}_{a}^{(n)} \\ \mathbf{x}_{u}^{(n)} \end{bmatrix} = \begin{bmatrix} \mathbf{I} & \mathbf{0} \\ \mathbf{\Psi} & \mathbf{\Phi} \end{bmatrix} \begin{bmatrix} \mathbf{x}_{a}^{(n)} \\ \mathbf{x}_{u}^{(n)} \end{bmatrix}, \tag{3.9}$$

where $\mathbf{T}_{CMS}$ is the CB-CMS transformation matrix. $\mathbf{\Psi}$ contains the constraint mode shapes for each active DOF, and $\mathbf{\Phi}$ contains the system normal mode shapes under CB-CMS fixed-interface boundary conditions. $\mathbf{x}_{u}^{(n)}$ has many physical linear DOFs which are replaced by a few modal coordinates $\mathbf{q}_{CMS}^{(n)}$. The resulting equations of motion can be written as

$$\mathbf{D}_{CMS}^{(n)} \mathbf{x}_{CMS}^{(n)} = \mathbf{F}_{e,CMS}^{(n)} + \mathbf{F}_{nl,CMS}^{(n)}, \tag{3.10}$$

where the subscript CMS indicates that the corresponding term is expressed in the CB-CMS coordinates.

3.2.3.2 Extending CB-CMS with Component Mode Mistuning (CB-CMS-CMM)

One of the objectives of this study is to analyze the forced responses of blisk-damper systems with random blade mistuning. The process of repetitively applying the CB-CMS method to a large number of full-order blisk-damper systems, where each of the systems is associated with a distinct mistuning pattern, can be computationally expensive. Methods to speed up the process have been proposed and used especially for geometric mistuning [66]. In general, it is preferable to perform the CB-CMS model condensation to a tuned system, and construct the mistuning component of the dynamic stiffness matrix, without any involvement of the full-order finite element model, directly in the CB-CMS coordinates. Thus, a reduced-order modeling technique is proposed by extending CB-CMS with the technique of CMM, resulting in a generalized CB-CMS method that can efficiently model mistuned systems. This method is named CB-CMS-CMM. The first step of CB-CMS-CMM is to apply CB-CMS on a tuned system to obtain the tuned dynamic stiffness matrix in the CB-CMS coordinates, $\mathbf{D}^{0}{}^{(n)}_{CMS}$, and the CB-CMS transformation matrix $\mathbf{T}^{0}_{CMS}$. The superscript 0 indicates that the corresponding term is for a tuned system.

Consider a blisk-damper system with blade mistuning. Assume mistuning is small and can be represented as variations in the stiffness of each blade. The dynamic stiffness matrix expressed in Eqn. (3.4) becomes

$$\mathbf{D}^{(n)} = -(n\omega)^2\mathbf{M}^0 + (1 + i\beta n\omega)(\mathbf{K}^0 + \mathbf{K}^\delta), \tag{3.11}$$

where $\mathbf{M}^0$ and $\mathbf{K}^0$ are the mass and stiffness matrices of the tuned system, and $\mathbf{K}^\delta$ is the mistuning component of the stiffness matrix. If CB-CMS is applied to the mistuned system, the mistuned dynamic stiffness matrix in the CB-CMS coordinates can be expressed as

$$\begin{aligned}
\mathbf{D}^{(n)}_{CMS} &= \mathbf{T}^T_{CMS}\mathbf{D}^{(n)}\mathbf{T}_{CMS} \\
&= \mathbf{T}^T_{CMS}(-(n\omega)^2\mathbf{M}^0 + (1 + i\beta n\omega)(\mathbf{K}^0 + \mathbf{K}^\delta))\mathbf{T}_{CMS} \\
&= \mathbf{T}^T_{CMS}\mathbf{D}^{0}{}^{(n)}\mathbf{T}_{CMS} + (1 + i\beta n\omega)\mathbf{T}^T_{CMS}\mathbf{K}^\delta\mathbf{T}_{CMS}.
\end{aligned} \tag{3.12}$$

The mistuned CB-CMS transformation matrix $\mathbf{T}_{CMS}$ contains two sets of mode shapes, including the system normal mode shapes $\mathbf{\Phi}$, and the constraint mode shapes $\mathbf{\Psi}$. As suggested by Yang et al. [14], system normal mode shapes of a blisk with small mistuning and with closely spaced natural frequencies can be estimated as a linear combination of the nor-

mal mode shapes of a tuned system, within the same frequency range. Moreover, constraint modes are computed by applying a unit displacement at each of the active DOFs. All the active DOFs in the case of ring damper surfaces are located on the disk and on the ring damper, and are remote from the mistuning components (i.e., the blades). Therefore, the difference between the constraint mode shapes of a tuned and a mistuned systems is negligible. Thus, the CB-CMS mode basis of a mistuned system is approximated by a linear combination of the mode basis of a tuned system. Based on this assumption, Eqn. (3.12) can be re-written as

$$\mathbf{D}^{(n)}_{CMS} \approx \mathbf{T}^{0^T}_{CMS}\mathbf{D}^{0^{(n)}}\mathbf{T}^{0}_{CMS} + (1+i\beta n\omega)\mathbf{T}^{0^T}_{CMS}\mathbf{K}^{\delta}\mathbf{T}^{0}_{CMS}. \tag{3.13}$$

Note that $\mathbf{T}^{0^T}_{CMS}\mathbf{D}^{0^{(n)}}\mathbf{T}^{0}_{CMS}$ is the dynamic stiffness matrix $\mathbf{D}^{0^{(n)}}_{CMS}$ of the tuned system in CB-CMS coordinates. Thus, Eqn. (3.13) becomes

$$\mathbf{D}^{(n)}_{CMS} \approx \mathbf{D}^{0^{(n)}}_{CMS} + (1+i\beta n\omega)\mathbf{T}^{0^T}_{CMS}\mathbf{K}^{\delta}\mathbf{T}^{0}_{CMS}. \tag{3.14}$$

Matrix $\mathbf{D}^{\delta^{(n)}}_{CMS} = \mathbf{T}^{0^T}_{CMS}(1+i\beta n\omega)\mathbf{K}^{\delta}\mathbf{T}^{0}_{CMS}$ represents the mistuning component of the dynamic stiffness matrix in CB-CMS coordinates. For cases where mistuning exists only on the blade components of the system, only the blade DOFs of the mistuning stiffness matrix $\mathbf{K}^{\delta}$ contain non-zero entries. Thus, $\mathbf{D}^{\delta^{(n)}}_{CMS}$ can be expanded as

$$\begin{aligned}
\mathbf{D}^{\delta^{(n)}}_{CMS} &= (1+i\beta n\omega)\begin{bmatrix}\mathbf{I} & \mathbf{0}\\ \mathbf{\Psi} & \mathbf{\Phi}\end{bmatrix}^{0^T}\mathbf{K}^{\delta}\begin{bmatrix}\mathbf{I} & \mathbf{0}\\ \mathbf{\Psi} & \mathbf{\Phi}\end{bmatrix}^{0} \\
&= (1+i\beta n\omega)\Bigg(\sum_{i}^{N}\mathbf{\Psi}^{0^T}_{i,B}\mathbf{K}^{\delta}_{i,B}\mathbf{\Psi}^{0}_{i,B} + \sum_{i}^{N}\mathbf{\Psi}^{0^T}_{i,B}\mathbf{K}^{\delta}_{i,B}\mathbf{\Phi}^{0}_{i,B} + \ldots \\
&\ldots + \sum_{i}^{N}\mathbf{\Phi}^{0^T}_{i,B}\mathbf{K}^{\delta}_{i,B}\mathbf{\Psi}^{0}_{i,B} + \sum_{i}^{N}\mathbf{\Phi}^{0^T}_{i,B}\mathbf{K}^{\delta}_{i,B}\mathbf{\Phi}^{0}_{i,B}\Bigg),
\end{aligned} \tag{3.15}$$

where N is the number of blades, and $\mathbf{\Psi}^{0}_{i,B}$, $\mathbf{\Phi}^{0}_{i,B}$, and $\mathbf{K}^{\delta}_{i,B}$ represent the portion of constraint modes, system normal modes and mistuning stiffness matrix that contain only the DOFs of the i^{th} blade, respectively. To further simplify Eqn. (3.15), two assumptions are made and discussed next.

The first assumption is that the blade DOFs of the tuned system normal modes under CB-CMS boundary conditions can be expressed as a linear combination of the cantilever blade (CB) modes of a tuned sector [1, 2]. CB modes are the normal modes of the blade component computed with the root of the blade held fixed. This assumption has been used

in many studies and is at the heart of CMM [1, 2, 7]. Thus, no DOFs retained by the CB-CMS condensation exist on the blade components. With this assumption, the projection of mistuning components onto the system normal modes can be simplified as

$$\sum_{i}^{N} {\boldsymbol{\Phi}^{0}}^{T}_{i,B} \mathbf{K}^{\delta}_{i,B} \boldsymbol{\Phi}^{0}_{i,B} \approx \sum_{i}^{N} \mathbf{q}^{T}_{i,CB} (\boldsymbol{\Phi}^{T}_{CB} \mathbf{K}^{\delta}_{i,B} \boldsymbol{\Phi}_{CB}) \mathbf{q}_{i,CB}, \tag{3.16}$$

where $\boldsymbol{\Phi}_{CB}$ contains the CB mode shapes of a tuned sector. $\mathbf{q}_{i,CB}$ represents the participation factors of each CB mode contributing to the tuned system normal modes. The benefits of CMM are highlighted by Eqn. (3.16) which shows that the mistuning is projected onto tuned CB modes at a blade level.

The second assumption is that the tuned and mistuned static constraint modes are equal in their blade portions. Constraint modes are computed by applying a unit displacement on each of the active DOFs, and all active DOFs are located on the disk and the ring damper. Since the disk is typically much stiffer than the blade, and since the ring damper is decoupled from the blisk during the CB-CMS model reduction, the blade motion resulting from a unit displacement on any of the active DOFs is negligible. Thus, in Eqn. 3.15, all terms that involve projections of mistuning components onto the constraint mode shapes can be neglected (i.e., $\sum_{i}^{N} {\boldsymbol{\Psi}^{0}}^{T}_{i,B} \mathbf{K}^{\delta}_{i,B} \boldsymbol{\Psi}^{0}_{i,B}$, $\sum_{i}^{N} {\boldsymbol{\Psi}^{0}}^{T}_{i,B} \mathbf{K}^{\delta}_{i,B} \boldsymbol{\Phi}^{0}_{i,B}$, and $\sum_{i}^{N} {\boldsymbol{\Phi}^{0}}^{T}_{i,B} \mathbf{K}^{\delta}_{i,B} \boldsymbol{\Psi}^{0}_{i,B}$).

Using these two assumptions, Eqn. (3.15) can be simplified to

$$\begin{aligned} \mathbf{D}^{\delta(n)}_{CMS} &\approx (1 + i\beta n\omega) \sum_{i}^{N} \mathbf{q}^{T}_{i,CB} \boldsymbol{\Phi}^{T}_{CB} \mathbf{K}^{\delta}_{i,B} \boldsymbol{\Phi}_{CB} \mathbf{q}_{i,CB} \\ &= (1 + i\beta n\omega) \sum_{i}^{N} \mathbf{q}^{T}_{i,CB} \boldsymbol{\Lambda}_{i,CB} \mathbf{q}_{i,CB} \end{aligned} \tag{3.17}$$

where in general, $\boldsymbol{\Lambda}_{i,CB} = \boldsymbol{\Phi}^{T}_{CB} \mathbf{K}^{\delta}_{i,B} \boldsymbol{\Phi}_{CB}$ is a diagonally-dominated matrix. In classical CMM [1, 2] its off-diagonal terms are neglected. Based on Eqn. (3.17), an approximation of the mistuning component of the dynamic stiffness matrix can be directly constructed in the CB-CMS coordinates. Note that $\mathbf{q}_{i,CB}$ represents the relation between the tuned CB modes and the tuned system normal modes. Since only the tuned system is involved, the participation factors can be pre-calculated in a single calculation. Since $\boldsymbol{\Lambda}_{i,CB}$ can be simplified to a diagonal matrix, minimal computational effort is required by the method of CB-CMS-CMM to construct the mistuning component of dynamics stiffness.

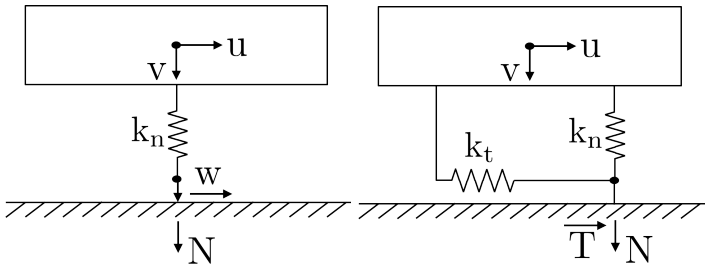

(a) Sliding condition (b) Sticking condition

Figure 3.3: Equivalent contact models of a node pair under two limiting contact statuses

3.2.3.3 Stick-Slip Modal Transformation

The size of the ROMs resulting from CB-CMS model reduction is usually several orders of magnitude smaller than that of the full-order finite element models of the blisk-damper systems. However, fully refined contact surfaces can possess numerous nonlinear DOFs, and solving Eqn. (3.10) can still be a computationally difficult task. Thus, a novel reduced-order modeling technique is proposed in this section to further reduce the size of the CB-CMS model.

Consider a contact in the sliding condition. In this case, the tangential contact force is constant, and hence, the tangential contact stiffness has no effect. An equivalent contact model is constructed by removing the tangential stiffness from the 1D macro-slip model, as shown in Fig. 3.3a. Now consider the opposite case where a contact is in the sticking condition. This contact can be modeled as shown in Fig. 3.3b, where the slider is bonded to the contact surface so that no sliding motion occurs. Local contact stiffness matrices can be defined for the two cases as

$$\mathbf{k}_{sl,l} = \begin{bmatrix} 0 & 0 & 0 \\ 0 & 0 & 0 \\ 0 & 0 & k_n \end{bmatrix}, \qquad \mathbf{k}_{st,l} = \begin{bmatrix} k_t & 0 & 0 \\ 0 & k_t & 0 \\ 0 & 0 & k_n \end{bmatrix}, \tag{3.18}$$

where the subscript l denotes local coordinates.

Using a rotation matrix $\mathbf{R}$ defined for each contact node pair, the contact stiffness matrices can be transformed into global coordinates as

$$\mathbf{k}_{sl,g} = \mathbf{R}^T \mathbf{k}_{sl,l} \mathbf{R}, \qquad \mathbf{k}_{st,g} = \mathbf{R}^T \mathbf{k}_{st,l} \mathbf{R}. \tag{3.19}$$

Next, we consider two extreme cases where all node pairs on the frictionless contact surfaces remain in contact, and are in one of the following conditions:

1. Global sliding condition: the entire contact surfaces slide.

2. Global sticking condition: the entire contact surfaces are stuck.

For the global sliding and sticking conditions, global contact stiffness matrices $\mathbf{K}_{sl}$ and $\mathbf{K}_{st}$ can be assembled from $\mathbf{k}_{sl,g}$ and $\mathbf{k}_{st,g}$, respectively. Note that since all contact DOFs are retained by CB-CMS condensation, the global stiffness matrices can be constructed directly in the CB-CMS coordinates, denoted as $\mathbf{K}_{sl,CMS}$ and $\mathbf{K}_{st,CMS}$. Also, note that under a global sliding or global sticking condition, the blisk-damper system model is linear. Thus, linear modal analyses can be performed for the two global conditions by solving the following eigenvalue problems

$$[-\omega_{sl}^2\mathbf{M}_{CMS} + (\mathbf{K}_{CMS} + \mathbf{K}_{sl,CMS})]\mathbf{\Phi}_{sl,CMS} = 0, \tag{3.20}$$

$$[-\omega_{st}^2\mathbf{M}_{CMS} + (\mathbf{K}_{CMS} + \mathbf{K}_{st,CMS})]\mathbf{\Phi}_{st,CMS} = 0, \tag{3.21}$$

where ω_{sl} and ω_{st} are natural frequencies of a blisk-damper system under global sliding and sticking conditions, respectively. Vectors $\mathbf{\Phi}_{sl,CMS}$ and $\mathbf{\Phi}_{st,CMS}$ contain the corresponding system normal mode shapes. Note that all computations are performed in CB-CMS coordinates. Thus, the subscript CMS is dropped hereafter for notation simplicity.

Due to the ring-shaped geometry, the damper contains a small amount of mass, and is much softer than the blisk. Thus, the two sets of system normal mode shapes $\mathbf{\Phi}_{sl}$ and $\mathbf{\Phi}_{st}$ are nearly identical for all DOFs except those on or near the contact surfaces. The motion of the contact DOFs of $\mathbf{\Phi}_{sl}$ and $\mathbf{\Phi}_{st}$ represent contact dynamics in two limiting cases: zero slip motion, and full sliding. Forced responses of a blisk-damper system with frictional contact can be considered an intermediate state, when only a limited level of sliding motions is allowed. Such sliding motions are well captured by the difference between the contact DOFs of $\mathbf{\Phi}_{sl}$ and $\mathbf{\Phi}_{st}$, while the motions of the rest DOFs can be represented by either $\mathbf{\Phi}_{sl}$ or $\mathbf{\Phi}_{st}$. Based on the above observations, forced responses of a frictionally damped system are treated as a linear combination of $\mathbf{\Phi}_{sl}$ and $\mathbf{\Phi}_{st}$. Therefore, the CB-CMS model can be projected onto a new modal basis with the following transformation

$$\mathbf{x}^{(n)} = \begin{bmatrix}\mathbf{\Phi}_{st} & \mathbf{\Phi}_{sl}\end{bmatrix}\mathbf{q}^{(n)} = \mathbf{T}\mathbf{q}^{(n)}. \tag{3.22}$$

The modal equation of motion resulting from the stick-slip modal transformation can

be expressed as

$$\mathbf{d}^{(n)}\mathbf{q}^{(n)} = \mathbf{f}_e^{(n)} + \mathbf{f}_{nl}^{(n)}. \tag{3.23}$$

As a consequence of this transformation, Eqn. (3.23) does not possess any physical DOFs. Thus, the size of the ROM is not related to the number of nonlinear DOFs on the contact surface. Depending on the number of harmonic terms N_H used in the frequency domain formulation, and the number of mode shapes N_M included in the mode basis of stick-slip modal transformation $\mathbf{T}$, the resulting ROM has a small size of $(2N_H - 1)N_M$ variables. This novel technique to form such ROMs is named the method of coherent ring damper, or CoRiD.

3.2.4 Solution Method

3.2.4.1 Static Deformation Resulting from Pre-Stress

The initial normal load results from pre-stress, such as the centrifugal loading during engine operations, which holds the ring damper in contact with the blisk. Thus, depending on the level of pre-stress, as well as the geometry of the damper, the initial normal load applied on each contact node varies (and even may result in separation at certain contact node pairs). Hence, an iterative static analysis is performed for a given pre-stress to determine the initial normal load distribution and the contact status. In this static analysis, the contact surfaces are assumed to be frictionless, and each contact node pair is modeled as shown in Fig. 3.3a. This results in infinite static solutions due to the rotational rigid body motion of the ring damper. Thus, the contact surfaces are coupled at one node in the tangential direction. The static analysis procedure is outlined below.

Initially, nodes of each contact node pair coincide, with no forces acting in between. Next, for each contact node pair, the relative displacement v in the normal direction are computed, and the resulting normal contact forces are

$$N = \max(k_n v, 0). \tag{3.24}$$

Next, the residual of the balance equation is computed as

$$\mathbf{\Delta} = \mathbf{K}\mathbf{x}_0 - \mathbf{F}_0 - \mathbf{F}_{nl}, \tag{3.25}$$

where $\mathbf{x}_0$ is the static deformation due to the vector $\mathbf{F}_0$ of pre-stress. Note that $\mathbf{F}_0$ includes also the static (0^{th} harmonic) term of the external excitation force $\mathbf{F}_e^{(0)}$. $\mathbf{F}_{nl}$ is the vector

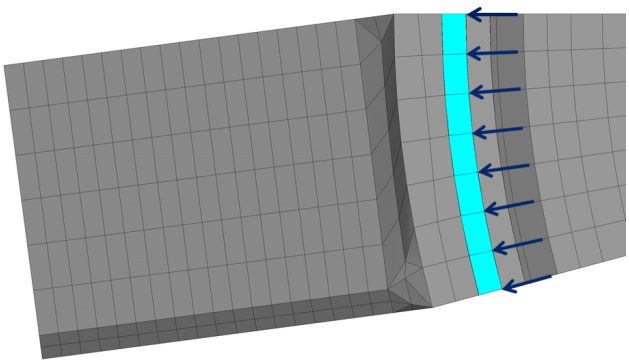

Figure 3.4: Pre-stress applied on the inner surface of the ring damper

of nonlinear forces assembled from normal contact forces at each node. $\mathbf{\Delta}$ represents the residual of the balance equation.

Then, if $\|\mathbf{\Delta}\| > \epsilon$, where ϵ is a small positive scalar, $\mathbf{x}_0$ is not a solution, and an updated value of $\mathbf{x}_0$ is computed by solving the following equation

$$\mathbf{K}\mathbf{x} = \mathbf{F}_0 + \mathbf{F}_{nl}. \tag{3.26}$$

The solution process is updated iteratively until a converged solution is obtained.

A converged solution of the static deformation $\mathbf{x}^0$, and the initial normal contact force $\mathbf{F}^0$ is obtained when $\|\mathbf{\Delta}\| \leq \epsilon$. The converged solution corresponds to the 0^{th} harmonic so that

$$\mathbf{x}^{(0)} = \mathbf{x}_0, \qquad \mathbf{F}_{nl}^{(0)} = \mathbf{F}_{nl}. \tag{3.27}$$

Note that in general, the centrifugal load is applied on every node of the blisk-damper system. To simplify the pre-stress and speed up the iterative computations, the centrifugal load is replaced by discrete nodal forces, pointing in the radial direction, applied on the inner surface of the ring damper, as shown in Fig. 3.4. This simplification does not preclude the proposed ROM from handling centrifugal loads or other complex types of pre-stress.

3.2.4.2 Hybrid Frequency/Time Method

The ROM model in Eqn. (3.23) consists of a set of nonlinear complex algebraic equations. This set of equations is solved by the hybrid frequency/time domain method introduced

by Guillen [45]. The HFT method is based on alternate transformations between the time and frequency domains. Contact forces acting on each node along the contact surfaces are evaluated in the time domain, while forced responses are obtained in the frequency domain by solving Eqn. (3.23). The procedure of the HFT method is outlined as

1. Initially, nodes of each contact node pair coincide, with no forces acting in between, and an initial guess of displacement in the frequency domain $\mathbf{x}^{(n)}$ is made.

2. An inverse fast Fourier transform is used to convert $\mathbf{x}^{(n)}$ for $n = 0, 1, \cdots, N_H$ into a time domain vector $\mathbf{x}(t)$ of displacements

3. For each contact node, the relative displacements are computed from $\mathbf{x}(t)$, and the contact forces $\mathbf{F}_{nl}(t)$ are obtained in the time domain from the macro-slip contact model.

4. A fast Fourier transform is used to convert contact forces into the frequency domain to obtain $\mathbf{F}_{nl}^{(n)}$ from $\mathbf{F}_{nl}(t)$ for $n = 0, 1, \cdots, N_H$.

5. The nonlinear forces $\mathbf{F}_{nl}^{(n)}$ are transformed into the reduced-order space based on the stick-slip modal transformation expressed in Eqn. (3.22) to obtain

$$\mathbf{f}_{nl}^{(n)} = \mathbf{T}^T \mathbf{F}_{nl}^{(n)}, \tag{3.28}$$

   and to compute the residual of Eqn. (**??**) as

$$\mathbf{\Delta}^{(n)} = \mathbf{d}^{(n)}\mathbf{q}^{(n)} - \mathbf{f}_e^{(n)} - \mathbf{f}_{nl}^{(n)}. \tag{3.29}$$

6. If $\sum_{n=0}^{N_H} ||\mathbf{\Delta}^{(n)}|| > \epsilon$, where ϵ is a small positive scalar, the solution has not converged yet, and $\mathbf{q}^{(n)}$ is computed by solving Eqn. (3.23). Next, $\mathbf{q}^{(n)}$ is transformed into physical domain based on Eqn. (3.22) to obtain $\mathbf{x}^{(n)}$, which serves as the input parameter for the next iteration,

$$\mathbf{x}^{(n)} = \mathbf{T}\mathbf{q}^{(n)}. \tag{3.30}$$

7. If $\sum_{n=0}^{N_H} ||\mathbf{\Delta}^{(n)}|| \leq \epsilon$, a converged solution has been reached, and the steady state forced response $\mathbf{x}^{(n)}$ and its time domain equivalent $\mathbf{x}(t)$ represent the forced response.

Note that the 0^{th} harmonic of the displacement in the frequency domain, $\mathbf{x}^{(0)}$, is linked to both the static responses computed in the previous section, and to the higher harmonics.

The HFT method is based on a continuation approach or on a Newton-Raphson-like solver. An initial guess of displacement $\mathbf{x}^{(n)}$ can be obtained by using the harmonic responses of a linear system under the same periodic forcing, where the entire contact surfaces remain stuck. Also, to compute the forced responses over a range of excitation frequencies, it is common practice to use the responses computed at a lower frequency as the initial condition at the next frequency step. However, with the softening or stiffening effects, bifurcations may occur, in which case two possible solutions exist at a single excitation frequency, and an increment of excitation frequency at the turning point can lead to the jump phenomenon. Thus, a pseudo-arc-length continuation method is used to ensure convergence [67].

3.3 Results and Discussion

3.3.1 Forced Response Analyses

The CoRiD method developed in this study is applied to the simplified academic model shown in Fig. 3.1, referred to as the UM Validation Blisk. Two examples are provided, including forced response analyses on a tuned system, and a system with small blade material mistuning. ROM-predicted results are validated against analyses performed on converged CB-CMS models. Note that all nonlinear equations are used in the validation model, and only the linear DOFs are reduced. The validations and error analyses focus on the accuracy of the stick-slip modal transformation, and the approximation of mistuning components by CB-CMS-CMM. Numerical error inherited by the classical CB-CMS method is negligible as the CB-CMS model is converged.

A traveling wave excitation is used in this study as external periodic forcing. It is the most common type of forcing used in analyzing blisk dynamics. A traveling wave excitation is a function of the engine order EO, and can be expressed as

$$\mathbf{f} = \sum_{j=1}^{N} \mathbf{F}_j \mathrm{e}^{-i(j-1)\mathrm{EO}\frac{2\pi}{N}}, \tag{3.31}$$

where $\mathbf{F}_j$ is the amplitude vector of the excitation on the j^{th} blade. Responses under excitations of lower EOs are expected to contain disk-dominated motions, in which case significant relative motions occur between the blisk and the ring damper, and the frictional damping is most effective. In contrast, under excitations of higher EOs, the blisk exhibits high levels of blade motions, and the effect of blade mistuning is stronger, whereas the

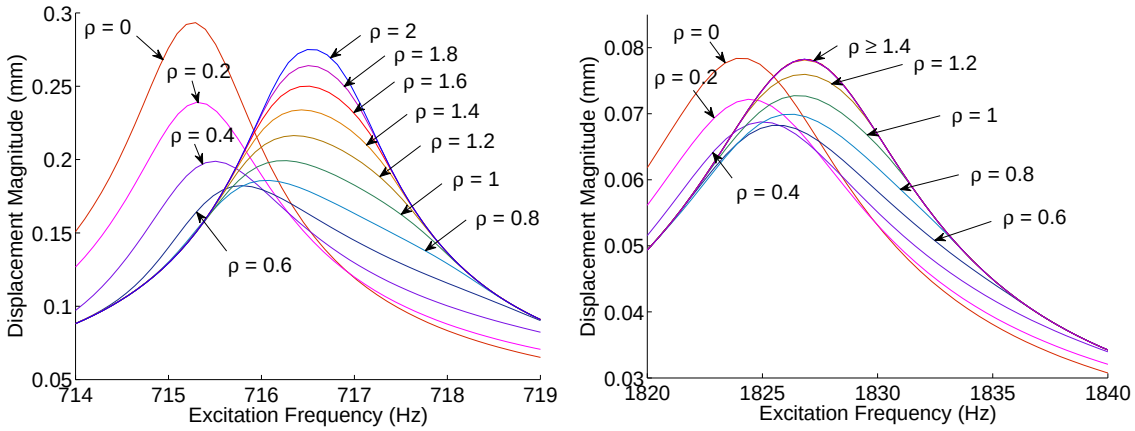

(a) EO 1 excitation

(b) EO 3 excitation

Figure 3.5: Forced responses of the tuned UM Validation Blisk under an EO 1 traveling wave excitation (left) and an EO 3 excitation (right)

frictional damping is ineffective. Thus, for the completeness of this study, traveling wave excitations of both engine orders 1 and 3 are adopted. To ensure a large blade deformation, the excitations are applied at the tip of each blade. Forced response are extracted at selected nodes, referred to as the response nodes, that are in proximity with the nodes on which the excitations are applied. Rayleigh damping ratio is chosen as $\alpha = 0$, and $\beta = 4.4396 \times 10^{-7}$, which corresponds to a damping ratio $\zeta = 4.0622 \times 10^{-4}$ at $\omega_n = 1,830$ Hz.

The first example includes forced response analyses of a tuned blisk-damper system. Responses are computed by using $N_H = 1$ in the HBM. Higher harmonics were used too, but they were found not to contribute significantly to the forced response.

To evaluate the relative importance and effects of the pre-stress magnitude N_0, the amplitude of external forcing $\|\mathbf{F}_j\| = F$, and the coefficient of friction μ, the ratio $\rho = \frac{\mu N_0}{F}$ is used in this study. Figure 3.5a shows the maximum response amplitude across all response nodes, under an EO 1 traveling wave excitation. Responses are extracted at each forcing frequency, and at each ρ value, ranging from 0 to 2. A maximum response is obtained at $\rho = 0$, where the contact surfaces can slide freely relative to each other. In this case, no energy dissipation by friction exists. As ρ increases, so does the effectiveness of friction damping, leading to a lower response amplitude. A minimum response amplitude is observed at $\rho = 0.6$. As ρ increases beyond 0.6 and approaches 2, it becomes more difficult for the contact surfaces to slide against each other, resulting in less energy dissipation and a higher response amplitude.

The ROM-predicted results are validated at three values of ρ: $\rho = 0$, 0.6, and 2. The

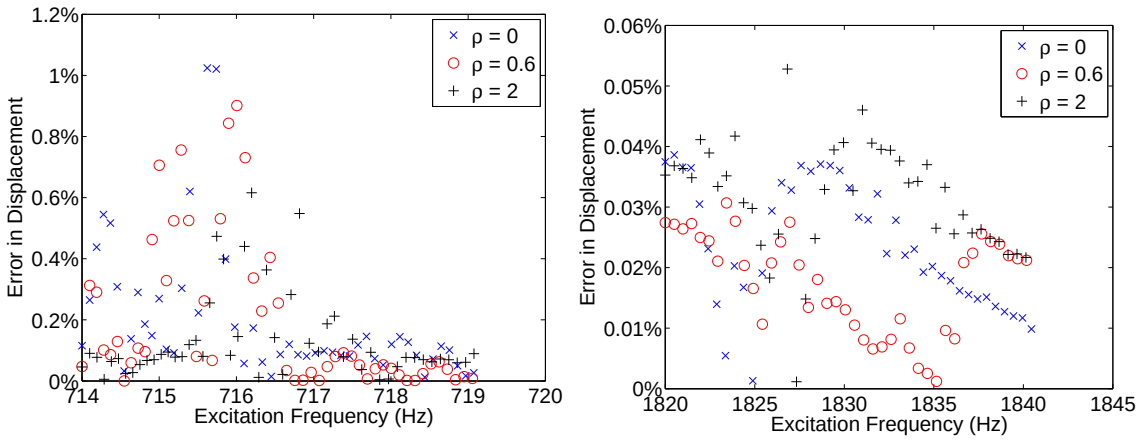

(a) EO 1 excitation

(b) EO 3 excitation

Figure 3.6: Error in forced responses of the tuned UM Validation Blisk under an EO 1 excitation (left) and an EO 3 excitation (right) at different ρ values

relative errors between the ROM results and the validation data are shown in Fig. 3.6a. The maximum relative error occurs at $\rho = 0$, and is approximately 1.02%. A better accuracy is observed in the forced responses under an EO 3 excitation (Fig. 3.6b), with a maximum relative error of 0.105%. Such a small error indicates that the nonlinear contact dynamics are accurately captured by the method of the stick-slip modal transformation. Note that in Fig. 3.5b, the reduction of the amplitude due to frictional damping is approximately 13.0%, smaller than the reduction ratio of 37.9% observed in the case of EO 1 excitation (Fig. 3.5a). This behavior indicates a better effectiveness of the ring damper at lower EOs.

The second example considers small blade mistuning in material properties applied to all blade components by varying their Young's modulus by a small percentage from the nominal value. Such variations are randomly chosen following a normal distribution with a 0 mean and a 2% standard deviation. The forced responses of the mistuned blisk-damper system under EO 1 and EO 3 traveling wave excitations are shown in Fig. 3.7. Validation data reveals that the maximum relative error in mistuned forced responses is approximately 1.32%, observed in the case of an EO 1 excitation (Fig. 3.8a). Note that in the CB-CMS-CMM method, the mistuning components of the dynamic stiffness are projected onto CB modes, which are computed with the root of the blade held fixed. This boundary condition assumes that little or no motion exists on the disk-blade interfaces. This assumption is less accurate when the blisk is subject to traveling wave excitations of low EOs. In this case, the root of each blade may contain high levels of motions. Thus, the error of 1.32% can be viewed as a worst case scenario for CMM. Thus, the CB-CMS-CMM approximation can be considered accurate.

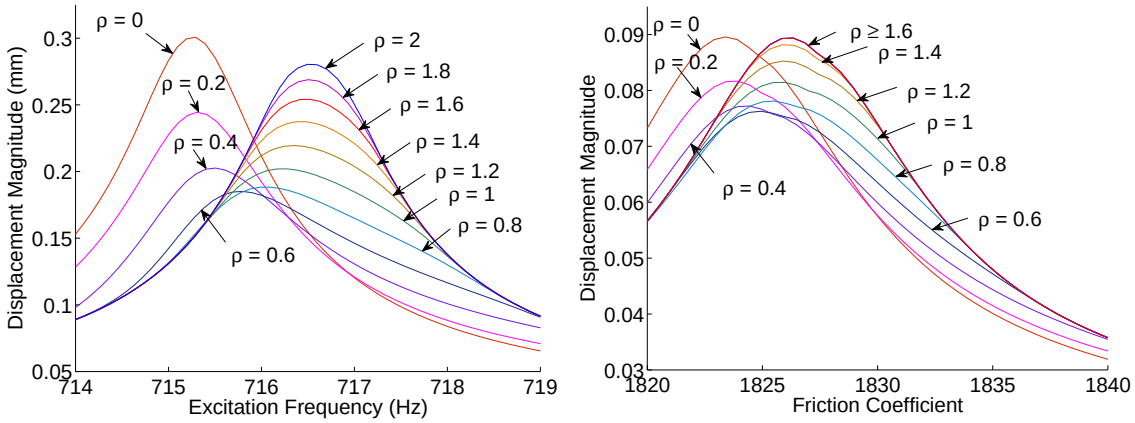

(a) EO 1 excitation

(b) EO 3 excitation

Figure 3.7: Forced responses of a mistuned UM Validation Blisk under an EO 1 traveling wave excitation (left) and an EO 3 excitation (right)

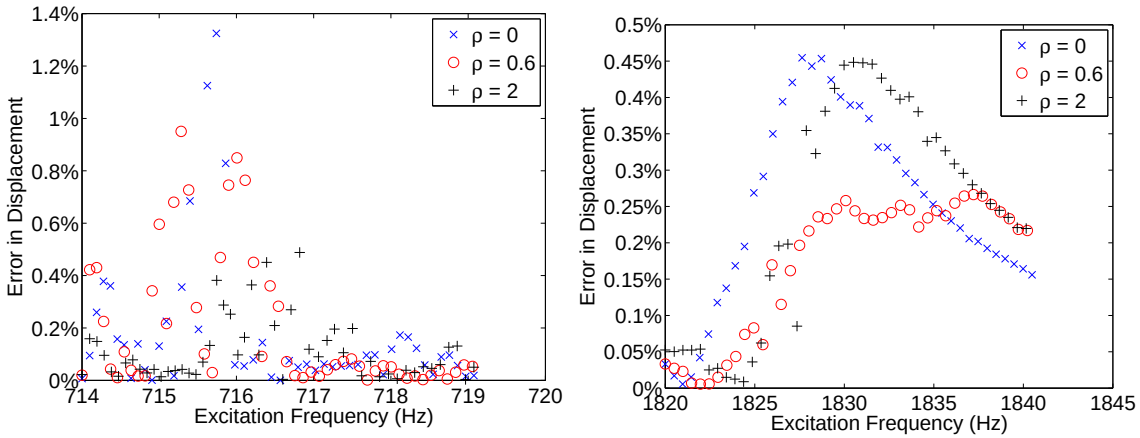

(a) EO 1 excitation

(b) EO 3 excitation

Figure 3.8: Error in forced responses of a mistuned UM Validation Blisk under an EO 1 excitation (left) and an EO 3 excitation (right) at different ρ values

3.3.2 Statistical Analyses

With the fast computations and good accuracy provided by the CoRiD method, it is possible to sample the blisk-damper system over a large number of mistuning patterns to study the correlation between random mistuning and effectiveness of the friction ring dampers. In this study, a Monte-Carlo analysis is demonstrated for the UM validation blisk, with 100 samples of mistuning patterns included. Each of the mistuning patterns is generated in the same way as described in the previous section, namely small variations in Young's modulus are applied to all blade components following a normal distribution with a 0 mean and a 2% standard deviation. A traveling wave excitation of EO 1 is applied.

It is well know that in the presence of mistuning, strain energy localization may occur, and can lead to drastic amplification of forced responses. Thus, it is useful to define a metric so that the amplification of forced responses due to mistuning can be evaluated. In this study, this metric is defined by comparing the maximum magnitude of forced responses at all pre-selected response nodes of the mistuned system with that of a tuned system, under the same forcing conditions. This metric is called the amplification factor $AF_x(\rho)$ and is defined as

$$AF_x(\rho) = \frac{\max_\omega(\max_{i=1}^{N_{node}}(\|\mathbf{x}_i^m(\rho)\|))}{\max_\omega(\max_{i=1}^{N_{node}}(\|\mathbf{x}_i^0(\rho)\|))}, \tag{3.32}$$

where N_{node} is the number of response nodes, and ω is the forcing frequency. Superscript m stands for a mistuned system, whereas 0 stands for a tuned system. Note that the amplification factor is computed with mistuned and tuned responses for the same ρ value.

Figure 3.9 shows the probability distribution of the amplification factors extracted from the Monte-Carlo analysis. The analysis is performed for a frictionless case ($\rho = 0$), and for the case with a ρ value of 0.6, where the friction damper is likely to be effective. It is observed that the distribution of amplification factors does not vary significantly, and reveals that frictional damping has a small effect on the amplification of forced responses due to mistuning. However, the correlation of the effects of mistuning and friction damping is mutual.

The analysis is not conclusive without also evaluating the effect of mistuning on the effectiveness of friction damping. This effect can be measured by a reduction ratio $RR_x(\rho)$, defined as the maximum percentage reduction of forced response amplitudes resulting from

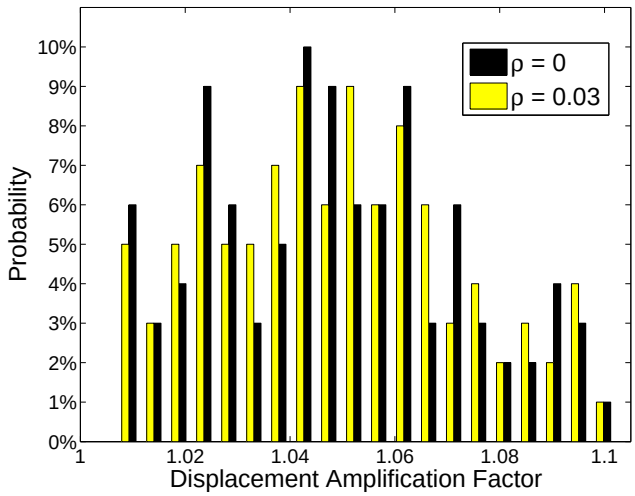

Figure 3.9: Probability distribution of amplification factors of forced responses with random mistuning patterns computed with ρ values of 0 and 0.6

frictional damping, namely

$$RR_x(\rho) = 1 - \frac{\max_\omega \max_{i=1}^{N_{node}} ||\mathbf{x}_i^m(\rho)||}{\max_\omega \max_{i=1}^{N_{node}} ||\mathbf{x}_i^m(0)||}. \tag{3.33}$$

Again, in this analysis the value of ρ is selected to be 0.6, where the frictional damping is expected to be effective. Figure 3.10 contains the reduction ratio of the forced responses for the UM Validation Blisk with each mistuning pattern included in the Monte-Carlo analysis. The reduction ratios are sorted from the lowest to the highest value. It is noteworthy that the friction damping is least effective in the tuned system, with a reduction ratio of 37.9%. Most mistuning patterns are associated with higher reduction of the response amplitude, with a maximum ratio of 40.0%. This analysis reveals that the ring-shaped friction damper is more effective when small mistuning is present in the blade components.

Note that with the ROMs constructed by CoRiD, the above statistical analysis that involves 100 mistuning patterns consumes approximately 4 days of CPU time. In contrast, conventional methods such as numerical time integration performed on a full-order model may require at least 800 days of CPU time to obtain the same forced responses.

3.4 Conclusions

A novel reduced-order modeling technique, capable of capturing nonlinear forced responses of mistuned bladed disks with frictional ring dampers, was presented. The CoRiD

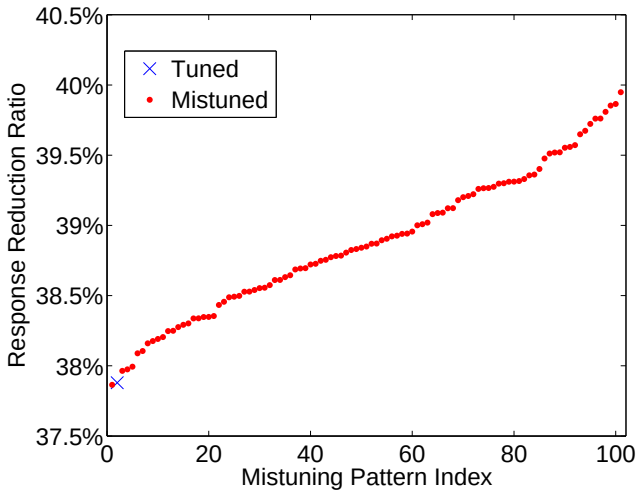

Figure 3.10: Reduction ratios (ordered in increasing value) of forced response amplitudes resulting from frictional damping for all 100 mistuning patterns

method contains a series of model reduction steps, and has the following attractive features.

1. The stick-slip modal transformation accurately mimics the dynamics of the contact surfaces. It reduces the size of blisk-damper models to the number of a few modal coordinates, which is not affected by the number of the contact DOFs. Thus, this method can be applied to models with highly refined contact surfaces.

2. By extending the classical CB-CMS technique with the CMM method, which results in the CB-CMS-CMM method, the mistuning component of the dynamic stiffness matrix can be directly computed in the ROM coordinates. Therefore, repetitive CB-CMS model reductions for systems associated with different mistuning patterns can be avoided.

3. The ROMs provided by the CoRiD method are compact, and require minimal amount of computational cost. Thus, they are suitable for statistical analyses to study the blisk dynamics under various forcing, mistuning, and damping conditions.

Forced response computations have been performed on the UM Validation Blisk. The results have been proven accurate. A statistical analysis has shown a noteworthy correlation between the small mistuning and the effectiveness of the ring damper in reducing the maximum response amplitude. One important area for future development is to extend the CoRiD method to model blisk-damper systems with not only small blade mistuning, but also significant changes in mass, stiffness, and geometry.

CHAPTER 4

Reduced Order Models for Blisks with Small and Large Mistuning and Friction Dampers

4.1 Introduction

In operation, rotating blisks are often subject to high levels of dynamic loading, resulting in large amplitudes of forced vibrations especially at resonance. Moreover, variations in structural properties of individual sectors, referred to as mistuning, can lead to strain energy localization and can amplify forced responses. To prevent damages caused by high cycle fatigue, frictional damping sources are introduced to dissipate vibration energy. Due to the nonlinear behavior of frictional contacts, conventional methods to study the dynamics of the blisk-damper systems are based often on numerical time integration, which is time-consuming and can be computationally prohibitive due to the large sizes of commercial blisk models. Existing techniques for model reduction either rely heavily on cyclic symmetry of the blisk-damper system, or are based on CMS techniques. However, in the presence of mistuning, cyclic symmetry no longer exists. Also, mistuning is random and best studied statistically. Repetitive CMS condensation for a large amount of random mistuning patterns can lead to a computationally formidable task.

The CoRiD method, introduced in Chapter II, is developed to address this issue. CoRiD projects the blisk-damper system onto a small mode basis that can accurately mimic the relative motions between the contact surfaces. The CoRiD mode basis consists of two sets of mode shapes: 1) mode shapes extracted from a blisk-damper system within which two mating contact surfaces are completely stuck together, and 2) mode shapes extracted when the contact surfaces can fully slide relative to each other. ROMs provided by CoRiD are compact and possess no physical DOFs. However, note that the mode basis formed by the CoRiD method requires system normal mode shapes. In the presence of mistuning, the amount of computations required for repetitive system-level modal analyses can be prohibitive. Therefore, it is necessary to extend the current CoRiD method with an efficient

reduced-order modeling technique that provides the required mode shapes with significantly less computational effort. The objective of this study is to combine the methods of N-PRIME and CoRiD to form a comprehensive tool to study the effectiveness of frictional ring dampers when the blisk suffers from high-level forced responses due to simultaneous large and small mistuning. The N-PRIME method is used to compute the system normal mode shapes of a mistuned blisk-damper system with the two types of contact status, which are further used as the input to the CoRiD method to form the mode basis for system reduction. The resulting reduced-order modeling technique can efficiently capture the nonlinear dynamic responses of blisk-damper systems with both small perturbations in blade material properties (small mistuning), and significant changes in the blisk geometries (large mistuning). Modal nonlinear equations of motion in the reduced-order space are solved by a HFT method with continuation. In the HFT method, the contact status and friction forces are determined in the time domain by a quasi-two-dimensional contact model at each contact point, whereas the modal equations of motion are solved in the frequency domain according to a harmonic balance formulation.

This section is organized as follows. The implementation of the CoRiD method, and its extension with N-PRIME, are introduced in the next section. The reduced-order modeling technique developed in this study, named PRIME-CoRiD, is applied to the UM Validation Blisk model, shown in Fig. 3.1. ROM-predicted forced responses for mistuned blisks are retrieved and validated. Since the computational effort required by the PRIME-CoRiD method is minimal, it is suitable for statistical analyses to reveal the influence of random mistuning on the effectiveness of the dry friction ring dampers. A typical statistical analysis is provided as well.

4.2 Reduced-Order Modeling

4.2.1 Harmonic Balance Formulation

Consider a model of a general blisk-damper system coupled through nonlinear friction forces

$$\mathbf{M}\ddot{\mathbf{x}}(t) + \beta\mathbf{K}\dot{\mathbf{x}}(t) + \mathbf{K}\mathbf{x}(t) = \mathbf{F}_e(t) + \mathbf{F}_{nl}(t), \tag{4.1}$$

where $\mathbf{M}$ and $\mathbf{K}$ are the mass and stiffness matrices of the blisk-damper system, and β is the stiffness-proportional damping coefficient. $\mathbf{F}_e(t)$ represents the external periodic forcing function. $\mathbf{F}_{nl}(t)$ represents the nonlinear contact forces. Note that the contact surfaces

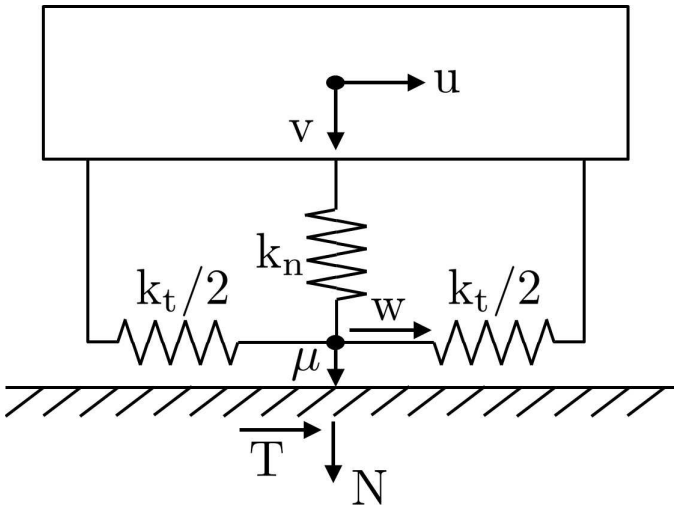

Figure 4.1: A 3D macro-slip contact model

between the blisk and the damper are discretized into contact node pairs, and the contact force $\mathbf{F}_{nl}(t)$ acting between each node pair is a nonlinear function of relative displacements and velocities between the two contact nodes. In this study, the contact forces are captured by a 2-1D contact model, consisting of a pair of 1D macro-slip models with normal load variations [26], respectively modeling the the contact dynamics between a contact node pair in each tangential direction on the contact surfaces, as shown in Fig. 4.1. The detailed description of the contact model and the transition criteria of contact status can be found in Sec. 3.2.2.

As mentioned previously, solving Eqn. (4.1) directly in the time domain through numerical time integration requires a large amount of iterations before the solution reaches steady state. Thus, the harmonic balance method (HBM) is introduced to transform Eqn. (4.1). The assumption in HBM formulation is that under periodic external forcing, steady-state responses of a non-linear system remain periodic. Thus, the variables involved in Eqn. (4.1), including the displacement $\mathbf{x}(t)$, the external forcing $\mathbf{F}_e(t)$, and the nonlinear force $\mathbf{F}_{nl}(t)$, can be approximated by a truncated sum of harmonic terms, written as

$$\begin{aligned}
\mathbf{x}(t) &= \mathbf{x}^{(0)} + \mathrm{Re}\left(\sum_{n=1}^{N_H} \mathbf{x}^{(n)} e^{in\omega t}\right), \\
\mathbf{F}_e(t) &= \mathbf{F}_e^{(0)} + \mathrm{Re}\left(\sum_{n=1}^{N_H} \mathbf{F}_e^{(n)} e^{in\omega t}\right), \\
\mathbf{F}_{nl}(t) &= \mathbf{F}_{nl}^{(0)} + \mathrm{Re}\left(\sum_{n=1}^{N_H} \mathbf{F}_{nl}^{(n)} e^{in\omega t}\right),
\end{aligned} \tag{4.2}$$

where N_H is the number of harmonics used in the HBM formulation, and ω is the angular frequency of periodic forcing $\mathbf{F}_e(t)$. Substituting Eqn. (4.2) into Eqn. (4.1), the ordinary differential equation is transformed into a set of N_H complex algebraic equations as

$$\mathbf{D}^{(n)}\mathbf{x}^{(n)} = \mathbf{F}_e^{(n)} + \mathbf{F}_{nl}^{(n)}, \tag{4.3}$$

where $\mathbf{x}^{(n)}$ is the n^{th} harmonic of the vector of displacement, and $\mathbf{D}^{(n)}$ is the n^{th} harmonic of the dynamic stiffness matrix of the blisk-damper system, expressed as

$$\mathbf{D}^{(n)} = -(n\omega)^2\mathbf{M} + (1 + i\beta n\omega)\mathbf{K}. \tag{4.4}$$

4.2.2 Stick-Slip Modal Transformation

Full-order FE models of industrial blisk-damper systems in general contain many DOFs, and thus solving Eqn. (4.3) in the frequency domain can be a formidable task. To reduce the computational effort required to solve the large set of nonlinear algebraic equations. A novel reduced-order modeling technique is proposed to reduce the size of Eqn. (4.3).

Consider two nodes of a contact node pair that can freely slide relative to each other. In this case, the tangential stiffness between the two contact nodes has no effects. An equivalent model for the contact node pair in the sliding condition can be constructed by removing the tangential contact stiffness from the 1D macro-slip model. This modification is shown in Fig. 4.2a. Similarly, two nodes within a contact node pair that are stuck to each other can be modeled by bonding the Coulomb slider to the contact surface, so that no slip motion is allowed, as shown in Fig. 4.2b. According to the two models, a local contact stiffness matrix for a contact node pair in sliding and sticking conditions can be defined respectively as the following

$$\mathbf{k}_{sl,l} = \begin{bmatrix} 0 & 0 & 0 \\ 0 & 0 & 0 \\ 0 & 0 & k_n \end{bmatrix}, \qquad \mathbf{k}_{st,l} = \begin{bmatrix} k_t & 0 & 0 \\ 0 & k_t & 0 \\ 0 & 0 & k_n \end{bmatrix}. \tag{4.5}$$

where the subscript l indicates that the contact stiffness matrices are expressed in the local contact coordinates at node i, and can be transformed into the global (cylindrical) coordinate system by using the rotation matrix $\mathbf{R}_i$, as follows

$$\mathbf{k}_{sl,i} = \mathbf{R}_i\mathbf{k}_{sl,l}\mathbf{R}_i^T, \qquad \mathbf{k}_{st,i} = \mathbf{R}_i\mathbf{k}_{st,l}\mathbf{R}_i^T. \tag{4.6}$$

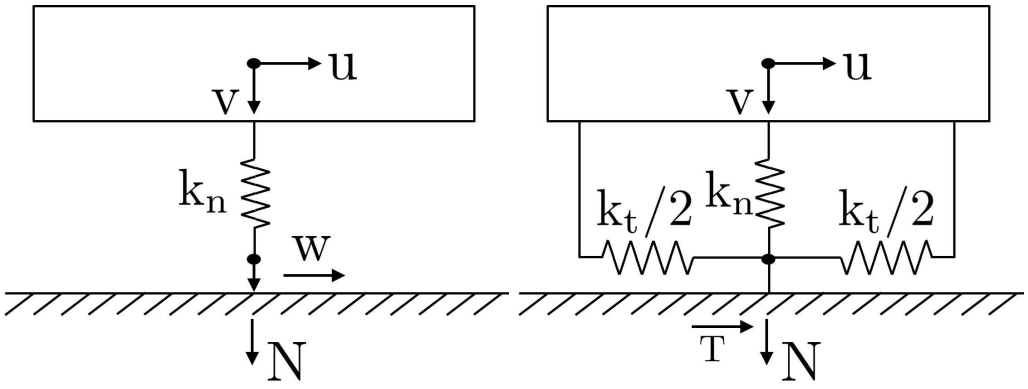

(a) Sliding condition (b) Sticking condition

Figure 4.2: Contact models for a node pair of two frictionless contact states

Consider a global contact status where the two mating contact surfaces can slide freely relative to each other. This status is defined as the global sliding condition, for which a global contact stiffness matrix $\mathbf{K}_{sl}$ can be assembled by summing the contributions of each local contact stiffness matrix $\mathbf{k}_{sl,i}$. Similarly, for a global sticking condition, where the entire contact surfaces are stuck, a global contact stiffness matrix $\mathbf{K}_{st}$ can be assembled from the local contact stiffness matrix $\mathbf{k}_{st,i}$. Note that under both global sliding and sticking conditions, the contact surfaces can be considered frictionless. A linear modal analysis can be performed for each of the global contact states by solving the following eigenvalue problems

$$[-\omega_{sl}^2\mathbf{M} + (\mathbf{K} + \mathbf{K}_{sl})]\mathbf{\Phi}_{sl} = 0, \tag{4.7}$$

$$[-\omega_{st}^2\mathbf{M} + (\mathbf{K} + \mathbf{K}_{st})]\mathbf{\Phi}_{st} = 0, \tag{4.8}$$

where ω_{sl} and ω_{st} are natural frequencies of a blisk-damper system with the contact surfaces under global sliding and sticking conditions, respectively. $\mathbf{\Phi}_{sl}$ and $\mathbf{\Phi}_{st}$ contain the corresponding system normal mode shapes. Equation (4.1) can be projected onto a mode basis formed with $\mathbf{\Phi}_{sl}$ and $\mathbf{\Phi}_{st}$ by the following transformation

$$\mathbf{x}^{(n)} = \begin{bmatrix}\mathbf{\Phi}_{st} & \mathbf{\Phi}_{sl}\end{bmatrix}\mathbf{q}^{(n)} = \mathbf{T}\mathbf{q}^{(n)}. \tag{4.9}$$

The fundamental assumption for the above transformation is that the forced responses of a blisk-damper system with frictional contact surfaces can be approximated as a linear combination of the normal mode shapes of the same system under global sliding and stick-

ing conditions. Due to its ring-shaped geometry, the damper contains a small amount of mass and is much softer than the blisk. Thus, the two sets of normal mode shapes $\mathbf{\Phi}_{sl}$ and $\mathbf{\Phi}_{st}$ are nearly identical for all DOFs of the blisk-damper system, except for those on the contact surfaces. The motion of the contact DOFs of $\mathbf{\Phi}_{sl}$ and $\mathbf{\Phi}_{st}$ represents the contact dynamics in two extreme cases: no sliding motion allowed, and free sliding. A frictional contact results in forced responses of an intermediate state, where only certain sliding motions are allowed on the contact surfaces. Such sliding motions are well captured by the difference between the contact DOFs of $\mathbf{\Phi}_{sl}$ and $\mathbf{\Phi}_{st}$, while the responses of the rest DOFs can be represented by either $\mathbf{\Phi}_{sl}$ or $\mathbf{\Phi}_{st}$. Thus, the mode basis proposed in Eqn. (4.9) is expected to accurately capture forced responses with a frictional contact status. The modal equation of motion resulting from the stick-slip modal transformation has the following form

$$\mathbf{d}^{(n)}\mathbf{q}^{(n)} = \mathbf{f}_e^{(n)} + \mathbf{f}_{nl}^{(n)}. \tag{4.10}$$

where $\mathbf{d}^{(n)} = \mathbf{T}^T\mathbf{D}^{(n)}\mathbf{T}$, $\mathbf{f}_e^{(n)} = \mathbf{T}^T\mathbf{F}_e^{(n)}$, and $\mathbf{f}_{nl}^{(n)} = \mathbf{T}^T\mathbf{F}_{nl}^{(n)}$.

As a consequence of this transformation, Eqn. (4.10) does not possess any physical DOFs. Thus, the size of Eqn. (4.10) is not related to the number of nonlinear DOFs on the contact surface. Depending on the number of harmonic terms N_H used in the frequency domain formulation, and the number of mode shapes N_M included in the mode basis $\mathbf{T}$, the resulting ROM resembles a compact system, with only $(2N_H - 1)N_M$ variables.

4.2.3 Extension with N-PRIME

Note that Eqns. (4.7) and (4.8) are system-level equations, and the computational cost involved in solving both equations can be prohibitively high. The ROM formulated as Eqn. (4.10) is first introduced by the authors in combination with the CB-CMS technique to replace the full-order system with a condensed model. However, a general blisk-damper system can be mistuned, and reconstructing the CB-CMS model for each mistuning pattern can result in unaffordable amount of computations.

The method of N-PRIME is constructed under the frame of pristine-rogue-interface modal expansion, and is designed to efficiently compute the free responses of a blisk with simultaneous large and small mistuning. Consider a free response problem for a mistuned blisk-damper system as follows

$$\left[-\omega^2\mathbf{M} + \bar{\mathbf{K}}\right]\mathbf{x} = \mathbf{0}, \tag{4.11}$$

where $\mathbf{M}$ and $\bar{\mathbf{K}}$ are system mass and stiffness matrices. Note that matrix $\bar{\mathbf{K}}$ includes the stiffness component of the blisk-damper system $\mathbf{K}$ and the contact stiffness between the blisk and the damper, which can be $\mathbf{K}_{sl}$ or $\mathbf{K}_{st}$, depending on the status of the contact surfaces. In the presence of large mistuning, the assumption suggested by Yang et al. [14] that the mistuned mode shapes can be expressed as linear combination of tuned mode shapes is no longer valid. One trivial reason for the assumption to fail is that in the case of missing material, tuned and mistuned mode shapes do not possess the same number of DOFs. Thus, Eqn. (4.11) cannot be directly projected on to the tuned system normal modes to form the ROM.

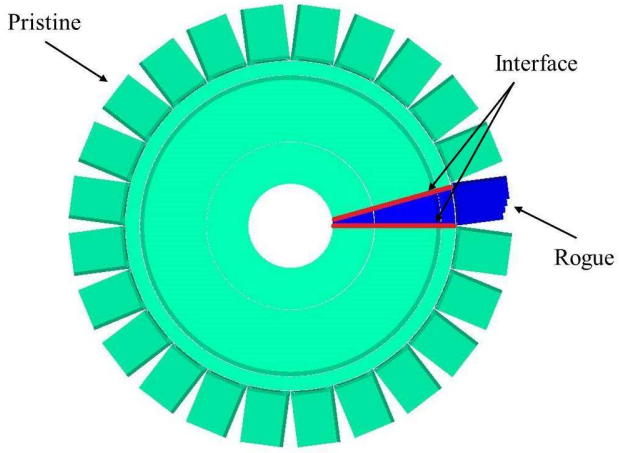

Figure 4.3: A mistuned UM validation blisk partitioned by PRIME

Figure 4.3 shows a typical mistuned system with a large volume of missing material. It can be partitioned into three components: a pristine component which consists of DOFs of sectors whose structural properties are identical to a nominal sector, a rogue component which consists of DOFs of sectors that have large mistuning, and an interface component that connects the pristine and rogue components. The partitioned mass and stiffness matrices are formulated as

$$\mathbf{M} = \begin{bmatrix} \mathbf{M}^{\mathrm{PP}} & \mathbf{M}^{\mathrm{PR}} & \mathbf{M}^{\mathrm{PI}} \\ \mathbf{M}^{\mathrm{RP}} & \mathbf{M}^{\mathrm{RR}} & \mathbf{M}^{\mathrm{RI}} \\ \mathbf{M}^{\mathrm{IP}} & \mathbf{M}^{\mathrm{IR}} & \mathbf{M}^{\mathrm{II}} \end{bmatrix}, \qquad \bar{\mathbf{K}} = \begin{bmatrix} \bar{\mathbf{K}}^{\mathrm{PP}} & \bar{\mathbf{K}}^{\mathrm{PR}} & \bar{\mathbf{K}}^{\mathrm{PI}} \\ \bar{\mathbf{K}}^{\mathrm{RP}} & \bar{\mathbf{K}}^{\mathrm{RR}} & \bar{\mathbf{K}}^{\mathrm{RI}} \\ \bar{\mathbf{K}}^{\mathrm{IP}} & \bar{\mathbf{K}}^{\mathrm{IR}} & \bar{\mathbf{K}}^{\mathrm{II}} \end{bmatrix}. \tag{4.12}$$

The PRIME method is based on the following assumption. The pristine DOFs of the mistuned mode shapes can be represented by a linear combination of the corresponding DOFs of a basis assembled from the cyclic modes computed for a pristine sector ($\mathbf{\Phi}^{\mathrm{P}}$). Similarly, the rogue DOFs of the mistuned mode shapes can be represented by a linear

combination of the corresponding DOFs of a basis assembled from the cyclic modes computed for rogue sectors ($\mathbf{\Phi}^{\mathrm{R}}$). These cyclic modes can be inexpensively extracted from cyclic symmetry modal analysis performed for a single pristine and each of the rogue sectors. With the above assumption, a preliminary PRIME mode basis can be assembled as follows

$$\mathbf{\Phi}^{\mathrm{PRI}} = \begin{bmatrix} \mathbf{\Phi}^{\mathrm{P}} & \mathbf{0} & \mathbf{0} \\ \mathbf{0} & \mathbf{\Phi}^{\mathrm{R}} & \mathbf{0} \\ \mathbf{0} & \mathbf{0} & \mathbf{\Phi}^{\mathrm{I}} \end{bmatrix}. \tag{4.13}$$

Note that each interface component is shared by a pristine and a rogue sector, and is included as the cyclic boundary during the cyclic symmetry modal analysis for both sectors. To ensure displacement compatibility on the interface, it is assumed that in the PRIME mode basis, the mode shapes of the interface component can be represented by the corresponding DOFs of the cyclic mode shapes of a tuned sector. This assumption is valid since all interface DOFs are on the rigid disk component, and thus the variations between the interface mode shapes of a pristine and a rogue sector are negligible. Projecting the mass and stiffness matrices of the mistuned system onto the PRIME mode basis yields the following ROM matrices

$$\begin{aligned} \mathbf{M}_{\mathrm{PRI}} &= \mathbf{\Phi}^{\mathrm{PRI}T}\mathbf{M}\mathbf{\Phi}^{\mathrm{PRI}} \\ &= \begin{bmatrix} \mathbf{\Phi}^{\mathrm{P}\,\mathrm{T}}\mathbf{M}^{\mathrm{PP}}\mathbf{\Phi}^{\mathrm{P}} & \mathbf{\Phi}^{\mathrm{P}\,\mathrm{T}}\mathbf{M}^{\mathrm{PR}}\mathbf{\Phi}^{\mathrm{R}} & \mathbf{\Phi}^{\mathrm{P}\,\mathrm{T}}\mathbf{M}^{\mathrm{PI}}\mathbf{\Phi}^{\mathrm{I}} \\ \mathbf{\Phi}^{\mathrm{R}\,\mathrm{T}}\mathbf{M}^{\mathrm{RP}}\mathbf{\Phi}^{\mathrm{P}} & \mathbf{\Phi}^{\mathrm{R}\,\mathrm{T}}\mathbf{M}^{\mathrm{RR}}\mathbf{\Phi}^{\mathrm{R}} & \mathbf{\Phi}^{\mathrm{R}\,\mathrm{T}}\mathbf{M}^{\mathrm{RI}}\mathbf{\Phi}^{\mathrm{I}} \\ \mathbf{\Phi}^{\mathrm{I}\,\mathrm{T}}\mathbf{M}^{\mathrm{IP}}\mathbf{\Phi}^{\mathrm{P}} & \mathbf{\Phi}^{\mathrm{I}\,\mathrm{T}}\mathbf{M}^{\mathrm{IR}}\mathbf{\Phi}^{\mathrm{R}} & \mathbf{\Phi}^{\mathrm{I}\,\mathrm{T}}\mathbf{M}^{\mathrm{II}}\mathbf{\Phi}^{\mathrm{I}} \end{bmatrix}, \\ \bar{\mathbf{K}}_{\mathrm{PRI}} &= \mathbf{\Phi}^{\mathrm{PRI}T}\bar{\mathbf{K}}\mathbf{\Phi}^{\mathrm{PRI}} \\ &= \begin{bmatrix} \mathbf{\Phi}^{\mathrm{P}\,\mathrm{T}}\bar{\mathbf{K}}^{\mathrm{PP}}\mathbf{\Phi}^{\mathrm{P}} & \mathbf{\Phi}^{\mathrm{P}\,\mathrm{T}}\bar{\mathbf{K}}^{\mathrm{PR}}\mathbf{\Phi}^{\mathrm{R}} & \mathbf{\Phi}^{\mathrm{P}\,\mathrm{T}}\bar{\mathbf{K}}^{\mathrm{PI}}\mathbf{\Phi}^{\mathrm{I}} \\ \mathbf{\Phi}^{\mathrm{R}\,\mathrm{T}}\bar{\mathbf{K}}^{\mathrm{RP}}\mathbf{\Phi}^{\mathrm{P}} & \mathbf{\Phi}^{\mathrm{R}\,\mathrm{T}}\bar{\mathbf{K}}^{\mathrm{RR}}\mathbf{\Phi}^{\mathrm{R}} & \mathbf{\Phi}^{\mathrm{R}\,\mathrm{T}}\bar{\mathbf{K}}^{\mathrm{RI}}\mathbf{\Phi}^{\mathrm{I}} \\ \mathbf{\Phi}^{\mathrm{I}\,\mathrm{T}}\bar{\mathbf{K}}^{\mathrm{IP}}\mathbf{\Phi}^{\mathrm{P}} & \mathbf{\Phi}^{\mathrm{I}\,\mathrm{T}}\bar{\mathbf{K}}^{\mathrm{IR}}\mathbf{\Phi}^{\mathrm{R}} & \mathbf{\Phi}^{\mathrm{I}\,\mathrm{T}}\bar{\mathbf{K}}^{\mathrm{II}}\mathbf{\Phi}^{\mathrm{I}} \end{bmatrix}. \end{aligned} \tag{4.14}$$

Note that the number of rows of $\mathbf{\Phi}^{\mathrm{PRI}}$ is the number of all DOFs of the full mistuned system. Thus, formulating the PRIME ROMs through direct matrix multiplication suggested by Eqn. (4.14) can be computationally expensive. However, the mode shapes contained by the PRIME mode basis $\mathbf{\Phi}^{\mathrm{PRI}}$ are sector-level cyclic modes expanded to corresponding pristine and rogue DOFs. Also, the mass and stiffness matrices of the mistuned system are block-diagonal in nature. Thus, the above projection can be performed as a sum of sector-level projections, and reduce the computational effort involved.

To enable the PRIME method to efficiently formulate ROMs for systems with both large and small mistuning, a modified version of the NEWT approach is integrated into the PRIME frame. Consider the equations of motion of a blisk with simultaneous large and small mistuning

$$\left[-\omega^2(\mathbf{M}+\mathbf{M}^{\delta})+\bar{\mathbf{K}}+\bar{\mathbf{K}}^{\delta}\right]\mathbf{x}=\mathbf{0}, \tag{4.15}$$

where $\mathbf{M}^{\delta}$ and $\bar{\mathbf{K}}^{\delta}$ are the small mistuning components of the system mass and stiffness matrices. Projecting the mistuning components onto the PRIME mode basis transforms Eqn. (4.15) into the reduced-order coordinates as

$$\begin{aligned}\Big[-\omega^2(\mathbf{M}^{\mathrm{PRI}}+\boldsymbol{\Phi}^{\mathrm{PRI}^{\mathrm{T}}}\mathbf{M}^{\delta}\boldsymbol{\Phi}^{\mathrm{PRI}})+\bar{\mathbf{K}}^{\mathrm{PRI}}+\ldots\\ \ldots+\boldsymbol{\Phi}^{\mathrm{PRI}^{\mathrm{T}}}\bar{\mathbf{K}}^{\delta}\boldsymbol{\Phi}^{\mathrm{PRI}}\Big]\mathbf{p}^{\mathrm{PRI}}=\mathbf{0}.\end{aligned} \tag{4.16}$$

The mass and stiffness matrices of the mistuned system are thus reduced to the following form

$$\begin{aligned}\mathbf{M}^{\mathrm{red}}&=\mathbf{M}^{\mathrm{PRI}}+\boldsymbol{\Phi}^{\mathrm{PRI}^{\mathrm{T}}}\mathbf{M}^{\delta}\boldsymbol{\Phi}^{\mathrm{PRI}},\\ \bar{\mathbf{K}}^{\mathrm{red}}&=\bar{\mathbf{K}}^{\mathrm{PRI}}+\boldsymbol{\Phi}^{\mathrm{PRI}^{\mathrm{T}}}\bar{\mathbf{K}}^{\delta}\boldsymbol{\Phi}^{\mathrm{PRI}}.\end{aligned} \tag{4.17}$$

The above formulation is acceptable in terms of accuracy. However, in the context of statistical analyses, re-constructing the ROM for multiple small mistuning patterns, based the approach of direct projection, can result in prohibitively high computational cost. Instead, NEWT strategically selects a subset of cyclic mode pairs for the pristine and each of the rogue sectors to form the projection basis for model reduction. The mode selection process is based on the criteria proposed by Fitzner et al. [17], following the fact that within the same mode family, cyclic modes associated with higher nodal diameters share similar shapes and can be mutually dependent on each other. And thus most of the cyclic modes of higher nodal diameters can be removed from the projection basis, whereas the rest of cyclic modes remain spanning the full modal space. This mode selection criterion results in a projection basis that is much smaller in size than the PRIME basis. To integrate the NEWT method into the PRIME frame, the PRIME mode basis is expressed as linear combinations of the cyclic modes selected following the NEWT criteria. The projection process from the PRIME mode basis to the cyclic mode basis for the j^{th} sector possesses either of the following two forms

$$\begin{aligned}\boldsymbol{\Phi}_j^{\mathrm{P}}&=\mathbf{A}^{\mathrm{P}}\mathbf{q}_j^{\mathrm{P}}+\mathbf{B}^{\mathrm{P}}\mathbf{r}_j^{\mathrm{P}},\\ \boldsymbol{\Phi}_j^{\mathrm{R}}&=\mathbf{A}_j^{\mathrm{R}}\mathbf{q}_j^{\mathrm{R}}+\mathbf{B}_j^{\mathrm{R}}\mathbf{r}_j^{\mathrm{R}}.\end{aligned} \tag{4.18}$$

If the j^{th} sector of the blisk-damper system is pristine, $\mathbf{A}^{\text{P}}$ and $\mathbf{B}^{\text{P}}$ contain the cyclic mode pairs of a pristine sector, and the modal participation factors $\mathbf{q}_j^{\text{P}}$ and $\mathbf{r}_j^{\text{P}}$ represent the contribution of the pristine cyclic mode pairs to the mode shapes of the j^{th} sector in the PRIME mode basis. Similarly, if the j^{th} sector is rogue, $\mathbf{A}_j^{\text{R}}$ and $\mathbf{B}_j^{\text{R}}$ contain the cyclic mode pairs of the rogue sector. The modal participation factors $\mathbf{q}_j^{\text{R}}$ and $\mathbf{r}_j^{\text{R}}$ represent the contribution of the rogue cyclic mode pairs to the mode shapes of the j^{th} sector in the PRIME mode basis.

Note that the above projection involves expanding cyclic mode pairs to a specific sector. This process requires adjusting the phase angle based on the sector index as well as the nodal diameter (or harmonic index). Such adjustment is implicitly carried by the participation factors, and indicated by their subscripts j = sector number. Substituting Eqn. (4.18) into Eqn. (4.16) results in the following ROM matrices

$$\begin{aligned}\mathbf{M}^{\text{red}} &= \mathbf{M}^{\text{PRI}} + \sum_{j=1}^{N} (\mathbf{A}_j \mathbf{q}_j + \mathbf{B}_j \mathbf{r}_j)^{\text{T}} \mathbf{M}_j^{\delta} (\mathbf{A}_j \mathbf{q}_j + \mathbf{B}_j \mathbf{r}_j), \\ \bar{\mathbf{K}}^{\text{red}} &= \bar{\mathbf{K}}^{\text{PRI}} + \sum_{j=1}^{N} (\mathbf{A}_j \mathbf{q}_j + \mathbf{B}_j \mathbf{r}_j)^{\text{T}} \bar{\mathbf{K}}_j^{\delta} (\mathbf{A}_j \mathbf{q}_j + \mathbf{B}_j \mathbf{r}_j),\end{aligned} \tag{4.19}$$

where $\mathbf{M}_j^{\delta}$ and $\bar{\mathbf{K}}_j^{\delta}$ are the mistuning components of the j^{th} sector. $\mathbf{A}_j$ and $\mathbf{B}_j$ represent the cyclic mode pairs of the j^{th} sector, which are selected from either $\mathbf{A}^{\text{P}}$ and $\mathbf{B}^{\text{P}}$, or $\mathbf{A}_j^{\text{R}}$ and $\mathbf{B}_j^{\text{R}}$, depending on whether the j^{th} sector is a pristine or one of the rogue sectors. $\mathbf{q}_j$ and $\mathbf{r}_j$ are the corresponding participation factors of the j^{th} sector.

Note that the contribution of cyclic mode pairs to the interface mode shapes $\mathbf{\Phi}^{\text{I}}$ in the PRIME mode basis is neglected in formulating the ROM for small mistuning. All interface DOFs are located on the disk component, which is significantly more rigid than the blade components. Small mistuning on the disk component can rarely result in noticeable changes in the free and forced responses of the blisk-damper system. Thus, it is assumed that small mistuning does not exist on the interface components. Consequently, the projection of the mistuning components onto the interface mode shapes of the PRIME basis can be omitted. Note that the projection of the mistuning components in the above equation is formulated as a sum of sector-level projections over a number of N sectors. The free response problem in the PRIME modal domain can be expressed as

$$[-\omega^2 \mathbf{M}^{\text{red}} + \bar{\mathbf{K}}^{\text{red}}] \mathbf{p}^{\text{PRI}} = \mathbf{0}, \tag{4.20}$$

and the normal mode shapes of the mistuned system can be extracted based on the following

transformation

$$\mathbf{\Phi} = \mathbf{\Phi}^{\mathrm{PRI}}\mathbf{p}^{\mathrm{PRI}}. \tag{4.21}$$

Thus, for each of the two global contact status, a PRIME mode basis can be formed, denoted as $\mathbf{\Phi}_{sl}^{\mathrm{PRI}}$ and $\mathbf{\Phi}_{st}^{\mathrm{PRI}}$. With the PRIME mode bases that serve as the input parameters to the N-PRIME method, the mode shapes $\mathbf{\Phi}_{sl}$ and $\mathbf{\Phi}_{st}$ of a mistuned system can be computed. Thus, the transformation expressed by Eqn. (4.9) can be written as

$$\mathbf{x}^{(n)} = \begin{bmatrix}\mathbf{\Phi}_{st} & \mathbf{\Phi}_{sl}\end{bmatrix}\mathbf{q}^{(n)} = \begin{bmatrix}\mathbf{\Phi}_{st}^{\mathrm{PRI}}\mathbf{p}_{st}^{\mathrm{PRI}} & \mathbf{\Phi}_{sl}^{\mathrm{PRI}}\mathbf{p}_{sl}^{\mathrm{PRI}}\end{bmatrix}\mathbf{q}^{(n)}. \tag{4.22}$$

The mode shapes contained by the two PRIME bases are assembled from sector-level mode shapes. Thus, the above transformation, as well as the projection of Eqn. (4.3) onto the modal domain, involves only sector-level computations. By integrating N-PRIME into the CoRiD method, a novel reduced-order modeling technique is developed for frictionally damped blisks with simultaneous large and small mistuning.

4.3 Results and Validation

As mentioned previously, the ring dampers are held in contact with the blisk by pre-stress, such as centrifugal loading. Depending on the amplitude of the pre-stress, as well as the geometry of the damper, the initial normal load acting on the contact surfaces varies from node to node, and may result in separation at certain contact node pairs. To determine the initial normal load at each contact node, and the resulted deformation, an iterative static analysis is performed for the given pre-stress. Moreover, Eqn. (4.10) represents a compact ROM, and consists of a small set of modal complex algebraic equations, in the frequency domain. However, the nonlinear contact forces $\mathbf{F}_{nl}^{(n)}$ must be first computed in the time domain. Thus, the hybrid frequency/domain method, originally introduced by Guillen [45], is adopted in this study to solve Eqn. (4.10). Both iterative solution processes of determining the static deformation resulting from pre-stress, and the nonlinear forced responses computed by HFT, are detailed in Sec. 3.2.4. With the solution methods established, the PRIME-CoRiD method is applied to obtain the forced responses of the UM Validation Blisk shown in Fig. 3.1.

4.3.1 Forced Response Analyses

In this section, forced responses are computed for the blisk-damper system with two mistuning patterns. Validations against finite element analyses on the full-order system are computationally prohibitive. Instead, the results provided by the ROM are validated against the forced response analyses performed on a condensed CB-CMS model provided by ANSYS. To minimize the error between the validation data generated by the CB-CMS model and the full-order model (so that it is negligible), 100 system normal modes with fixed CMS interfaces are included in the CB-CMS mode basis, enough to ensure the accuracy of the CB-CMS model for forced response analyses performed within the forcing frequency range of interest.

A traveling wave excitation is used in this study as the external periodic forcing function, which can be expressed as follows

$$\mathrm{f} = \sum_{j=1}^{N} \mathbf{F}_j \mathrm{e}^{-i(j-1)\mathrm{EO}\frac{2\pi}{N}}, \tag{4.23}$$

where $\mathbf{F}_j$ is the amplitude of the excitation applied on the j^{th} sector. Note that a traveling wave excitation is a function of the engine order EO. Responses under excitations of lower engine orders exhibit disk-dominated behavior, where significant relative motions are observed between the ring damper and the blisk, and the frictional damping is most effective in dissipating energies. However in this case, the blade mistuning has little or no effect on the forced responses since little or no motion is present on the blades. In contrast, under excitations of higher engine orders, the effect of blade mistuning is stronger, whereas the frictional damping becomes ineffective. Thus, to ensure both blade mistuning and frictional damping are effective so that their correlation can be observed, an excitation of engine order 3 is selected, as this intermediate engine order results in motions distributed throughout the blisk. The traveling wave excitation is applied at the tip of each blade to ensure a large blade deformation. Forced responses are extracted at one selected node per blade, referred to as the response nodes, that are in proximity with the nodes on which the excitations are applied. A small Rayleigh damping ratio is chosen as $\alpha = 0$, and $\beta = 4.4396 \times 10^{-7}\, s$, which corresponds to a damping ratio $\zeta = 4.0622 \times 10^{-4}$ at $\omega_n = 1,830\, Hz$.

It it well known that in predicting the responses of complex systems, better accuracy can be achieved with more harmonics added to the HBM formulation. For the simple academic model, a single harmonic is sufficient to capture the correct responses, and test cases reveal that adding more harmonics results in unnoticeable improvements to the accuracy of the ROM-predicted responses. Thus, in this study a single harmonic is used.

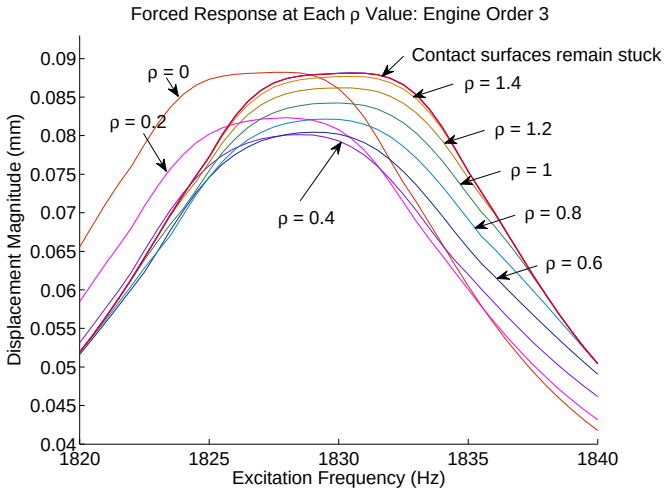

Figure 4.4: Forced responses of a UM validation blisk with large mistuning under a traveling wave excitation of engine order 3

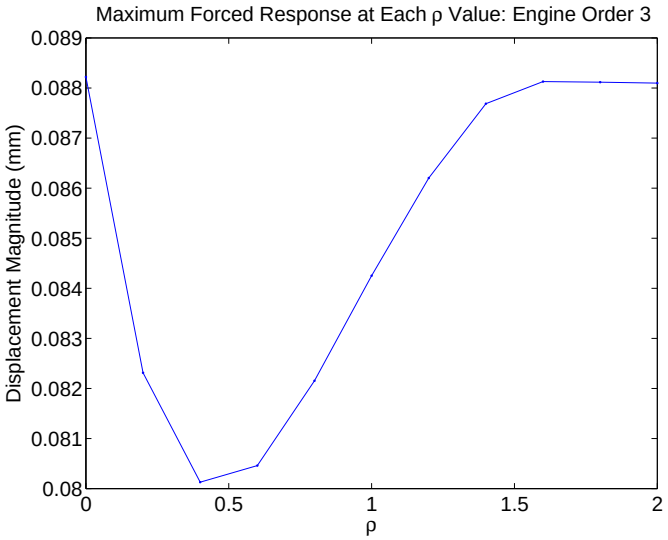

Figure 4.5: Maximum forced responses within the range of excitation frequencies at each ratio ρ of a UM validation blisk with large mistuning under a traveling wave excitation of engine order 3

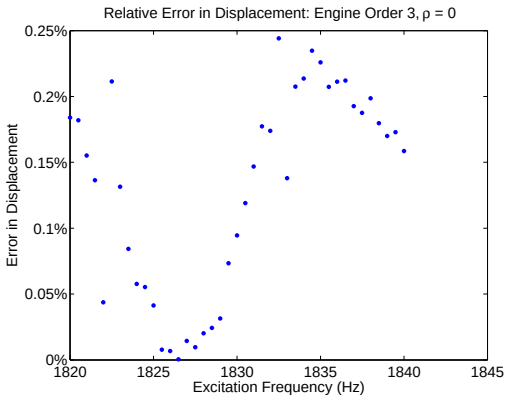

(a) Error in forced responses at $\rho = 0$

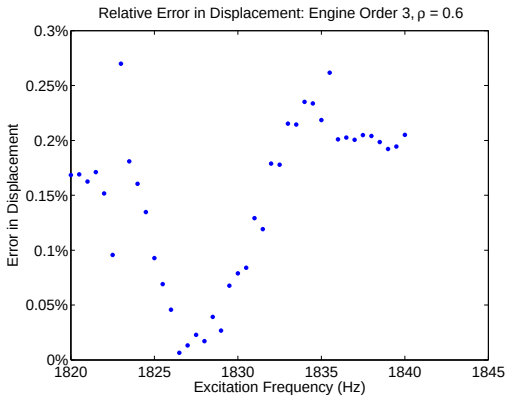

(b) Error in forced responses at $\rho = 0.6$

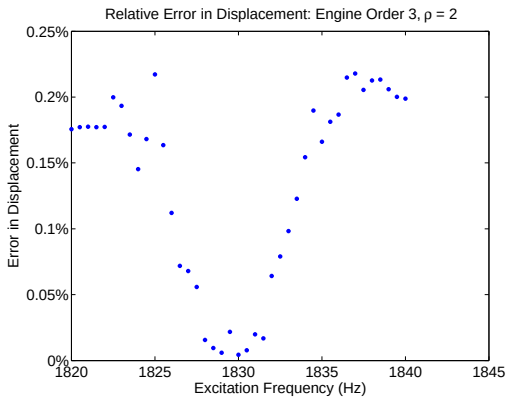

(c) Error in forced responses at $\rho = 2$

Figure 4.6: Error in forced responses of a UM validation blisk with large mistuning under a traveling wave excitation of engine order 3, validated at ρ values of 0, 0.6, and 2

The first example includes the forced responses performed on a blisk-damper system with large mistuning only, where 10% material is removed from one of the blades, as shown in Fig. 4.10a. To evaluate the relative importance and effects of the pre-stress magnitude N_0, forcing magnitude F, and the coefficient of friction μ, the ratio $\rho = \frac{\mu N_0}{F}$ is used in this study. The maximum amplitude of forced responses across all response nodes are extracted at each excitation frequency, from 1,820 to 1,840 Hz, and each ρ value, ranging from 0 to 2, as shown in Fig. 4.4. A more clear view is shown in Fig. 4.5 by extracting the maximum forced response amplitude within the range of forcing frequencies at each ρ value. At $\rho = 0$, the contact surfaces are frictionless and can freely slide relative to each other. Thus, no energy dissipation by frictional damping occurs, and a maximum response is observed. As the friction coefficient increases, so does the effectiveness of frictional damping, resulting in a lower response. A maximum reduction in the forced response amplitude occurs at $\rho = 0.4$. As the friction coefficient continues increasing, and ρ increases (approaching 2), it becomes difficult for the contact surfaces to slide against each other, leading to less effective frictional damping and a higher amplitude of forced responses. The ROM-predicted results are validated at three values of ρ: $\rho = 0$, 0.6, and 2. The relative errors between the ROM results and the validation data provided by the ANSYS CB-CMS model are shown in Fig. 4.6. The maximum relative error occurs at $\rho = 0.6$, and is approximately 0.27% (Fig. 4.6b). Such a small error indicates a good accuracy of the ROM when modeling large mistuning. Also, it shows that the contact dynamics is well captured by the mode basis involved in the stick-slip modal transformation.

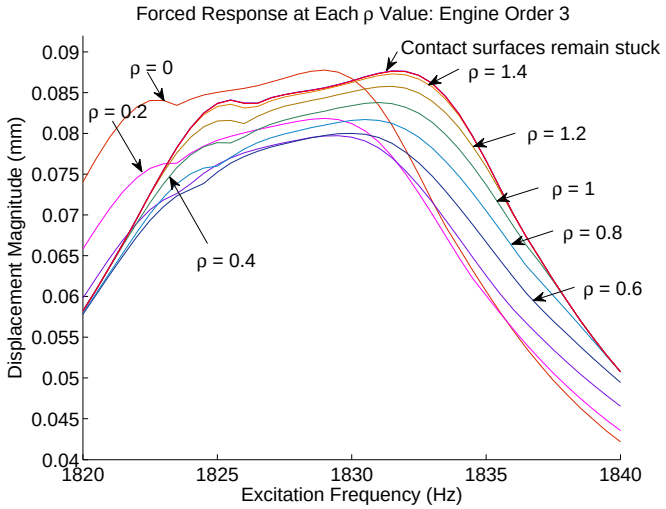

Figure 4.7: Forced responses of a UM validation blisk with both large and small mistuning under a traveling wave excitation of engine order 3

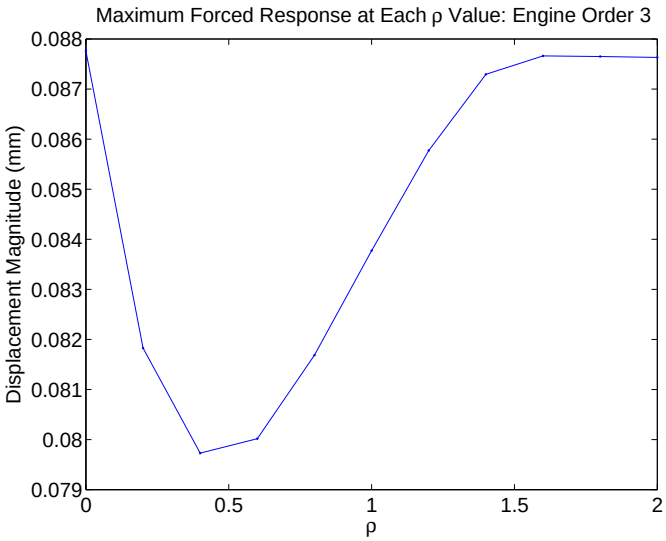

Figure 4.8: Maximum forced responses within the range of excitation frequencies at each ratio ρ of a UM validation blisk with both large and small mistuning under a traveling wave excitation of engine order 3

In the second example, in addition to the damaged blade, small perturbations in material property are applied to all blades by varying their Young's modulus by a small percentage from their nominal value. Such variations are randomly determined following a normal probability distribution of a zero mean value and a 2% standard deviation, resembling a small mistuning pattern that typically results from manufacturing tolerances. The ROM-predicted forced responses under a traveling wave excitation of engine order 3 are shown in Fig. 4.7. The maximum forced responses within the range of forcing frequencies at each friction coefficient are shown in Fig. 4.8. It is observed that the added small mistuning pattern has little influence on the effectiveness of the frictional damping, as the maximum reduction of forced response amplitude remains at $\rho = 0.4$. Interestingly, validation against the CB-CMS model indicates that the maximum relative error occurs at $\rho = 0$, and is approximately 0.15% (Fig. 4.9a), lower than the value observed in the case where only large mistuning exists. This small error indicates that an upper bound of error is set by the PRIME-CoRiD method when solving large mistuning problems, and little or no additional error is introduced by NEWT for modeling small mistuning.

4.3.2 Statistical Analyses

Recall that all computations required by the PRIME-CoRiD method are sector-level, resulting in fast construction of ROMs of mistuned blisk-damper systems. Moreover, if a

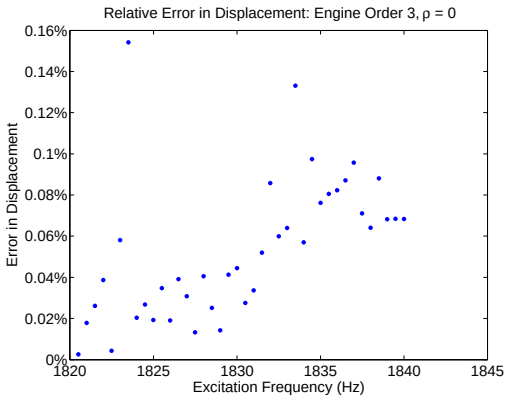

(a) Error in forced responses at $\rho = 0$

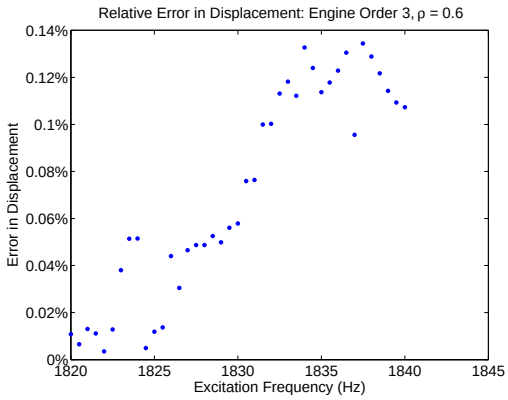

(b) Error in forced responses at $\rho = 0.6$

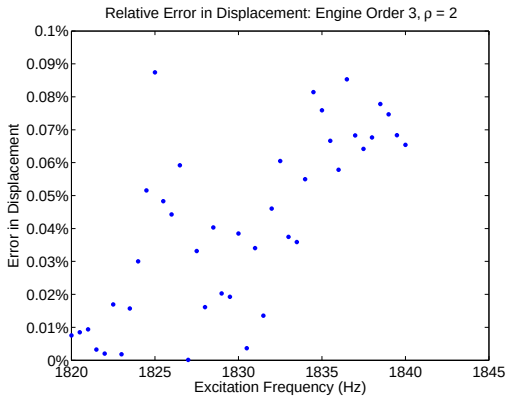

(c) Error in forced responses at $\rho = 2$

Figure 4.9: Error in forced responses of a UM validation blisk with both large and small mistuning under a traveling wave excitation of engine order 3, validated at ρ values of 0, 0.6, and 2

(a) 10% tip (b) 14% tip (c) 8% edge

Figure 4.10: Examples of rogue sectors with different volume of material removed from different locations on the blade component

single harmonic is used in the HBM formulation, the size of the resulting ROM depends only on the number of (a few) modal coordinates used in the stick-slip modal transformation. Thus, minimal computational effort is required to compute forced responses by the HFT method. For a mistuned blisk-damper system excited under external forcing at a specified forcing frequency, the PRIME-CoRiD requires only 3-5 minutes of CPU time to compute its forced responses for all DOFs of the system. In contrast, the transient analysis performed on a full-order finite element model of the blisk-damper system requires more than 5 days of CPU time for the solution to reach steady state. Due to the fast computations and good accuracy provided by the PRIME-CoRiD method, it is possible to sample a blisk-damper system over a large amount of simultaneous large and small mistuning patterns to obtain its statistical characteristics and to study the correlation between random mistuning and the effectiveness of frictional ring dampers. In this study, a Monte-Carlo analysis is applied to the UM Validation Blisk, with 400 samples of small and large mistuning patterns included. The mistuning patterns are created as follows

1. Large mistuning patterns are created by randomly selecting 1 or 2 sectors as rogue sectors. Each of the rogue sectors has distinct volume of material removed from its blade component. Examples of rogue sectors are shown in Fig. 4.10. In this study, 10 large mistuning patterns are involved.

2. Each large mistuning pattern is associated with 40 different small mistuning patterns. The small mistuning patterns are created through the same process introduced in the previous section. Variations in Young's modulus are applied to each blade. A random number generator is implemented to provide the variations following a normal probability distribution of a zero mean value and a 2% standard deviation.

A traveling wave excitation of engine order 3 is adopted in this study so that the effects of both blade mistuning and frictional damping are present. It is well known that mistun-

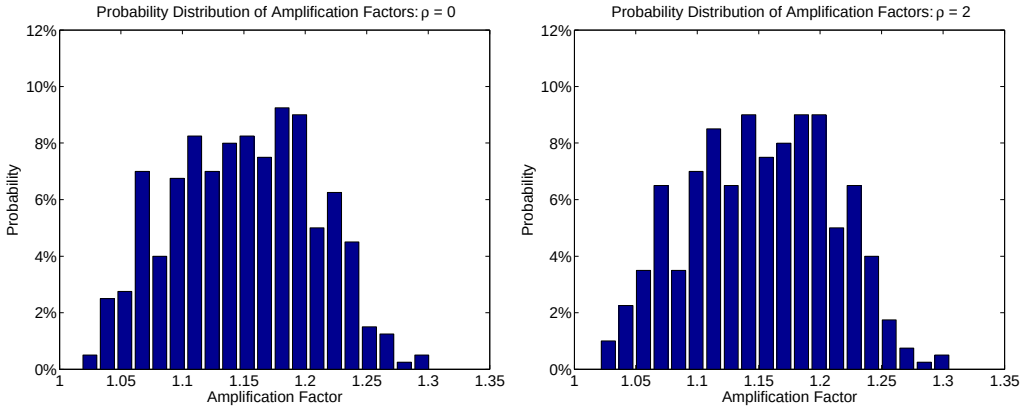

(a) $\rho = 0$ (b) $\rho = 2$

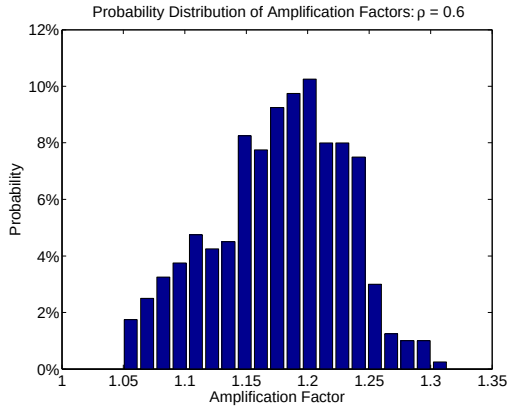

(c) $\rho = 0.6$

Figure 4.11: Probability distributions of amplification factors of forced responses of mistuned blisk-damper systems obtained at different ρ value

ing can lead to strain energy localization and drastically increase the amplitude of forced responses. Thus, it is useful to define a metric so that the effect of mistuning can be quantified. In this study, this metric is defined by comparing the maximum amplitude of forced response throughout the pre-selected response nodes of the mistuned system with that of a tuned system, under the same forcing conditions, with the same ρ value, and within the same range of forcing frequencies. This metric is called the amplification factor ($AF_x(\rho)$), and is defined as follows

$$AF_x(\rho) = \frac{\max_\omega(\max_{i=1}^{N_{node}}(\|\mathbf{x}_i^m(\rho)\|))}{\max_\omega(\max_{i=1}^{N_{node}}(\|\mathbf{x}_i^0(\rho)\|))}, \tag{4.24}$$

where N_{node} is the number of response nodes, and ω is the angular forcing frequency. Superscript m stands for a mistuned system, whereas 0 stands for a tuned system. Note that

the amplification factor is computed for forced responses of mistuned and tuned systems with the same ρ value. Figure 4.11 shows the probability distributions of amplification factors for the forced responses of mistuned systems obtained from the Monte-Carlo analyses. The analyses are performed for three values of ρ: $\rho = 0, 0.6$, and 2. Note that in the cases of $\rho = 0$ or 2, (Fig. 4.11a, and 4.11b), the contact surfaces maintain a sliding or sticking condition, respectively. A side-by-side comparison shows that similar probability distributions are observed in these two linear cases. A frictional contact surface with $\rho = 0.6$ results in amplification factors which are more centered toward the mean value of 1.18 (Fig. 4.11c). However, the maximum amplification factor is not influenced by the friction damping, and is approximately 1.33 for all three cases.

The probability distribution of amplification factors reveals that frictional damping has a small influence on the amplification of forced responses caused by blade mistuning. However, the correlation between mistuning and friction damping is mutual, and the analysis cannot be conclusive without studying the effect of mistuning on the effectiveness of friction damping. This effect can be measured by the reduction ratio ($RR_x(\rho)$), representing the maximum percentage reduction in forced response amplitude due to frictional damping, expressed as the following

$$RR_x(\rho) = 1 - \frac{\max_\omega(\max_{i=1}^{N_{node}}(\|\mathbf{x}_i^m(\rho)\|))}{\max_\omega(\max_{i=1}^{N_{node}}(\|\mathbf{x}_i^m(0)\|))}. \tag{4.25}$$

In this study, the value of ρ is selected as 0.6. Figure 4.12 shows the reduction ratio of forced responses, sorted from the lowest to the highest value, for the UM Validation Blisk with each of the mistuning patterns involved in the Monte-Carlo analyses. It is observed that the reduction ratios spread over a wide range from 8% to 15.2%. This range cannot be estimated based on analyzing a tuned system, with a reduction ratio of approximately 13%, that is neither a mean nor a median value of all the samples. Such results emphasize the value of the PRIME-CoRiD method in efficiently predicting the effectiveness of a damper design, especially for mistuned systems, through statistical analyses.

4.4 Conclusion

A novel reduced-order modeling technique, referred to as the PRIME-CoRiD method, is proposed and presented in this paper. This method is capable of predicting the nonlinear forced responses of bladed disks with frictional ring dampers, and random large and small mistuning patterns. This method has the following attractive features.

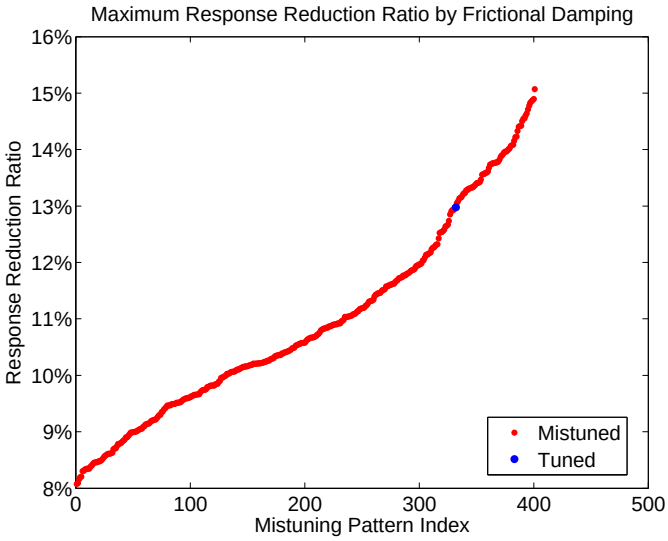

Figure 4.12: Ratio of reduction of forced response amplitudes resulted from frictional damping, extracted for a tuned and each of the 400 mistuned systems

1. The PRIME-CoRiD method forms a mode basis that contains the system normal mode shapes of a blisk-damper system that undergoes global sliding and sticking conditions. This mode basis can accurately capture the nonlinear behavior of the contact surfaces. By projecting the blisk-damper system onto this mode basis through stick-slip modal transformation, its size is reduced from the level of the full-order FE model that contains many DOFs, to a few modal coordinates.

2. The mode shapes contained by this mode basis are obtained through the N-PRIME method, which is specialized in computing free and forced responses of bladed disks with simultaneous large and small mistuning. The N-PRIME method uses only sector-level cyclic mode shapes as the input parameters, and all computations required by N-PRIME are performed on a sector level. Thus, the computational effort required to form the mode basis of the stick-slip modal transformation is minimal.

3. Due to the compactness of the ROM, and the minimal computational cost required to form it, nonlinear forced response analyses performed on the PRIME-CoRiD ROM through the HFT method is fast and efficient. This enables PRIME-CoRiD to be used for Monte-Carlo analyses, for the first time, to study the mutual influence between random large and small mistuning and the effectiveness of ring dampers.

The PRIME-CoRiD method is applied to the UM Validation Blisk with two different mistuning patterns. The results indicate that the method has very good accuracy in predicting the nonlinear forced responses of mistuned blisk-damper systems. A statistical analysis

reveals a wide range of effectiveness of the friction ring damper when the blisk suffers from different mistuning patterns. Since the upper and lower bounds of the effectiveness cannot be simply estimated based on the forced responses of a tuned system, the results emphasize the unique usefulness of the PRIME-CoRiD method. Moreover, though ring dampers are selected as the damping source in this study, it does not indicate that the variety of damping sources that the PRIME-CoRiD method can model is restricted. One important area for future development is to extend the current PRIME-CoRiD method to applications that involve underplatform wedge dampers, frictional shroud contacts, and other types of frictional damping sources.

CHAPTER 5

Geometric Optimization of Dry Friction Ring Dampers for Maximized Reduction in Forced Responses

5.1 Introduction

The CoRiD and PRIME-CoRiD methods are powerful in accurately and efficiently capturing the nonlinear forced responses of blisk-damper systems. However, from a design perspective, the reduced-order methods alone cannot provide an optimal design of friction ring dampers. The effectiveness of ring dampers depend on a variety of parameters, including 1) contact parameters, such as contact stiffness, friction coefficient, and the level of pre-stress, 2) external forcing conditions, such as the location of forcing, and the forcing amplitude, and 3) geometry of the cross-section of the ring. Optimization of damper effectiveness has been carried out by many researchers. Conventional methods in predicting optimal damper design involves repetitive computations of nonlinear forced responses of blisk-damper systems with a few pre-selected sets of parameters. Such methods require tremendous amount of computational effort, and do not guarantee to involve the optimal sets of parameters.

To address this issue, direct parametric analyses have been adopted to facilitate in tracing the optimal of design parameters [60–64]. The optimization problem can be efficiently solved when the sensitivity characteristics of forced responses are determined. Unfortunately, direct parametric analyses imposes a restriction that no geometric changes are allowed during the optimization process. In practice, variations in each dimension of the damper geometry can result in significant changes in damper effectiveness. Thus, a ring damper with optimal geometry cannot be directly obtained through direct parametric analyses.

Figure 5.1 shows the UM Validation Blisk model used in this study, in contact with

a V-shaped ring damper. In this study, the geometry of the V-shaped damper is first parametrized following a volume constraint. A parametric study is performed by varying two of the geometric parameters simultaneously at a time to study the trade-offs among different dimensions of the damper geometry. Moreover, a series of sensitivity analyses are performed to reveal the optimal location that the damper should be placed upon to reach its maximum effectiveness. The effect of joints and changes in thickness are also explored. Based on the analyses conducted in this paper, a set of damper design guidelines are proposed.

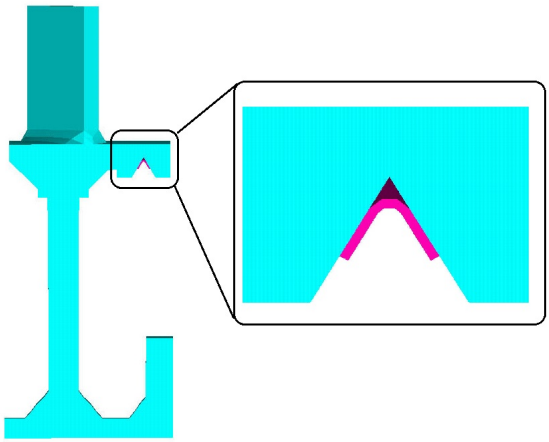

Figure 5.1: A typical blisk-damper system: UM validation blisk (blue) in contact with a V-shaped ring damper (purple)

5.2 Methodology

5.2.1 Damper Geometry Parametrization

Consider the V-shaped ring damper shown in Fig. 5.2. To create a deterministic geometry of the damper, the values of four parameters must be specified, including the length of the contact surface l, the opening angle of the groove θ, the damper thickness t, and the radius r from the center of the blisk to the groove depth. For a given blisk model, such as the academic model shown in Fig. 5.1, the distance from the center of the blisk to the rim is fixed. Since the groove is located underneath the rim, it is reasonable to specify r with a pre-set value. Thus, variations in r are not included as a parameter for optimization.

Moreover, the optimization of the damper geometry follows a volume constraint. In other words, during the optimization process, at least two of the remaining three geometric parameters, l, θ, and t, must vary simultaneously to keep the volume of the damper constant.

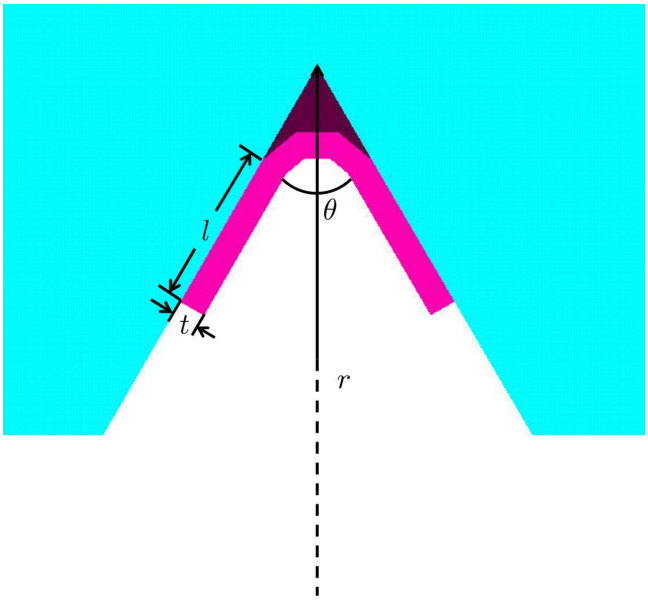

Figure 5.2: A V-shaped ring damper parametrized into four dimensions

Although this study focuses on a V-shaped ring damper, the parametrization process is not limited to such a single geometry. In general, for a ring damper with a generic shape of the cross-section, it is often feasible to identify the minimum number of parameters that are sufficient to construct the geometry of the damper. While some parameters are fixed due to certain geometric constraints imposed by the blisk model, the rest parameters can be included for optimization process following a volume constraint.

5.2.2 Coherent Ring Damper (CoRiD)

One of the widely-used metrics for evaluating the effectiveness of a friction damper is the maximum reduction in the nonlinear forced responses of the blisk-damper system. For a blisk in contact with the V-shaped damper with a specific set of geometric parameters, its responses under external excitation is computed by the CoRiD method [68, 69]. The formulation of the CoRiD method is reviewed in this section.

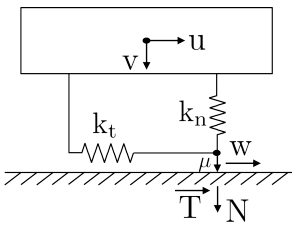

Figure 5.3: A 1D macro-slip model

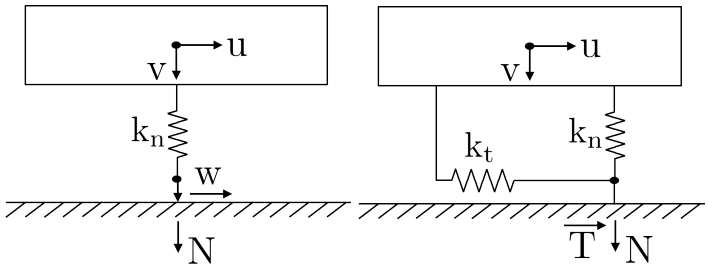

(a) Sliding condition (b) Sticking condition

Figure 5.4: Equivalent contact models of a node pair under two limiting contact statuses

Consider a typical blisk-damper model as shown in Fig. 5.1. Its EOMs can be expressed as

$$\mathbf{M}\ddot{\mathbf{x}}(t) + \beta\mathbf{K}\dot{\mathbf{x}}(t) + \mathbf{K}\mathbf{x}(t) = \mathbf{F}_e(t) + \mathbf{F}_{nl}(t), \tag{5.1}$$

where $\mathbf{M}$ and $\mathbf{K}$ are the mass and stiffness matrices of the blisk-damper system, and β is the stiffness-proportional damping coefficient. $\mathbf{F}_e(t)$ represents the external periodic forcing function. $\mathbf{F}_{nl}(t)$ represents the nonlinear contact forces. To capture the nonlinear contact forces $\mathbf{F}_{nl}(t)$, the two mating contact surfaces between the blisk and the ring damper are discretized into evenly distributed contact node pairs. The 3D relative displacements, as well as contact forces, are decomposed into two perpendicular in-plane tangential directions, and an out-of-plane normal direction. By assuming the two tangential components of the relative displacements, as well as the resulting tangential contact forces, are independent of each other, the contact dynamics along each tangential direction can be modeled by a simple 1D macro-slip model with normal load variation [26], as shown in Fig. 5.3. This assumption has been extensively adopted and validated in many studies [51, 52, 65]. Thus, the 3D contact dynamics at each contact node pair can be modeled by a pair of independent 1D models.

Full-order FE models of commercial blisk-damper systems often contain many DOFs. Thus solving Eqn. (5.1) directly can be a formidable task. In order to reduce the size of the full-order model, two limiting contact conditions of the 1D macro-slip model are considered.

Consider two nodes of a contact node pair that can fully slide relative to each other. In this case, the contact force is constant, and the tangential contact stiffness between the two contact nodes is ineffective. An equivalent model is constructed by removing the tangential stiffness from the 1D macro-slip model, as shown in Fig. 5.4a. In contrast, two nodes of a contact node pair that are stuck together can be modeled as shown in Fig. 5.4b, where the

Coulomb slider is bonded to the contact surface, and no slip motion is allowed. A local contact stiffness matrix can be written for each of the two limiting contact models.

$$\mathbf{k}_{sl} = \begin{bmatrix} 0 & 0 & 0 \\ 0 & 0 & 0 \\ 0 & 0 & k_n \end{bmatrix}, \qquad \mathbf{k}_{st} = \begin{bmatrix} k_t & 0 & 0 \\ 0 & k_t & 0 \\ 0 & 0 & k_n \end{bmatrix}. \tag{5.2}$$

Note that the contact stiffness matrices for each contact node pair are expressed in local contact coordinates. Now consider a global contact status, where the two mating contact surfaces can fully slide relatively to each other. In this case, a global contact stiffness matrix $\mathbf{K}_{sl}$ can be assembled from $\mathbf{k}_{sl}$, and expressed in global (cylindrical) coordinate system, with proper rotation applied. Similarly, when the two contact surfaces are completely stuck together, a global contact stiffness matrix $\mathbf{K}_{st}$ can be assembled from the local contact stiffness matrix $\mathbf{k}_{st}$. Note that under both global sliding and sticking conditions, no nonlinear forces exist between the contact surfaces. Thus, a linear modal analysis can be performed for the blisk-damper system under each of the global contact status by solving the following eigenvalue problems

$$[-\omega_{sl}^2\mathbf{M} + (\mathbf{K} + \mathbf{K}_{sl})]\mathbf{\Phi}_{sl} = 0, \tag{5.3}$$

$$[-\omega_{st}^2\mathbf{M} + (\mathbf{K} + \mathbf{K}_{st})]\mathbf{\Phi}_{st} = 0, \tag{5.4}$$

where ω_{sl} and ω_{st} are natural frequencies of a blisk-damper system with global sliding and sticking conditions respectively enforced along the contact surfaces. $\mathbf{\Phi}_{sl}$ and $\mathbf{\Phi}_{st}$ contain the corresponding system normal mode shapes. Equation (5.1) can be projected onto a mode basis formed by $\mathbf{\Phi}_{sl}$ and $\mathbf{\Phi}_{st}$ by the following transformation

$$\mathbf{x}^{(n)} = \begin{bmatrix} \mathbf{\Phi}_{st} & \mathbf{\Phi}_{sl} \end{bmatrix} \mathbf{q}^{(n)} = \mathbf{T}\mathbf{q}^{(n)}. \tag{5.5}$$

Since the motion along the contact DOFs of $\mathbf{\Phi}_{sl}$ and $\mathbf{\Phi}_{st}$ represents the contact dynamics in two limiting cases: no sliding motion allowed, and free sliding, the contact dynamics of a blisk-damper system with frictional contact can be considered an intermediate state with only a limited level of sliding allowed. Such sliding motion is well captured by the difference between contact DOFs of $\mathbf{\Phi}_{sl}$ and $\mathbf{\Phi}_{st}$. Thus, the forced responses of a frictionally damped system can be approximated as a linear combination of the normal mode shapes of the same system under global sliding and sticking conditions ($\mathbf{\Phi}_{sl}$ and $\mathbf{\Phi}_{st}$).

The modal equation of motion resulting from the stick-slip modal transformation can

be expressed as

$$\mathbf{m}\ddot{\mathbf{q}}(t) + \beta\mathbf{k}\dot{\mathbf{q}}(t) + \mathbf{k}\mathbf{q}(t) = \mathbf{f}_e(t) + \mathbf{f}_{nl}(t), \tag{5.6}$$

where $\mathbf{m} = \mathbf{T}^T\mathbf{M}\mathbf{T}$, $\mathbf{k} = \mathbf{T}^T\mathbf{K}\mathbf{T}$, $\mathbf{f}_e = \mathbf{T}^T\mathbf{F}_e$, and $\mathbf{f}_{nl} = \mathbf{T}^T\mathbf{F}_{nl}$.

The ROM resulting from the stick-slip modal transformation does not possess any physical DOFs, and its size depends only on the number of mode shapes involved in the transformation basis. Thus, this ROM resembles a compact system.

Note that Eqn. (5.6) is expressed in the time domain. Conventional method such as the direct numerical time integration requires a large amount of iterations to obtain the steady state solution. Thus, the classical harmonic balance formulation is introduced to transform Eqn. (5.6) into the frequency domain by expressing each variable ($\mathbf{q}$, $\mathbf{f}_e$, and $\mathbf{f}_{nl}$) as a truncated sum of harmonic terms. And the resulting EOM in the frequency domain can be written as

$$\mathbf{d}^{(n)}\mathbf{q}^{(n)} = \mathbf{f}_e^{(n)} + \mathbf{f}_{nl}^{(n)}. \tag{5.7}$$

where $\mathbf{q}^{(n)}$ is the n^{th} order harmonic of the vector of modal displacement, and $\mathbf{d}^{(n)}$ is the n^{th} order harmonic of the modal dynamic stiffness matrix, expressed as

$$\mathbf{d}^{(n)} = -(n\omega)^2\mathbf{m} + (1 + i\beta n\omega)\mathbf{k}. \tag{5.8}$$

Equation (5.7) represents a compact frequency domain equation. However, the nonlinear contact forces must be evaluated in the time domain. Thus, the HFT method is adopted in this study to solve Eqn. (5.7). Detailed iterative solution process can be found in Ref. [46,68,69]. With the HFT method, the nonlinear forced responses of the blisk-damper system, with a provided set of damper dimensions, can be obtained.

5.3 Results and Discussion

5.3.1 Parametric Study of Geometric Variations

In this study, 28 V-shaped dampers are created by varying either the length of contact area from 3 to 6 *mm*, or the opening angle of the V-groove from $\frac{\pi}{3}$ to $\frac{5\pi}{6}$. The thickness of the dampers are adjusted accordingly to maintain the volume constraint. Several examples of the V-shaped dampers are shown in Fig. 5.5. Nonlinear forced responses are extracted at the tip of the blades for each of the 28 blisk-damper models. A traveling wave excitation is

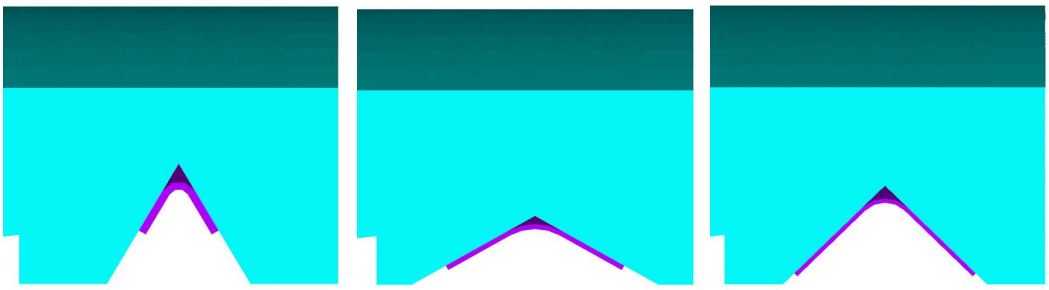

(a) $l = 3$, $\theta = \frac{\pi}{6}$ (b) $l = 4.5$, $\theta = \frac{\pi}{3}$ (c) $l = 6$, $\theta = \frac{\pi}{4}$

Figure 5.5: Examples of V-shaped dampers with various lengths of contact area and opening angles of the groove

used as the external periodic forcing function, which can be expressed as follows

$$\mathrm{f} = \sum_{j=1}^{N} \mathbf{F} \mathrm{e}^{-i(j-1)\mathrm{EO}\frac{2\pi}{N}}, \tag{5.9}$$

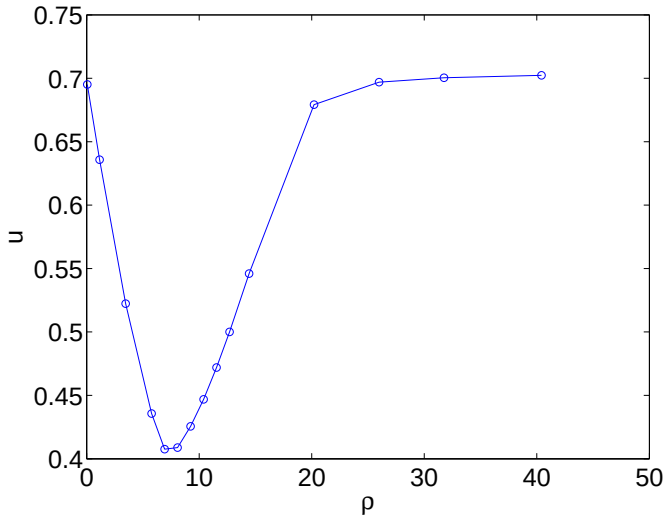

Figure 5.6: Forced responses of a UM validation blisk in contact with a typical V-shaped damper under a traveling wave excitation

As an example, Figure 5.6 shows the forced responses of a blisk-damper systems. The damper geometry is shown in Fig. 5.5b, which has a length of contact area of 4.5 *mm*, and an opening angle of $\frac{\pi}{3}$. To comprehensively evaluate the relative importance among the pre-stress magnitude N_0, forcing magnitude F, and the coefficient of friction μ, the ratio $\rho = \frac{\mu N_0}{F}$ is used in this study. Also, to account for the variations of damper effectiveness due to external forcing, the forced response magnitude x is normalized with respect to the

external forcing magnitude F. Thus, the normalized response magnitude $u = \frac{x}{F}$ is used in this study. The maximum response amplitude within the range of excitation frequency is extracted at each ρ value, ranging from 0 to 40. The effectiveness of a damper is often evaluated by the reduction ratio of forced responses R from the maximum value, typically when the damper is full sliding or completely stuck with the blisk, to the minimum response where the friction damping is most effective. Moreover, from a design perspective, a damper is often required to be effective over a wide range of frictional coefficients, or under different forcing conditions. This requirement is reflected in Fig. 5.6 as to maintain the reduction ratio above certain threshold over a wide range of ρ values, referred hereafter as the effective range of ρ. In this study, the two metrics, reduction ratio R and the effective range of ρ, are used to evaluate damper performance.

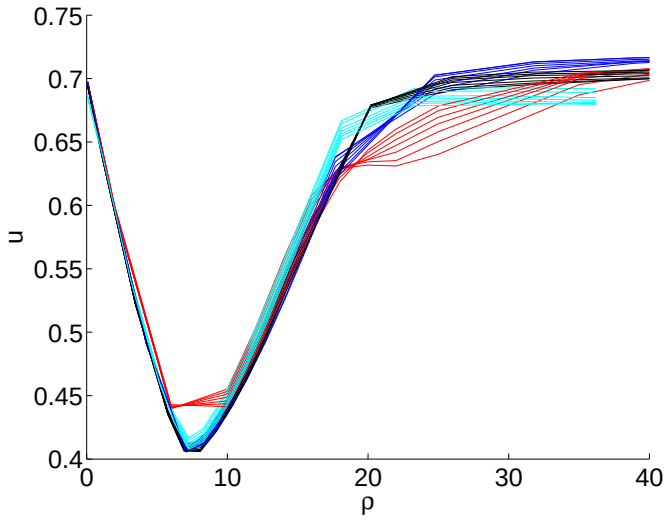

Figure 5.7: Forced responses of a UM validation blisk in contact with 28 V-shaped dampers of different variations in geometric parameters

Figure 5.7 shows the nonlinear responses of 28 blisk-damper systems. Surprisingly, the forced responses of all 28 models are almost identical to each other, with the same reduction ratio and the same effective range of ρ. This observation indicates that small variations of damper geometry has little or no effect on the damper effectiveness. Thus, it is of interest to explore the aspects of damper geometry that control damper effectiveness. A cone-shaped damper is created as shown in Fig. 5.8a, which possess half of the contact area compared with a V-shaped damper (Fig. 5.8b). It is expected that under the same forcing condition, the cone-shaped damper should reach at least half of the reduction ratio that a V-shaped damper provides.

However, Figure 5.9a shows that the cone-shaped damper has a reduction ratio of

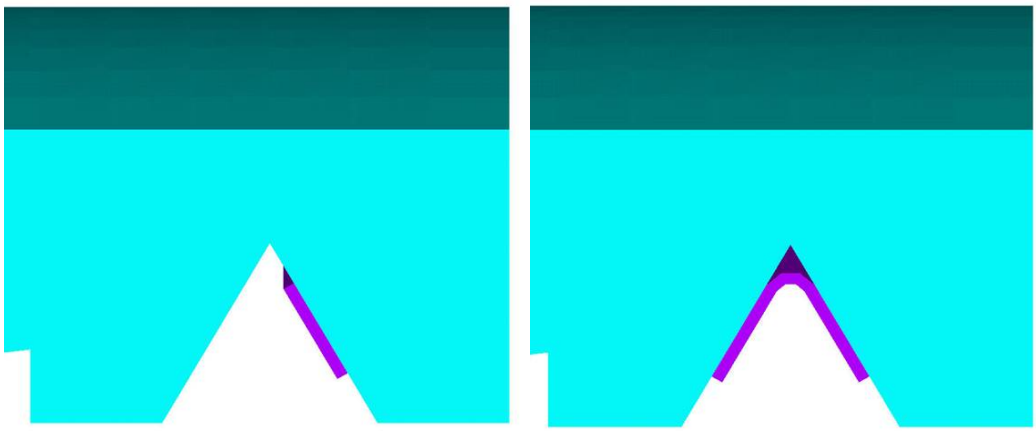

(a) A cone-shaped damper (b) A V-shaped damper

Figure 5.8: A cone-shaped damper that has half contact area of a V-shaped damper

	Sliding Frequency (Hz)	Sticking Frequency (Hz)	Frequency Split (Hz)
Cone-Shaped Damper	399.5890	399.6969	0.1079
V-Shaped Damper	399.0624	399.6754	0.6130

Table 5.1: Natural frequencies of a UM Validation Blisk in contact with a cone-shaped and a V-shaped damper

19.46%. Compared to the reduction ratio of 46.95% provided by the V-shaped damper (Fig. 5.9b), the cone-shaped damper fails to meet the expectation of reaching half of the effectiveness that the V-shaped damper provides. Moreover, the effective range of ρ values that the cone-shaped damper provides is 0.45, if the threshold of reduction ratio is set as 10%. This range is much narrower than the range of 24 that the V-shaped damper provides with the same threshold.

With the same forcing condition, and half of the contact area of the V-shaped damper, it is suspected that the ineffectiveness of the cone-shaped damper is due to the joint that the V-shaped damper possesses. The main contribution of the joint is additional bending stiffness along the tangential direction. Thus, the natural frequencies of the blisk-damper systems under sliding and sticking conditions are computed. Presented in Tab. 5.1 are the natural frequencies that fall into the range of excitation frequency. Note that while the sticking frequency remains the same for both cases, the sliding frequency has changed by approximately 0.5 Hz. This change leads to a larger difference between sliding and sticking frequencies, hereafter referred to as the frequency split, in the case of a V-shaped damper. It is believed that with a narrow frequency split, a small perturbation in excitation

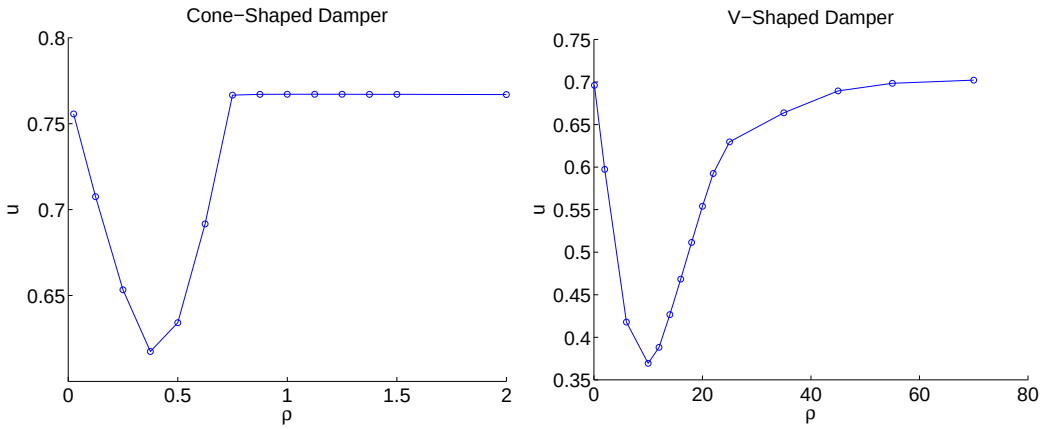

(a) A cone-shaped damper

(b) A V-shaped damper

Figure 5.9: Forced responses of a cone-shaped damper in comparison with the responses of a V-shaped damper that has twice the contact area

frequency can result in a sudden change of contact status of the entire contact surface from a sliding to a sticking condition. In contrast, a large frequency split provides more tolerance in perturbation in excitation frequency, and allows more micro-slip to occur. To prove this point, a double cone-shaped damper is created as shown in Fig. 5.10, and its Young's modulus is tuned to increase its bending stiffness so that its frequency split matches that of the V-shaped damper, as shown in Tab. 5.2.

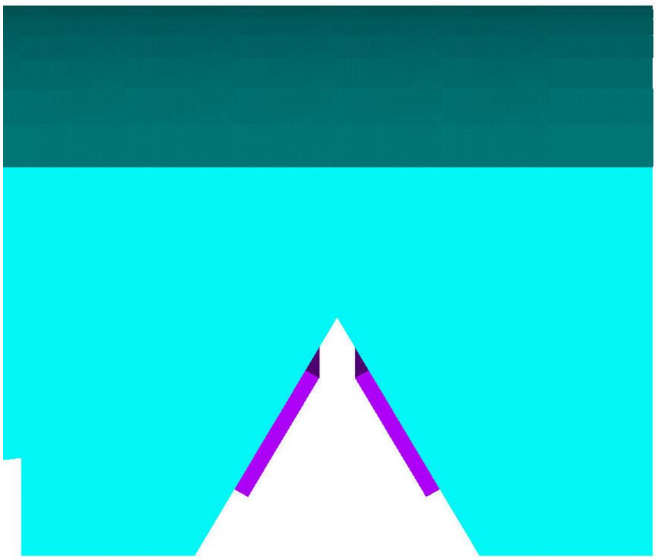

Figure 5.10: A double cone-shaped damper

Forced response analyses reveal that the double cone-shaped damper and the V-shaped

	Sliding Frequency (Hz)	Sticking Frequency (Hz)	Frequency Split (Hz)
Double Cone-Shaped Damper	399.3131	399.9290	0.6159
V-Shaped Damper	399.0624	399.6754	0.6130

Table 5.2: Natural frequencies of a UM Validation Blisk in contact with a double cone-shaped and a V-shaped damper

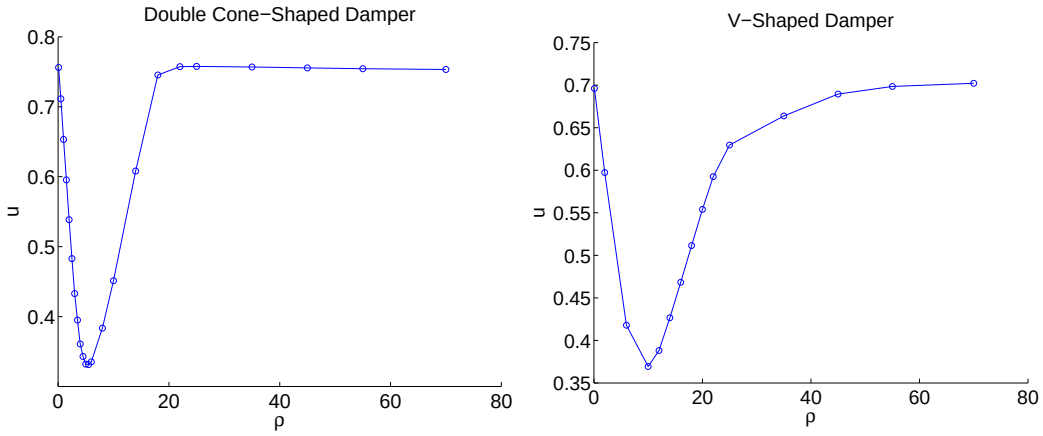

(a) A double cone-shaped damper

(b) A V-shaped damper

Figure 5.11: Forced responses of a double cone-shaped damper in comparison with the responses of a V-shaped damper that has twice the contact area

damper has similar reduction ratio of forced response amplitudes, as shown in Fig. 5.11. This observation is consistent with the statement that under the same forcing condition, the frequency split that damper provides determines its effectiveness. This is further confirmed by revisiting the frequency split provided by the 28 V-shaped damper models. It is revealed that all the 28 models have nearly identical frequency split of approximately 0.58 to 0.62 Hz.

5.3.2 Sensitivity Analyses

The observation that the frequency split provided by a friction ring damper determines its effectiveness is very impactful. It suggests that instead of time-consuming nonlinear analyses, a few harmonic analyses can fast predict whether a damper design is effective. Thus, in this section, a series of sensitivity analyses are performed to understand the relation between damper geometries and the frequency split. The results are further used to develop a systematical approach to increase the frequency split, as well as damper effectiveness, as

much as possible.

5.3.2.1 Location of Ring Dampers

With given geometry of the contact surface, the location which the damper is placed upon has certain effect on the interaction between the damper and the blisk, and thus affect the frequency split. To determine the optimal location for the damper, a sensitivity analysis is conducted by continuously applying circumferential elements of damping material along the contact surface, as shown in Fig. 5.12. Frequency split is computed with modal analyses performed after each time the material is added to the system, as shown in Fig. 5.13.

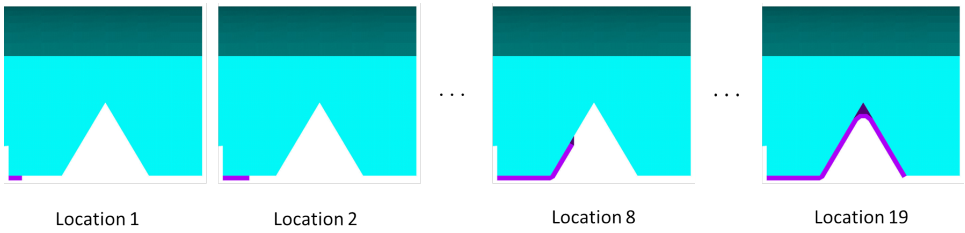

Figure 5.12: Models involved in the sensitivity analysis. Damper material is continuously added along the contact surface.

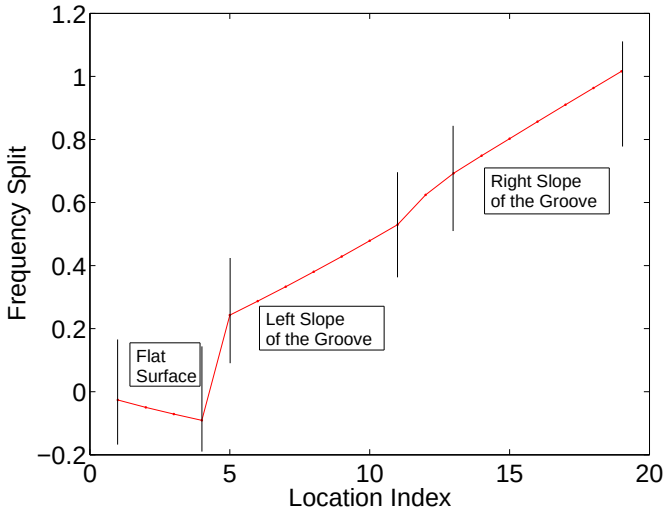

Figure 5.13: Frequency split resulted from continuously adding damper material along the contact surface

It is observed that adding damping material on the left slope of the groove is most influential to increase the frequency split, followed by material added to the right slope.

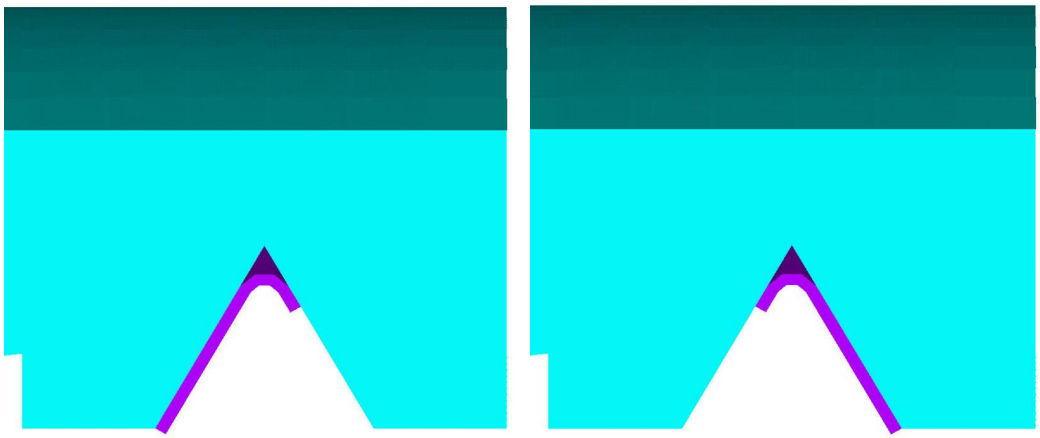

(a) A hook-shaped damper along the left slope of the groove

(b) A hook-shaped damper along the right slope of the groove

Figure 5.14: Hook-shaped dampers that respectively include damper material along the left and the right slope of the groove

	Sensitivity Analysis (Hz)	Modal Analysis (Hz)
Left Hook-Shaped Damper	0.4501	0.5114
Right Hook-Shaped Damper	0.4761	0.5311
V-Shaped Damper	0.4763	0.5364

Table 5.3: Comparison between the frequency split suggested by sensitivity analyses, and results computed from modal analyses on each of the two hook-shaped dampers and a V-shaped damper

Also, the frequency split increases linearly along both slopes with more material added. The rate of increase is 0.04785 Hz per element of material added to the left slope, and 0.05384 Hz per element added to the right slope. Interestingly, adding material to the flat surface, from location 1 to 4, causes negative frequency splits. Thus, a good damper design practice should avoid adding damping material to such regions. To validate this sensitivity analysis, two hook-shaped dampers are created, as shown in Fig. 5.14. These two dampers include damping material along left and right slope of the groove. Modal analyses are performed on the two hook-shaped dampers, as well as a V-shaped damper. Frequency splits are extracted and presented in Tab. 5.3, in comparison with the results from the sensitivity analysis.

Certain discrepancies exists between the frequency split computed from the dampers, and the sensitivity analyses. This is due to the fact that in the sensitivity analysis, the material possessed by the each of the dampers are connected with material from other

(a) Joint between damper material along the flat surface and the left slope of the groove

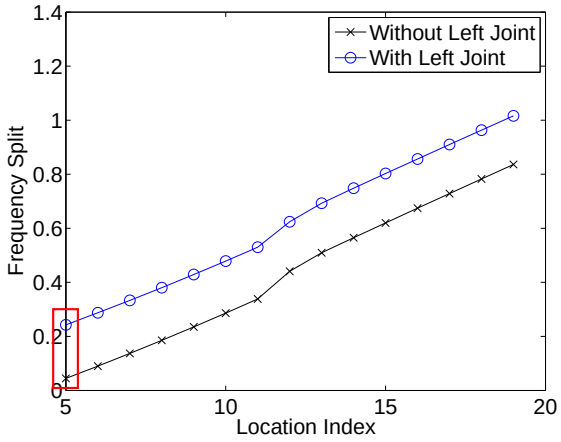

(b) Comparison between sensitivity analyses with and without the left joint

Figure 5.15: Sensitivity analyses reveal the effect of the joint on the increasing the starting point of frequency split

regions, especially the flat surfaces (location 1 to 4) that tend to decrease the frequency split. However, the trend among the frequency splits provided by each of the dampers is consistent with that observed in the sensitivity analysis.

The sensitivity analysis indicates that to create a most effective damper, material along both slopes should be included. However, it is also observed that a large increase in frequency split exists from location 4 to location 5 (Fig. 5.13). This location corresponds to the left joint between material from the flat surface and the left slope of the groove, as shown in Fig.5.15a. Thus, the above sensitivity analysis is repeated starting at location 5. Figure 5.15b reveals that without this joint, the frequency split resulted from material from other region remains the same. However, the starting point of frequency split is at a much lower value. This suggests that adding the joint to the damper design results in a larger frequency split, which is favorable in damper design practice.

Figure 5.16 shows a damper design that includes material from all the effective regions, with the joints included. A modal analysis shows that the frequency split possessed by this damper is as high as 0.8910 Hz. Nonlinear forced response analyses are also performed on this blisk-damper system. Figure 5.17 shows the maximum normalized response amplitudes at each value of ρ. Compared to a V-shaped damper (Fig. 5.8b), significant improvement in reduction ratio of response amplitudes is observed (62.89% compared to 46.95%). Moreover, the new damper has a much wider effective range of ρ values. If a threshold of 30% reduction ratio is selected, the new damper has a effective range of ρ values that is

approximately 51, 4 times wider than that provided by the V-shaped damper, which has a range that is approximately 12.

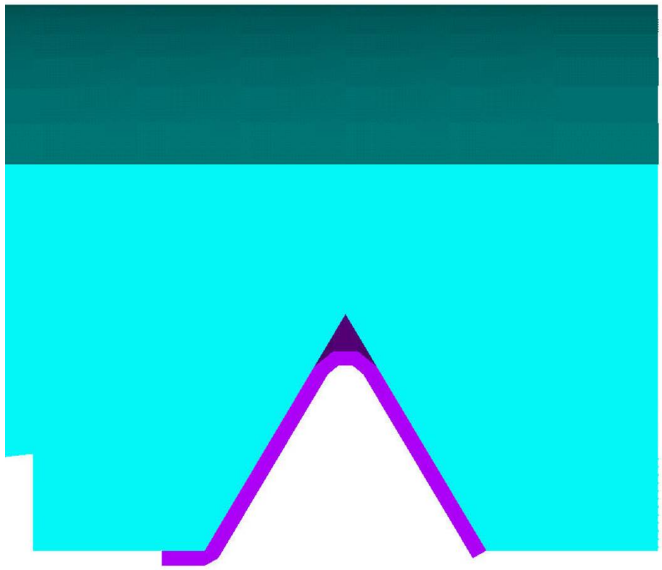

Figure 5.16: An effective damper that includes necessary joints, and material from regions that provide large frequency split

5.3.2.2 Thickness of Damping Material

In the previous section, sensitivity analyses are performed by adding damper material along the contact surface. This practice can be considered analyzing the effect of variations in one of the damper dimensions (length) on its effectiveness. In this section, sensitivity analyses are applied to explore the effect variations in another dimension of the damper geometry, which is the damper thickness. A thin-layered cone-shaped damper is applied to the left slope of the groove, as shown in Fig. 5.18a. During the sensitivity analysis, the thickness of the damper gradually increases. Modal analyses are performed after each increment of thickness to extract the frequency split (Fig 5.19). Figure 5.20 reveals the frequency split resulted from the cone-shaped damper with various thickness.

It is observed that the frequency split increases linearly with the thickness of the slope. The same analysis is repeated with a cone-shaped damper placed on the right slope of the groove (Fig. 5.18b). Linearity between the frequency split and the damper thickness is again observed, with a smaller rate of increase (Fig. 5.20). This observation suggests that increasing the damper thickness tends to increase the bending stiffness of the damper, and consequently increase the frequency split. Thus, the thickness of the V-shaped damper

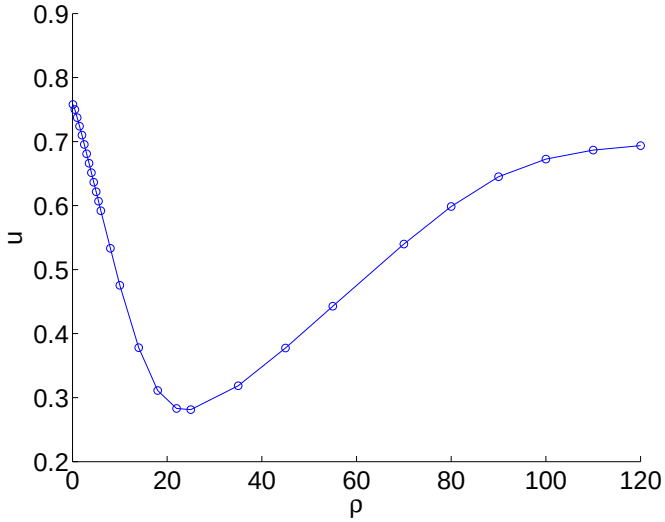

Figure 5.17: Forced responses of an effective damper with a high reduction ratio of response amplitudes, and a wide effective range of ρ values

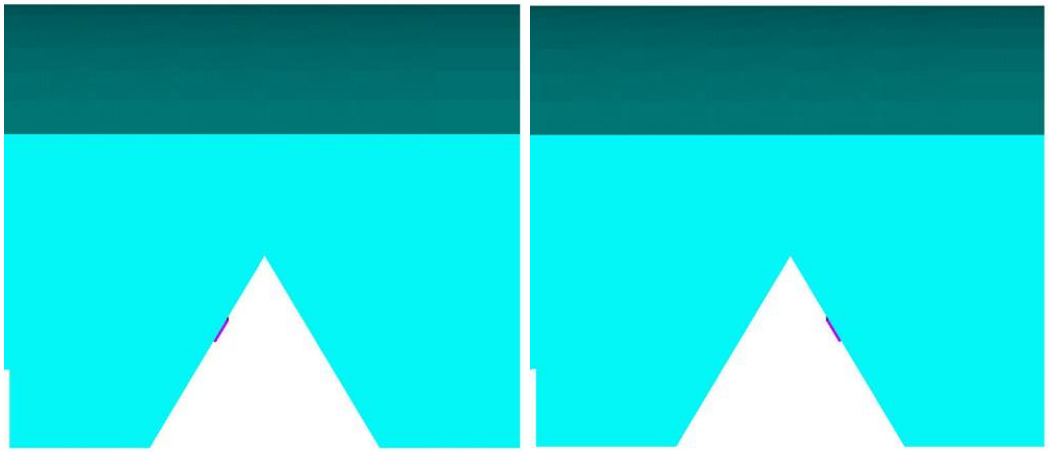

(a) Thin-layered damper on the left slope (b) Thin-layered damper on the right slope

Figure 5.18: Thin-layered cone-shaped damper placed on the left and right slope of the groove, respectively

Figure 5.19: Models involved in the sensitivity analysis with the thickness of the damper continuously increasing

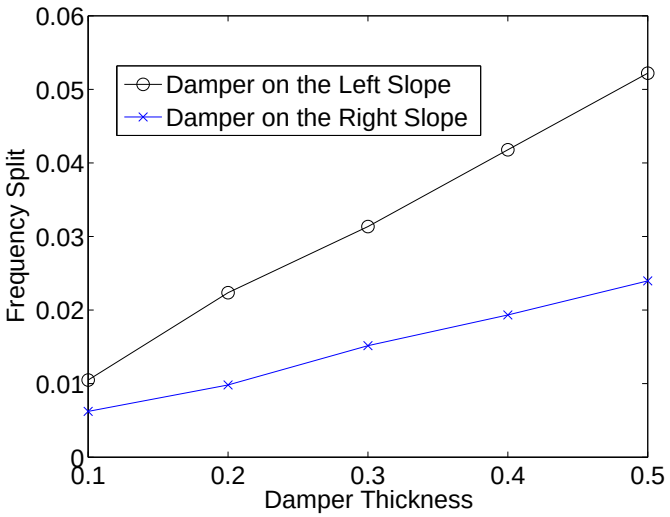

Figure 5.20: Frequency split resulted from continuously increasing damper thickness

(Fig. 5.8b) is increased by a factor of 1.7, as shown in Fig. 5.21. Nonlinear forced responses reveals that the thicker V-shaped damper has a larger reduction ratio of response amplitudes (62.93% compared to 46.95%), as shown in Fig. 5.22. And if the threshold of reduction ratio is chosen as 30%, the effective range of ρ values that the thicker V-shaped damper provides is much wider than its thinner counterpart (55.5 compared to 12).

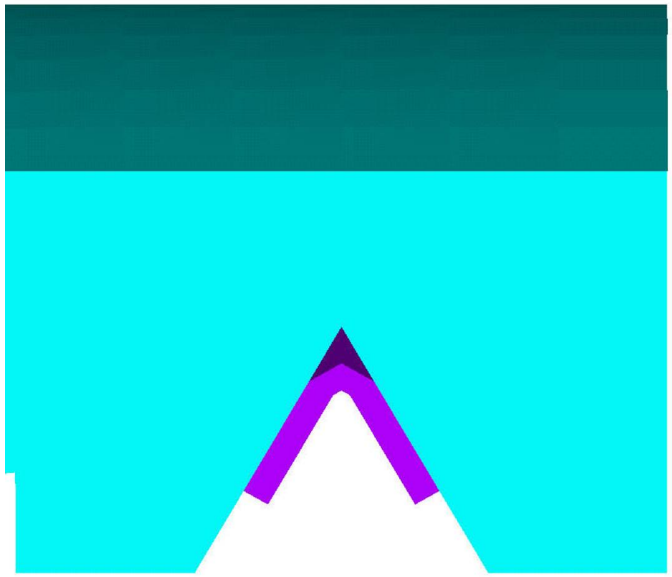

Figure 5.21: A V-shaped damper with larger thickness

The sensitivity analyses performed in previous sections reveal that the frequency split that a damper can provide depends on its location as well as thickness. During damper

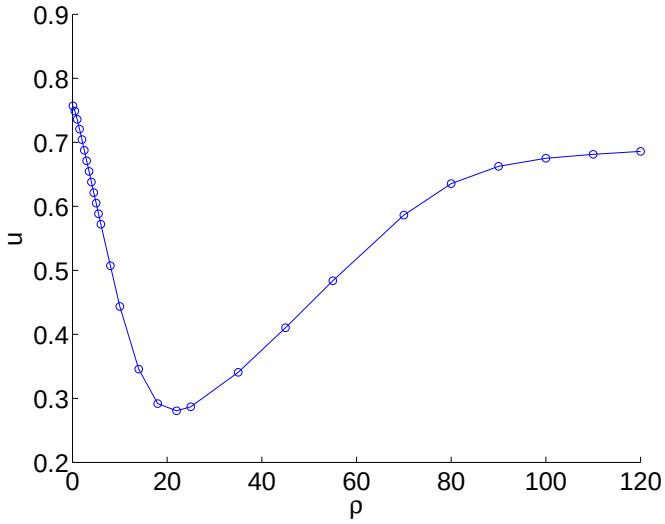

Figure 5.22: Forced responses of a V-shaped damper with increased thickness, providing a high reduction ratio of response amplitudes, and a wide effective range of ρ values

design practice, to ensure the largest possible frequency split is involved in designing an effective damper, it is recommended to first perform sensitivity analyses to reveal the locations that are most effective in proving large frequency split. Damping material placed on these locations are connected by several joints. It is favorable to involve as many joints as possible, as revealed in Sec.5.3.2.1, since joints tend to increase the bending stiffness of the damper, and consequently the frequency split. Moreover, the frequency split increases linearly with the damper thickness. Thus, after the location of the damper is determined, its thickness should be increased as much as possible to ensure an optimal frequency split.

5.4 Conclusion

The conventional damper design process involves nonlinear forced response analyses repetitively performed for numerous sets of contact and geometric parameters. The observation that the frequency split between sliding and sticking frequencies determines damper effectiveness is very impactful since computationally costly nonlinear analyses can be replaced by linear modal analyses used to extract the frequency split. A series of sensitivity analyses is used in this study to explore the geometric parameters that dictate the frequency split. Two distinctive damper models are created following the discoveries from the sensitivity analyses, and are validated to be effective by forced response analyses. These damper models provide high reduction ratio of response amplitudes and wide effective range of ρ values.

CHAPTER 6

Conclusions and Future Work

6.1 Contributions

The research in this dissertation proposes several algorithms and techniques for predicting linear and nonlinear dynamic responses of turbomachinery, and identifying design parameters of friction damping sources. The original contributions of this work are summarized as follows:

- In Chapter II, a reduced-order modeling technique based on the concept of PRIME was proposed. It was observed that the existing PRIME method can accurately capture the free and forced responses of blisks with both small and large mistuning. However, repetitive construction of small mistuning model through PRIME is computationally inefficient. To address this issue, two distinct methods, CMM and NEWT, were both strategically integrated into the PRIME work frame to specifically target small mistuning with less computational effort required, resulting in two new methods called C-PRIME and N-PRIME. Both methods were applied to the UM blisk to extract its system natural frequencies, and forced responses under traveling wave excitations. Results were validated against full-order finite element analyses, which revealed a better accuracy possessed by the N-PRIME method. Moreover, unlike the cantilever blade modes required by CMM, NEWT forms its model reduction basis with sector-level normal modes, which do not require a clear definition of the root of each blade. This property enables the N-PRIME method to be applicable to dual-flow path systems, which resemble complex structures with multiple sector-to-sector interfaces. Structural analyses were performed by applying the N-PRIME method to a typical dual-flow path system. Validation once again showed the blisk responses can be captured by N-PRIME with good accuracy. Since both PRIME and NEWT methods utilize sector-level calculations, the computational effort required by N-PRIME to generate ROMs is minimal. Thus, the N-PRIME method was used

for a Monte-Carlo analysis to study the characteristics of random combinations of both large and small mistuning. This analysis revealed emerging groups of mistuned natural frequencies resulting from isolated modes with high strain energy localization. Moreover, amplification factors of forced responses were extracted for each randomly mistuned blisk. It was discovered that the conventional method of estimating stress amplification based on displacement responses is not applicable to systems with large mistuning. The modified Weibull distribution, commonly used to estimate probability distributions of amplification factors, were proven to be invalid both physically and mathematically when large mistuning is present.

- In Chapter III, a dry friction ring damper was added to the UM blisk. To capture the nonlinear dynamics along the frictional contact surfaces between the blisk and the damper, the CoRiD method was proposed by exploring the coherent motion between the two mating contact surfaces. CoRiD utilizes the mode shapes of the blisk-damper system when the contact surfaces experience either a full sliding or a full sticking condition. The resulting mode basis mimics the relative motion between the contact surfaces, and can capture the contact dynamics accurately. Forced responses of a tuned blisk-damper system were computed by CoRiD and validated against results obtained directly from full-order systems, which revealed good accuracy provided by CoRiD. Moreover, it was noted that frictional damping sources and blade mistuning often coexist, and investigation on their mutual effects are necessary. To do that through the CoRiD method, the normal mode shapes of the mistuned blisk-damper systems required by CoRiD must be extracted in absence of cyclic symmetry. Thus, the technique of CB-CMS-CMM were developed to condense the size of full-order blisk-damper systems. CB-CMS-CMM consists of a series of model reduction steps. First, the CB-CMS model of a tuned blisk-damper system was generated. The blade mistuning component was modeled by CMM, and the mistuning model was then transformed into the CB-CMS domain. This novel model reduction process avoids repetitive construction of CB-CMS models for blisk-damper systems with multiple mistuning patterns, and significantly reduces the computational effort required to form the CoRiD mode basis. CB-CMS-CMM was validated using a UM blisk-damper system with small deviations in blade stiffness, and was proven to possess good accuracy and efficiency. Finally, since the ROMs generated by CoRiD are compact, and require minimal amount of computations, they were used for studying the correlations between frictional damping and random small mistuning, through a Monte-Carlo analysis. This analysis revealed that frictional damping has small effect on the amplification resulting from random small mistuning patterns. However, small

mistuning tends to increase the effectiveness of the damper in terms of reduction ratio in forced response amplitudes.

- In Chapter IV, the CoRiD method was strategically integrated into the PRIME work frame, resulting in the PRIME-CoRiD method, which is a comprehensive tool that can model blisk-damper systems with both large and small mistuning. It was noted that though the ROMs generated by the CB-CMS-CMM method formulated in Chapter III can be used to fast extract the system normal mode shapes required by CoRiD, this method is restricted to modeling small material mistuning. Thus, the PRIME method was adopted to replace CB-CMS-CMM as the first model reduction step, and to extend the CoRiD method to accurately predict nonlinear dynamic responses of blisk-damper systems with simultaneous large and small mistuning patterns. Contact stiffness matrices were added to the full-order blisk-damper systems, and carried throughout the PRIME partition process. The ROMs resulting from the PRIME method were compact and resembled the blisk-damper systems in either full-sliding or full-sticking contact condition. Mode shapes provided by PRIME ROMs were used as the input parameters required by the CoRiD method. The PRIME-CoRiD method was applied to a UM blisk-damper system with both large and small mistuning. The results were validated against full-order analyses and revealed good accuracy and efficiency possessed by PRIME-CoRiD. In Chapter III, weak correlations between small mistuning and frictional damping were observed. This was caused by the fact that small mistuning, compared with large mistuning, is less likely to trigger significant energy localization and amplification in forced responses. Thus, a Monte-Carlo analysis was carried out using PRIME-CoRiD to investigate the correlations between frictional damping and simultaneous large and small mistuning. It was revealed that a mixed mistuning patterns can cause the probability distributions to concentrate towards their mean values. Also, unlike small mistuning, mixed mistuning patterns can either increase or decrease the damper effectiveness. Resulting changes of reduction ratio in forced response amplitudes cannot be estimated with solely a tuned system, but through statistical analyses.

- In Chapter V, the dependence of the effectiveness of ring dampers on their geometric parameters was investigated. The geometry of a V-shaped damper was parametrized. A parametric study was performed by creating 28 different damper models by varying the damper geometric parameters simultaneously following a volume constraint. Nonlinear forced responses were computed using the CoRiD method to evaluate the damper performance. It was revealed that the 28 different dampers resulted in similar

levels of effectiveness. Further investigations have shown that these models share a nearly identical frequency split between system natural frequencies under full sliding and full sticking conditions, and validated that the frequency split influences the most the damper effectiveness. This observation is impactful since it suggests that linear modal analyses can be used to replace computationally expensive nonlinear forced responses to estimate the effectiveness of a damper. Optimal damper locations were discovered through sensitivity analyses, which also revealed that joints between damper material along different contact surfaces can enhance the bending stiffness of the damper, and consequently increase the frequency split. Moreover, it was shown that the frequency split increases approximately linearly with damper thickness. These findings assisted in proposing a set of damper design guidelines to obtain an optimal damper geometry.

6.2 Future Work

- The N-PRIME method introduced in Chapter II forms its reduction basis with sector-level cyclic modes for a pristine and each of the rogue sectors. This mode basis specifically targets cyclic symmetric structures, and is thus applicable to blisk systems. Turbomachinery components include both blisks and vane packets. Vane packets are stationary airfoils that convert rotational kinetic energy into static pressure. It is known that mistuning is also present on vane packets. However, vane packets are non-cyclic structures. Thus, the N-PRIME method cannot be directly applied to study the effect of mistuning on vane packets. Future work would utilize the PRIME partition, and form PRIME mode basis with other mode shapes obtainable from non-cyclic structures, to replace cyclic mode shapes, so that the N-PRIME method can be extended for vane packets.

- The guidelines for optimal damper design proposed in Chapter V suggests to apply damping material to more effective locations, and to increase damper thickness. The resulting damper geometry following the guidelines can be bulky and require a considerably large amount of damping material. Thus, these guidelines should be refined in the future work by performing additional sensitivity analyses with a volume constraint enforced. Moreover, the design guidelines are based on analyses on a V-shaped damper, it is necessary to conduct tests on dampers with different geometries.

BIBLIOGRAPHY

[1] Lim, S.-H., Bladh, R., Castanier, M., and Pierre, C., "A Compact, Generalized Component Mode Mistuning Representation for Modeling Bladed Disk Vibration," *Structures, Structural Dynamics, and Materials and Co-located Conferences*, American Institute of Aeronautics and Astronautics, April 2003, pp. –.

[2] Lim, S.-H., Bladh, R., Castanier, M. P., and Pierre, C., "Compact, Generalized Component Mode Mistuning Representation for Modeling Bladed Disk Vibration," *AIAA Journal*, Vol. 45, No. 9, Sept. 2007, pp. 2285–2298.

[3] Lim, S.-H., Castanier, M., and Pierre, C., "Vibration Modeling of Bladed Disks Subject to Geometric Mistuning and Design Changes," *Structures, Structural Dynamics, and Materials and Co-located Conferences*, American Institute of Aeronautics and Astronautics, April 2004.

[4] Sinha, A., "Reduced-Order Model of a Bladed Rotor With Geometric Mistuning," *J Turbomach*, Vol. 131, No. 3, April 2009, pp. 031007–031007.

[5] Bhartiya, Y. and Sinha, A., "Reduced Order Model of a Multistage Bladed Rotor With Geometric Mistuning via Modal Analyses of Finite Element Sectors," *J Turbomach*, Vol. 134, No. 4, July 2011, pp. 041001–041001.

[6] Mbaye, M., Soize, C., and Ousty, J.-P., "A Reduced-Order Model of Detuned Cyclic Dynamical Systems With Geometric Modifications Using a Basis of Cyclic Modes," *J Eng Gas Turb Power*, Vol. 132, No. 11, Aug. 2010, pp. 112502–112502.

[7] Madden, A., Epureanu, B. I., and Filippi, S., "Reduced-Order Modeling Approach for Blisks with Large Mass, Stiffness, and Geometric Mistuning," *AIAA Journal*, Vol. 50, No. 2, Feb. 2012, pp. 366–374.

[8] Ottarsson, G., Castanier, M., and Pierre, C., "A reduced-order modeling technique for mistuned bladed disks," *Structures, Structural Dynamics, and Materials and Co-located Conferences*, American Institute of Aeronautics and Astronautics, April 1994.

[9] Castanier, M. P., Ottarsson, G., and Pierre, C., "A Reduced Order Modeling Technique for Mistuned Bladed Disks," *Journal of Vibration and Acoustics*, Vol. 119, No. 3, July 1997, pp. 439–447.

[10] Bladh, R., Castanier, M. P., and Pierre, C., "Reduced Order Modeling and Vibration Analysis of Mistuned Bladed Disk Assemblies With Shrouds," *J Eng Gas Turb Power*, Vol. 121, No. 3, July 1999, pp. 515–522.

[11] Bladh, R., Pierre, C., Castanier, M. P., and Kruse, M. J., "Dynamic Response Predictions for a Mistuned Industrial Turbomachinery Rotor Using Reduced-Order Modeling," *J Eng Gas Turb Power*, Vol. 124, No. 2, March 2002, pp. 311–324.

[12] Bladh, R., Castanier, M. P., and Pierre, C., "Component-Mode-Based Reduced Order Modeling Techniques for Mistuned Bladed Disks-Part I: Theoretical Models," *J Eng Gas Turb Power*, Vol. 123, No. 1, April 2000, pp. 89–99.

[13] Bladh, R., Castanier, M. P., and Pierre, C., "Component-Mode-Based Reduced Order Modeling Techniques for Mistuned Bladed Disks-Part II: Application," *J Eng Gas Turb Power*, Vol. 123, No. 1, April 2000, pp. 100–108.

[14] Yang, M.-T. and Griffin, J. H., "A Reduced-Order Model of Mistuning Using a Subset of Nominal System Modes," *J Eng Gas Turb Power*, Vol. 123, No. 4, March 1999, pp. 893–900.

[15] Feiner, D. M. and Griffin, J. H., "A Fundamental Model of Mistuning for a Single Family of Modes," *J Turbomach*, Vol. 124, No. 4, Nov. 2002, pp. 597–605.

[16] Vargiu, P., Firrone, C., Zucca, S., and Gola, M., "A reduced order model based on sector mistuning for the dynamic analysis of mistuned bladed disks," *International Journal of Mechanical Sciences*, Vol. 53, No. 8, Aug. 2011, pp. 639–646.

[17] Fitzner, C., Epureanu, B. I., and Filippi, S., "Nodal energy weighted transformation: A mistuning projection and its application to FLADE turbines," *Mechanical Systems and Signal Processing*, Vol. 42, No. 1–2, Jan. 2014, pp. 167–180.

[18] Griffin, J., "Friction Damping of Resonant Stresses in Gas Turbine Engine Airfoils," *Journal of engineering for power*, Vol. 102, No. 2, 1980, pp. 329–333.

[19] Ferri, A., "Friction damping and isolation systems," *Journal of Mechanical Design, Transactions of the ASME*, Vol. 117 B, 1995, pp. 196–206.

[20] Menq, C.-H. and Griffin, J., "Comparison of Transient and Steady State Finite Element Analyses of the Forced Response of a Frictionally Damped Beam," *Journal of Vibration, Acoustics, Stress, and Reliability in Design*, Vol. 107, No. 1, 1985, pp. 19–25.

[21] Cameron, T., Griffin, J., Kielb, R., and Hoosac, T., "Integrated approach for friction damper design," *Journal of vibration, acoustics, stress, and reliability in design*, Vol. 112, No. 2, 1990, pp. 175–182.

[22] Csaba, G., "Modeling of a Microslip Friction Damper Subjected to Translation and Rotation," *ASME International Gas Turbine and Aeroengine Congress and Exhibition*, Vol. 4, Indianapolis, Indiana, USA, June 1999.

[23] Menq, C.-H., Bielak, J., and Griffin, J., "Influence of Microslip on Vibratory Response, Part I: A New Microslip Model," *Journal of Sound and Vibration*, Vol. 107, No. 2, 1986, pp. 279–293.

[24] Menq, C.-H., Griffin, J., and Bielak, J., "Influence of Microslip on Vibratory Response, Part II: A Comparison with Experimental Results," *Journal of Sound and Vibration*, Vol. 107, No. 2, 1986, pp. 295–307.

[25] Menq, C.-H., Cigeroglu, E., and Lu, W., "One-dimensional dynamic microslip friction model," *Journal of Sound and Vibration*, Vol. 292, No. 3-5, May 2006, pp. 881–98.

[26] Yang, B., Chu, M., and Menq, C., "Stick-slip-separation analysis and non-linear stiffness and damping characterization of friction contacts having variable normal load," *Journal of Sound and Vibration*, Vol. 210, No. 4, March 1998, pp. 461–81.

[27] Cigeroglu, E., An, N., and Menq, C.-H., "A microslip friction model with normal load variation induced by normal motion," *Nonlinear Dynamics*, Vol. 50, No. 3, 2007, pp. 609–626.

[28] Sanliturk, K. and Ewins, D., "Modelling two-dimensional friction contact and its application using harmonic balance method," *Journal of Sound and Vibration*, Vol. 193, No. 2, 1996, pp. 511–523.

[29] Menq, C. and Yang, B., "Non-linear spring resistance and friction damping of frictional constraint having two-dimensional motion," *Journal of Sound and Vibration*, Vol. 217, No. 1, 1998, pp. 127–143.

[30] Yang, B. and Menq, C., "Characterization of 3D contact kinematics and prediction of resonant response of structures having 3D frictional constraint," *Journal of Sound and Vibration*, Vol. 217, No. 5, 1998, pp. 909–925.

[31] Chen, J., Yang, B., and Menq, C., "Periodic forced response of structures having three-dimensional frictional constraints," *Journal of Sound and Vibration*, Vol. 229, No. 4, 2000, pp. 775–792.

[32] Pfeiffer, F. and Hajek, M., "Stick-Slip Motion of Turbine Blade Dampers," *Philosophical Transactions of the Royal Society of London A: Mathematical, Physical and Engineering Sciences*, Vol. 338, No. 1651, March 1992, pp. 503–517.

[33] Sextro, W., Popp, K., and Wolter, I., "Improved reliability of bladed disks due to friction dampers," *American Society of Mechanical Engineers (Paper)*, ASME, Orlando, FL, USA, 1997.

[34] Tanrikulu, O., Kuran, B., Ozguven, H., and Imregun, M., "Forced harmonic response analysis of nonlinear structures using describing functions," *AIAA journal*, Vol. 31, No. 7, 1993, pp. 1313–1320.

[35] Cigeroglu, E. and Ozguven, H. N., "Nonlinear vibration analysis of bladed disks with dry friction dampers," *Journal of Sound and Vibration*, Vol. 295, No. 3-5, 2006, pp. 1028–1043.

[36] Cardona, A., Coune, T., Lerusse, A., and Geradin, M., "A multiharmonic method for non-linear vibration analysis," *International Journal for Numerical Methods in Engineering*, Vol. 37, No. 9, May 1994, pp. 1593–608.

[37] Yang, B. and Menq, C., "Characterization of contact kinematics and application to the design of wedge dampers in turbomachinery blading: Part 1 - stick-slip contact kinematics," *J Eng Gas Turb Power*, Vol. 120, No. 2, 1998, pp. 410–417.

[38] Yang, B. and Menq, C., "Characterization of contact kinematics and application to the design of wedge dampers in turbomachinery blading: Part 2 - prediction of forced response and experimental verification," *J Eng Gas Turb Power*, Vol. 120, No. 2, 1998, pp. 418–423.

[39] Sanliturk, K., Ewins, D., and Stanbridge, A., "Underplatform dampers for turbine blades: Theoretical modeling, analysis, and comparison with experimental data," *J Eng Gas Turb Power*, Vol. 123, No. 4, 2001, pp. 919–929.

[40] Yang, B., Chen, J., and Menq, C., "Prediction of resonant response of shrouded blades with three-dimensional shroud constraint," *J Eng Gas Turb Power*, Vol. 121, No. 3, 1999, pp. 523–529.

[41] Petrov, E. and Ewins, D., "Analytical formulation of friction interface elements for analysis of nonlinear multi-harmonic vibrations of bladed disks," *Journal of Turbomachinery*, Vol. 125, No. 2, 2003, pp. 364–371.

[42] Chen, J. and Menq, C., "Periodic response of blades having three-dimensional nonlinear shroud constraints," *J Eng Gas Turb Power*, Vol. 123, No. 4, 2001, pp. 901–909.

[43] Lau, S., Cheung, Y., and Wu, S., "Incremental Harmonic Balance Method With Multiple Time Scales for Aperiodic Vibration of Nonlinear Systems," *Journal of Applied Mechanics, Transactions ASME*, Vol. 50, No. 4 a, 1983, pp. 871–876.

[44] Pierre, C., Ferri, A., and Dowell, E., "Multi-harmonic analysis of dry friction damped systems using an incremental harmonic balance method," *Transactions of the ASME. Journal of Applied Mechanics*, Vol. 52, No. 4, Dec. 1985, pp. 958–64.

[45] Guillen, J., *Studies of the dynamics of dry-friction-damped blade assemblies*, Ph.D. thesis, University of Michigan, Ann Arbor, 1999.

[46] Poudou, O. and Pierre, C., "Hybrid frequency-time domain methods for the analysis of complex structural systems with dry friction damping," *Collection of Technical Papers - AIAA/ASME/ASCE/AHS/ASC Structures, Structural Dynamics and Materials Conference*, Vol. 1, American Inst. Aeronautics and Astronautics Inc., Norfolk, VA, United states, 2003, pp. 111–124.

[47] Petrov, E., "A method for use of cyclic symmetry properties in analysis of nonlinear multiharmonic vibrations of bladed disks," *Journal of Turbomachinery*, Vol. 126, No. 1, 2004, pp. 175–183.

[48] Siewert, C., Panning, L., Wallaschek, J., and Richter, C., "Multiharmonic forced response analysis of a turbine blading coupled by nonlinear contact forces," *J Eng Gas Turb Power*, Vol. 132, No. 8, 2010.

[49] Craig, R. R. and Kurdila, A. J., *Fundamentals of structural dynamics*, John Wiley & Sons, 2nd ed., 2006.

[50] Berthillier, M., Dupont, C., Mondal, R., and Barrau, J., "Blades forced response analysis with friction dampers," *Journal of Vibration and Acoustics, Transactions of the ASME*, Vol. 120, No. 2, 1998, pp. 468–474.

[51] Cigeroglu, E., An, N., and Menq, C.-H., "Wedge damper modeling and forced response prediction of frictionally constrained blades," *Proceedings of the ASME Turbo Expo*, Vol. 5, American Society of Mechanical Engineers, Montreal, Que., Canada, 2007, pp. 519–528.

[52] Cigeroglu, E., An, N., and Menq, C.-H., "Forced response prediction of constrained and unconstrained structures coupled through frictional contacts," *J Eng Gas Turb Power*, Vol. 131, No. 2, March 2009, pp. 022505 (11 pp.).

[53] Mitra, M., Zucca, S., and Epureanu, B. I., "Adaptive Microslip Projection for Reduction of Frictional and Contact Nonlinearities in Shrouded Blisks," *Journal of Computational and Nonlinear Dynamics*, Vol. 11, No. 4, May 2016, pp. 041016–041016.

[54] Popp, K., Panning, L., and Sextro, W., "Vibration damping by friction forces: Theory and applications," *JVC/Journal of Vibration and Control*, Vol. 9, No. 3-4, 2003, pp. 419–448.

[55] Firrone, C. M. and Zucca, S., *Numerical Analysis - Theory and Application*, chap. 14 Modelling Friction Contacts in Structural Dynamics and its Application to Turbine Bladed Disks, InTech, 2011, ISBN: 978-953-307-389-7.

[56] Niemotka, M. A. and Ziegert, J. C., "Optimal design of split ring dampers for gas turbine engines," *ASME 1993 International Gas Turbine and Aeroengine Congress and Exposition, GT 1993*, Vol. 2, American Society of Mechanical Engineers, Cincinnati, OH, United states, 1993, pp. International Gas Turbine Institute–.

[57] Laxalde, D., Thouverez, F., Sinou, J.-J., and Lombard, J.-P., "Qualitative analysis of forced response of blisks with friction ring dampers," *European Journal of Mechanics, A/Solids*, Vol. 26, No. 4, 2007, pp. 676–687.

[58] Laxalde, D., Thouverez, F., and Lombard, J.-P., "Forced response analysis of integrally bladed disks with friction ring dampers," *Journal of Vibration and Acoustics, Transactions of the ASME*, Vol. 132, No. 1, 2010, pp. 0110131–0110139.

[59] Laxalde, D., Salles, L., Blanc, L., and Thouverez, F., "Non-linear modal analysis for bladed disks with friction contact interfaces," *Proceedings of the ASME Turbo Expo*, Vol. 5, American Society of Mechanical Engineers, Berlin, Germany, 2008, pp. 457–467.

[60] Petrov, E. P., "Method for Direct Parametric Analysis of Nonlinear Forced Response of Bladed Disks With Friction Contact Interfaces," *Journal of Turbomachinery*, Vol. 126, No. 4, Dec. 2004, pp. 654–662.

[61] Petrov, E. P., "Sensitivity Analysis of Nonlinear Forced Response for Bladed Discs with Friction Contact Interfaces," *Proceedings of ASME Turbo Expo*, No. GT2005-68935, Reno-Tahoe, NV, June 6-9 2005.

[62] Petrov, E. P., "Direct Parametric Analysis of Resonance Regimes for Nonlinear Vibrations of Bladed Disks," *Journal of Turbomachinery*, Vol. 129, No. 3, July 2006, pp. 495–502.

[63] Petrov, E. P., "Method for Sensitivity Analysis of Resonance Forced Response of Bladed Disks With Nonlinear Contact Interfaces," *Journal of Engineering for Gas Turbines and Power*, Vol. 131, No. 2, Dec. 2008, pp. 022510–022510.

[64] Krack, M., Panning, L., Wallaschek, J., Siewert, C., and Hartung, A., "Robust Design of Friction Interfaces of Bladed Disks With Respect to Parameter Uncertainties," *Proceedings of ASME Turbo Expo*, Vol. 7, Copenhagen, Denmark, June 11-15 2012, pp. 1193–1204.

[65] Petrov, E., "Explicit finite element models of friction dampers in forced response analysis of bladed disks," *Journal of Engineering for Gas Turbines and Power*, Vol. 130, No. 2, March 2008, pp. 022502 (11 pp.)–.

[66] Beck, J. A., Brown, J. M., Cross, C. J., and Slater, J. C., "Component-Mode Reduced-Order Models for Geometric Mistuning of Integrally Bladed Rotors," *AIAA Journal*, Vol. 52, No. 7, May 2014, pp. 1345–1356.

[67] Sundararajan, P. and Noah, S., "Dynamics of forced nonlinear systems using shooting/arc-length continuation method - application to rotor systems," *Journal of Vibration and Acoustics, Transactions of the ASME*, Vol. 119, No. 1, 1997, pp. 9–20.

[68] Tang, W., Baek, S., and Epureanu, B. I., "Reduced Order Models for Blisks with Small and Large Mistuning and Friction Dampers," *Journal of Engineering for Gas Turbines and Power*, July 2016, pp. –.

[69] Tang, W., Baek, S., and Epureanu, B. I., "Reduced Order Models for Blisks With Small and Large Mistuning and Friction Dampers," *Proceedings of ASME Turbo Expo*, Vol. 7A, Seoul, South Korea, June 13C17 2016.